

# Low-Dimensional Metal Halide Perovskite Photodetectors

Hsin-Ping Wang, Siyuan Li, Xinya Liu, Zhifeng Shi, Xiaosheng Fang,\* and Jr-Hau He\*

Metal halide perovskites (MHPs) have been a hot research topic due to their facile synthesis, excellent optical and optoelectronic properties, and record-breaking efficiency of corresponding optoelectronic devices. Nowadays, the development of miniaturized high-performance photodetectors (PDs) has been fueling the demand for novel photoactive materials, among which low-dimensional MHPs have attracted burgeoning research interest. In this report, the synthesis, properties, photodetection performance, and stability of low-dimensional MHPs, including 0D, 1D, 2D layered and nonlayered nanostructures, as well as their heterostructures are reviewed. Recent advances in the synthesis approaches of low-dimensional MHPs are summarized and the key concepts for understanding the optical and optoelectronic properties related to the PD applications of low-dimensional MHPs are introduced. More importantly, recent progress in novel PDs based on low-dimensional MHPs is presented, and strategies for improving the performance and stability of perovskite PDs are highlighted. By discussing recent advances, strategies, and existing challenges, this progress report provides perspectives on low-dimensional MHP-based PDs in the future.

charge carrier collection. Nowadays, PDs detecting in the UV–visible to near-infrared (NIR) spectrum range are mainly based on crystalline inorganic elemental semiconductors, such as Si, III–V and II–VI semiconductors, and their heterojunctions.<sup>[5,6]</sup> These PDs have been fully investigated and mature, but they usually have complicated structures and require high-temperature and complex fabrication processes, such as metal-organic chemical vapor deposition (MOCVD) and molecular-beam epitaxy (MBE), leading to high cost. Moreover, the mechanical inflexibility of materials limits their broader applications for large-area and flexible PDs.

PDs made by solution-processed semiconductors have recently emerged as a potential candidate for next-generation light sensors.<sup>[3,7–9]</sup> Among them, metal halide perovskites (MHPs) have been sparking wide interest for optoelectronic devices because they hold several advantages over traditional materials such as the simplicity of their processing (e.g., solution deposition), high absorption coefficient, weakly bound excitons, long carrier lifetime >1 ms in polycrystalline films, and tunable bandgap between 1.48 and 2.23 eV.<sup>[10–14]</sup> Ballif's group found a high absorption coefficient of MAPbI<sub>3</sub> (MA = methylammonium) perovskite with particularly sharp onset and discussed the relation between sharp optical absorption edge and its photovoltaic performance.<sup>[15]</sup> MHPs exhibit a much higher absorption coefficient than crystalline Si and show an exponential trend over more than four decades with an Urbach energy of 15 meV for MAPbI<sub>3</sub> and as low as 13 meV for MAPbBr<sub>3</sub>, which is comparable to III–V materials (e.g., Urbach energy of GaAs is 7 meV).<sup>[12,15]</sup> The low value of Urbach energy indicates a very low degree of structural disorder and high crystallinity of MHP crystals. The purely exponential optical absorption edge strongly suggests no apparent presence of deep states within the bandgap, which is likely a key factor why MHPs can feature such great optoelectronic performance compared to other materials.<sup>[12,16]</sup> In brief, MHPs have attracted considerable attention because of such superb optoelectronic properties comparable to III–V materials but much cost-effective fabrication processes. These advantages make researchers believe perovskites could also be a good candidate for future PDs. Encouragingly, polycrystalline MHP PDs exhibit comparable or even better performance than those traditional single-crystalline semiconductors (Si, Ge, etc.) and high-temperature epitaxial semiconductor PDs (InGaAs, HgCdTe, etc.) due to their great optoelectronic


## 1. Introduction

Photodetectors (PDs), which convert optical signals to electrical signals, have wide applications in many fields, such as optical communication, image sensing, environmental monitoring, and sensing in the Internet of Things (IoT).<sup>[1–4]</sup> An efficient PD requires high responsivity ( $R$ ), high detectivity ( $D^*$ ), on/off ratio, and fast response speed. To realize these characteristics, the active layers in PDs must have a high absorption coefficient, low trap-state density ( $n_{\text{trap}}$ ), high carrier mobility, and efficient

Dr. H.-P. Wang, Prof. J.-H. He  
Department of Materials Science and Engineering  
City University of Hong Kong  
Tat Chee Avenue, Kowloon, Hong Kong  
E-mail: jrhaue@cityu.edu.hk

S. Y. Li, X. Y. Liu, Prof. X. S. Fang  
Department of Materials Science  
Fudan University  
Shanghai 200433, P. R. China  
E-mail: xshfang@fudan.edu.cn

Prof. Z. F. Shi  
Key Laboratory of Materials Physics of Ministry of Education  
School of Physics and Microelectronics  
Zhengzhou University  
Daxue Road 75, Zhengzhou 450052, P. R. China

 The ORCID identification number(s) for the author(s) of this article can be found under <https://doi.org/10.1002/adma.202003309>.

DOI: 10.1002/adma.202003309

properties.<sup>[17]</sup> Polycrystalline MHPs film based PDs can demonstrate high  $D^*$  of  $\approx 1 \times 10^{15}$  Jones ( $\text{cm Hz}^{1/2} \text{W}^{-1}$ ) together with the fast response time of a few microseconds,<sup>[18]</sup> which is close to the commercial GaAs. Moreover, perovskite PDs provide other good characteristics such as transparency, mechanical flexibility, and compatibility to roll-to-roll process, making them desirable for a new class of revolutionary optoelectronic devices.

Despite the remarkable device performance, MHPs with polycrystalline 3D structures still suffer from low carrier mobility ( $< 10 \text{ cm}^2 \text{ V}^{-1} \text{ s}^{-1}$ ) and undesired charge recombination at the grain boundaries.<sup>[19]</sup> In polycrystalline materials, grain boundaries act as a high defect density region and tend to decrease the electrical properties of the materials. Electrically active ions or other impurities might segregate along grain boundaries, causing nonuniform electrical properties over the films.<sup>[20]</sup> Moreover, it is revealed that the grain boundaries in polycrystalline MHPs are especially unstable and highly vulnerable to moisture.<sup>[21]</sup> These effects hinder their practical applications in stable functional devices. Compared with polycrystalline MHP thin films, it is found that the  $n_{\text{trap}}$  of MHP single crystals is only  $10^9$ – $10^{10} \text{ cm}^{-3}$ , which is much lower than that of solution-processed polycrystalline MAPbI<sub>3</sub> films ( $10^{16}$ – $10^{17} \text{ cm}^{-3}$ ).<sup>[22,23]</sup> Unfortunately, these macroscopic single crystals are too thick to realize efficient PDs. It is difficult to directly grow scalable single crystals on a planar substrate due to the rapid reaction of perovskite precursors, curtailing their potential for optoelectronic applications.

Low-dimensional single-crystalline perovskites can be easily fabricated on planar or flexible substrates. They possess not only the advantages of single-crystalline perovskites such as fewer grain boundaries, lower  $n_{\text{traps}}$ , lower recombination rate, and longer lifetime of the photogenerated carriers, but also good mechanical properties for flexible and printable devices, which have attracted great attention.<sup>[14,24–30]</sup> Much promising progress has been made for PD applications in recent years. For example, ultrasensitive PDs with a high  $R$  of more than  $1.5 \times 10^4 \text{ A W}^{-1}$ ,  $D^*$  of  $7.45 \times 10^{15}$  Jones, and fast switching ratio of few microseconds are demonstrated based on single-crystalline layered MHP nanowires (NWs), which show superior performance than PDs based on polycrystalline MHP films and even many commercial PDs.<sup>[31]</sup> The change of dimensionality of MHPs also influences the stability of final devices. Low-dimensional perovskites have shown signs of better stability than polycrystalline ones in terms of phase stability, environmental stability, mechanical stability, and suppressed ion migration. In Deng's study, the PDs fabricated from MAPbI<sub>3</sub> microwire arrays exhibit long-term stability of >50 days in air; by contrast, the PDs made with polycrystalline MAPbI<sub>3</sub> film gradually degrade with time and nearly fully degrade after 40 days.<sup>[32]</sup> Moreover, many groups presented the outstanding flexibility (>10 000 cycles) of PDs with only a small performance change, showing great mechanical stability of PDs with low-dimensional MHPs.<sup>[33–35]</sup>

In addition to the promising performance and improved stabilities, as well as the flexibility, it has been found that PDs based on low-dimensional MHPs have potentials for different types of PDs, which have not been observed in polycrystalline MHPs. 1D MHPs can serve as polarization-sensitive PDs

because of their anisotropic optical properties, and that could be useful in applications including integrated photonic circuits, optical switches, near-field imaging, and high-resolution detection.<sup>[36]</sup> 2D layered MHPs have their potentials for wavelength-selective narrowband PDs, which are attractive in the field of biomedical sensing, defense, imaging, and machine vision.<sup>[37]</sup> 2D layered and quasi-2D MHPs with chiral organic ammonium in the lattice have been demonstrated their circularly polarized light (CPL) detection ability, which has wide potential applications such as magnetic memory devices, telecommunication, optical information processing, display technologies, and chiral catalysis.<sup>[38,39]</sup> These discoveries have attracted many researchers' interests in low-dimensional MHPs for PD applications.

In this review, we summarize recent advances in PDs based on low-dimensional MHPs, focusing on the synthesis and properties, the photodetection performance, and stability of low-dimensional MHPs, including 0D, 1D, 2D perovskites, and their heterostructures. We first briefly introduce the fundamentals of PDs and the important parameters to characterize them. Then, in Section 3, we highlight the unique characteristics of low-dimensional MHPs including their chemical, optical, and optoelectronic properties. The bandgap engineering strategies of low-dimensional MHPs are summarized in Section 4. In Section 5, recent advances made in PDs based on low-dimensional perovskites are surveyed and summarized. We also summarize the key figures of merit of the most typical low-dimensional perovskite-based PDs for comparison. Then, the stability of low-dimensional perovskites and the corresponding PD devices are discussed in a focused section (Section 6). In Section 7, we summarize the self-powered MHP PDs and other practical applications of MHP PDs in optical communication and biomimetic eyes. Low-dimensional MHP PDs still have substantial development ahead in order to be competitive with traditional Si PDs, such as stability. Finally, we give an outlook based on the current status of low-dimensional perovskite-based PDs and provide some strategies to improve their performance and long-term stability.

## 2. Fundamentals of PDs

As a fundamental device in both academia and industry, various types of PDs have been developed and applied to a variety of circumstances, such as imaging, spectroscopy, and communications.<sup>[40–43]</sup> To achieve high-performance PDs, a 5S standard (high sensitivity, high signal-to-noise ratio, high spectral selectivity, fast response speed, and satisfactory stability) has been proposed for practical applications.<sup>[44]</sup> More specifically, the major figures of merit to characterize the performance of a PD are listed as follows.

### 2.1. Photoresponsivity ( $R_\lambda$ )

When exposed to incident light, the difference of photocurrent ( $I_p$ ) and dark current ( $I_d$ ) in a PD can be measured. The photoresponsivity of a PD refers to the  $\Delta I$  divided by the incident power ( $P_\lambda$ ). The  $R_\lambda$  of a PD can vary with the incident

wavelength because of the bandgap and the surface recombination of the active layer.<sup>[45]</sup> The  $R_\lambda$  can be calculated as follows

$$R_\lambda \text{ (A W}^{-1}\text{)} = \frac{(I_p - I_d)}{P_\lambda} \quad (1)$$

## 2.2. On/Off Ratio

The on/off ratio is the ratio of photocurrent ( $I_p$ ) and dark current ( $I_d$ ) of a PD, which mainly depends on the photoelectric conversion and charge transport of the active layer. To increase the on/off ratio, effort should be made to increase the photocurrent and/or to reduce the dark current.

## 2.3. External Quantum Efficiency (EQE)

The external quantum efficiency refers to the ratio of the number of collected charge carriers and the number of incident photons. This figure of merit shows the average number of photogenerated carriers per incident photon. The EQE can be derived from the photoresponsivity ( $R_\lambda$ ) and incident wavelength ( $\lambda$ )

$$\text{EQE (\%)} = \frac{R_\lambda hc}{e\lambda} \quad (2)$$

## 2.4. Photoconductive Gain (G)

The photoconductive gain is defined as the ratio of the number of collected carriers in a PD and the number of absorbed photons. Note that the incident light power cannot be totally absorbed by the active layer of a PD, the quantum efficiency ( $\eta$ ) is introduced to determine the ratio of absorbed light power and incident power.<sup>[46]</sup> The gain can also be calculated by the ratio of carrier lifetime ( $\tau_{\text{lifetime}}$ ) and transit time between electrodes ( $\tau_{\text{transit}}$ ), where  $\tau_{\text{transit}} = d^2/\mu V$ ,  $d$  is the distance of the two electrodes,  $\mu$  is the mobility of the majority charge carrier, and  $V$  is the applied voltage. In the case that the lifetime is longer than the transit time, a gain is therefore generated<sup>[47]</sup>

$$G = \frac{(I_p - I_d) h\nu}{eP_\lambda \eta} = \frac{\tau_{\text{lifetime}}}{\tau_{\text{transit}}} = \frac{\tau_{\text{lifetime}} \cdot \mu V}{d^2} \quad (3)$$

## 2.5. Specific Detectivity ( $D^*$ )

The parameter of detectivity ( $D$ ) is the signal detecting sensitivity of a PD from noise environment, which is defined as the inverse of the noise equivalent power (NEP). When the NEP is normalized by the square root of the product of the detector area ( $S$ ) and the bandwidth ( $\Delta f$ ), its reciprocal is defined as the  $D^*$ . The unit of the  $D^*$  is in Jones ( $\text{cm Hz}^{1/2} \text{W}^{-1}$ ). In the circumstances where the shot noise is the dominant contributor, the  $D^*$  can be calculated as follows<sup>[48]</sup>

$$D^* \text{ (Jones)} = \frac{(S\Delta f)^{1/2}}{\text{NEP}} = \frac{R_\lambda}{(2eI_d/S)^{1/2}} \quad (4)$$

## 2.6. Linear Dynamic Range (LDR)

The LDR means the range of incident light power for which a PD responds linearly to the external illumination. The LDR is given by the following equation

$$\text{LDR (dB)} = 20 \log \left( \frac{I_p^*}{I_d^*} \right) \quad (5)$$

in which  $I_p^*$  and  $I_d^*$  are the upper and lower limit of the linear range, respectively. In some reports,  $I_p^*$  represents the photocurrent obtained under  $1.0 \text{ mW cm}^{-2}$  light excitation and  $I_d^*$  is the dark current.

## 2.7. Spectral Selectivity

Actual PDs generally work at specific wavelength ranges to meet users' diverse demands. The spectral selectivity of a PD can be measured by the full width half maximum (FWHM) of its spectral photoresponsivity. The smaller FWHM indicates the narrower response peak width and the better spectral selectivity. PDs with selective wavelength ranges are generally achieved by the selection of active materials with suitable bandgaps and the design of device structure.

## 2.8. Response Time

The response time of a PD is an indicator of its response speed to externally incident light. It is generally identified by the rise time ( $\tau_{\text{rise}}$ ) and the decay time ( $\tau_{\text{decay}}$ ), which are defined as the time for the current to rise to 90% of its maximum after exposure to incident light and the time for the current to decay to 10% of its maximum after the removal of the incident light, respectively.<sup>[49]</sup>

Based on their working mechanisms, currently used PDs could be roughly divided into three categories, namely, photoconductors, photodiodes, and phototransistors. Generally, photoconductors consist of photoactive materials and two Ohmic contacts, and externally applied bias voltage is required to separate photogenerated electron-hole pairs. Under bias voltage, charge carriers are injected into the semiconductor layer from metal contacts. An advantageous feature of photoconductors is that photogenerated charge carriers are able to circulate in the circuit several times before recombination, possibly leading to a high value of EQE or gain (>100%). But the long carrier lifetime of photoconductors also brings drawbacks such as slow response speed. By contrast, photodiodes with structures such as p-n, p-i-n, or Schottky junctions mainly rely on a built-in electric field to separate photogenerated carrier pairs without carrier injection under reverse bias.<sup>[1]</sup> Compared with photoconductors, photodiodes boast the advantages of fast response speed and very low dark current under reverse bias, and they can function in the photovoltaic mode without external energy supply. However, the mentioned advantages benefit the photo-detection performance at the cost of reducing the EQE (<100%). As for phototransistors, the carrier concentration in the channel

can be modulated by applying the gate voltage. Phototransistors can yield relatively low dark current when working in the depletion regime, and exhibit high gain similar to photoconductors when exposed to light illumination.<sup>[3]</sup> Therefore phototransistors can overcome the trade-off between low dark current and high gain to some extent. In recent years, much effort has been made to improve the performance of PDs with different mechanisms and structures, moving toward the 5S requirements.

### 3. The Synthesis and Properties of Low-Dimensional MHPs

Inherited from the perovskite structure and originated from their reduced dimensionalities, low-dimensional MHPs show unique physical and chemical properties compared to their bulk counterparts. From 0D quantum dots (QDs), nanocrystals (NCs) and nanoparticles (NPs), 1D NWs and nanorods, to 2D nanosheets (NSs) and nanoplates, great progress has been made on the study of low-dimensional halide perovskites in recent years. In this section, we focus on the recent advances in synthesis strategies as well as the unique optical and optoelectronic properties related to the optoelectronic applications of low-dimensional MHPs.

#### 3.1. Synthesis

##### 3.1.1. Solution Synthesis

Solution-based syntheses have the advantage of mass production of colloidal nanostructures with relatively low cost, and therefore have been widely used in the preparation of various nanostructures.<sup>[27]</sup> For the preparation of 0D MHPs, two synthetic methods have been widely used, i.e., the ligand-assisted reprecipitation (LARP) and hot injection.<sup>[50–54]</sup> An early attempt to synthesize colloidal perovskite NPs through template-free LARP approach was reported by Pérez-Prieto and co-workers.<sup>[50]</sup> This strategy involves using ammonium bromide as capping ligands for the self-termination of the crystallization of MAPbBr<sub>3</sub> NPs (≈6 nm, MA = CH<sub>3</sub>NH<sub>3</sub>), and using poor solvent for nucleation. The synthesized NPs can be kept dispersed in organic solvents for more than three months. Zhang et al. further developed the LARP method to precipitate MAPbX<sub>3</sub> (X = Cl, Br, and I) QDs by simply dropping perovskite precursors containing long-chain ligands into a poor solvent (toluene) under stirring.<sup>[51]</sup> They found the low-cost LARP method provides not only the increased photoluminescence quantum yield (PLQY), but also good colloidal stability through surface passivation of ligands. Besides preparing colloidal 0D NPs, the LARP method is modified to fabricate MHP NP films on substrates. Han et al. reported the in situ fabrication of uniform FAPbBr<sub>3</sub> (FA = formamidinium) NP films by dropping antisolvent during the spin-coating of the MHP precursor solution.<sup>[55]</sup> They used 3,3-diphenylpropylamine bromide as the capping ligand, and the adding of antisolvent before nucleation facilitates fast precipitation of MHP NCs, forming MHP films for efficient light-emitting devices (LEDs). Another practical synthetic approach for 0D MHPs is hot injection. Protesescu et al.

first reported the preparation of all-inorganic CsPbX<sub>3</sub> NCs by quickly injecting Cs-oleate solution into PbX<sub>2</sub> solution at an elevated temperature between 140 to 200 °C.<sup>[52]</sup> With the help of oleylamine (OLA) and oleic acid (OA), size-controlled perovskite NCs could be obtained by adjusting the reaction temperature (Figure 1a–c), further contributing to its tunable optical properties. Apart from these two synthesis methods, some other strategies have been developed to synthesize 0D MHPs, including emulsion synthesis,<sup>[56]</sup> ultrasonication synthesis,<sup>[57]</sup> solvothermal,<sup>[58]</sup> and template-assisted methods.<sup>[59]</sup> Since the LARP and hot injection usually employ long-chain surfactants to stabilize or confine the growth of MHP NCs, they bring about the issue of reduced charge transport. To solve this problem, Huang et al. proposed an emulsion method for the synthesis of MHP QDs.<sup>[56]</sup> As shown in Figure 1d, two immiscible solvents are employed to form an emulsion system, in which the two liquids are separated in microscopic scale. Subsequently, the demulsion step initialize solvent mixing and induce the crystal growth, producing QD colloidal solution (Figure 1e). Some other novel strategies were also explored for 0D MHPs, and, for example, Wei et al. reported the epitaxial synthesis of CsPbX<sub>3</sub>/Cs<sub>2</sub>GeF<sub>6</sub> hybrid NCs by partial surface chemical conversion of Cs<sub>2</sub>GeF<sub>6</sub> double perovskite with PbX<sub>2</sub>.<sup>[60]</sup> In addition, some researchers focus on top-down approaches for the synthesis of 0D nanostructures. For example, Huang et al. synthesized MAPbBr<sub>3</sub> NCs by mixing precursors, MABr and PbBr<sub>2</sub>, with two ligands—OA and OLA.<sup>[61]</sup> The ligands directly break the bulk perovskite into small MAPbBr<sub>3</sub> NCs with an average size of 4 nm under ultrasonication. The method avoids the use of less volatile polar solvents and multiple post-treatment processes, yielding MHP NCs with higher PLQY and improved stability.

The key point of solution-based preparation of 1D MHPs, such as NWs and nanorods, is the anisotropic growth of nanostructures. To achieve this, bottom-up approaches are commonly used, including the oriented assembly of nanocrystal building blocks, or using surfactants and templates to direct the anisotropic growth. Recently, the nanoscale “additive fabrication” of defect-free 1D NWs was accomplished via the visible-light-induced self-assembly of cubic CsPbBr<sub>3</sub> NCs.<sup>[62]</sup> The self-assembly process involves the selective desorption of surface ligands, i.e., OA and OLA, under light illumination. During the 0D–1D transformation, the anisotropic linear growth and a cubic-to-orthorhombic phase transformation were observed by researchers, and the NWs show a much longer photoluminescence (PL) lifetime than that of NC building blocks. Besides, 1D MHP nanostructures can also be obtained by surfactant-directed 1D growth mechanisms, where growth kinetics and product morphology could be controlled by adjusting reaction conditions. Yang and co-workers prepared CsPbX<sub>3</sub> NWs by reacting Cs-oleate with lead halide in octadecene (ODE) with the participation of OA and OLA.<sup>[63]</sup> When changing the solvent from ODE to OLA, the reaction possesses slower kinetics but a higher yield of NWs, suggesting the role of surfactants in this method. Recently, Du et al. adapted the surfactant-assisted method for the solvothermal synthesis of CsPbI<sub>3</sub> nanotubes with a cavity.<sup>[64]</sup> They prepared the nanotubes by mixing Cs-oleate solution with PbI<sub>2</sub> precursor in ODE and reacting them in an autoclave at elevated temperatures. There is no doubt that surfactants play a significant role

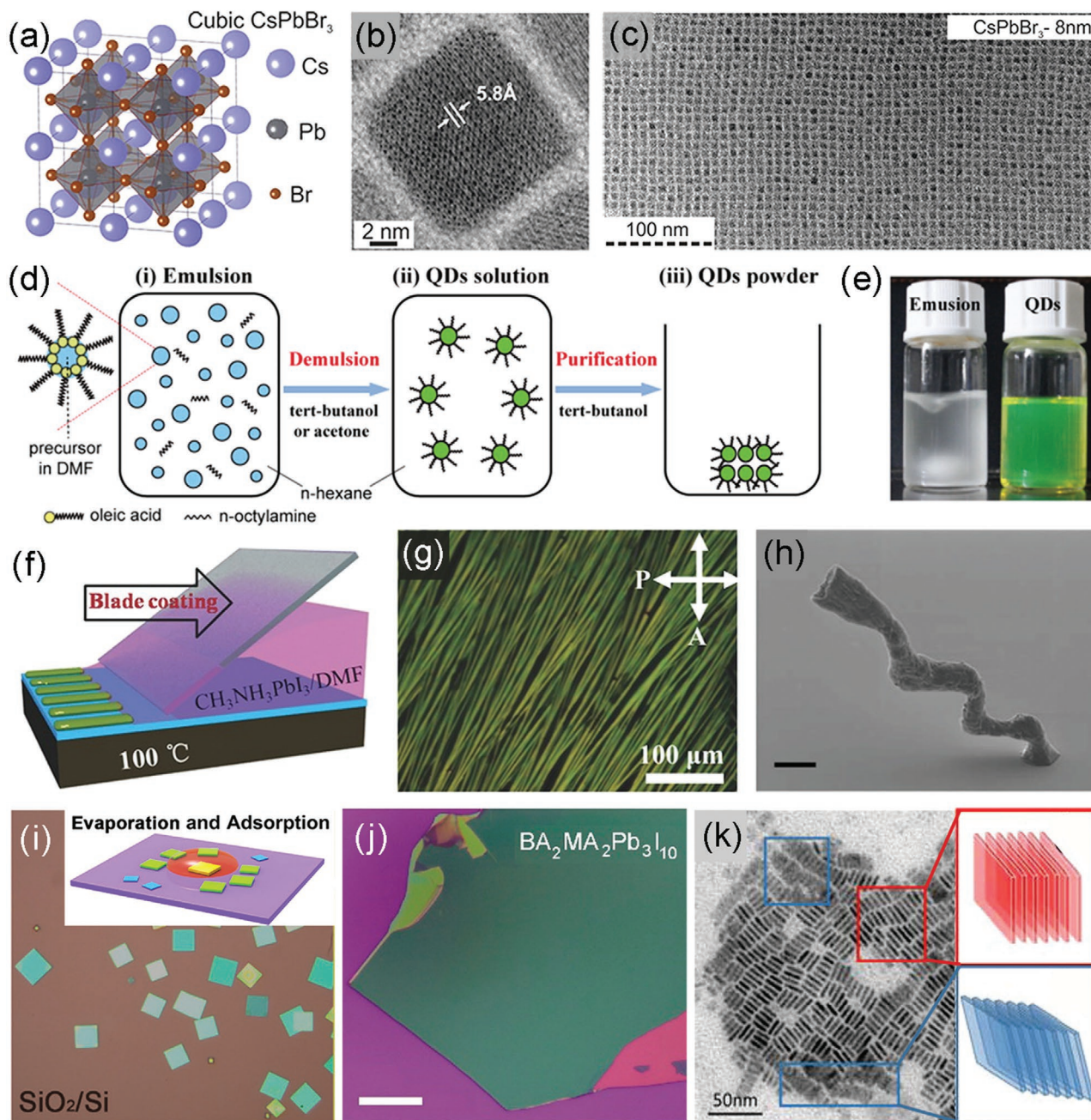


**Figure 1.** Typical low-dimensional MHP nanostructures synthesized by solution-based methods. a) Schematic illustration of CsPbBr<sub>3</sub> lattice. b,c) typical TEM images of monodisperse CsPbBr<sub>3</sub> NCs by hot injection. a–c) Reproduced with permission.<sup>[52]</sup> Copyright 2015, American Chemical Society. d) Schematic illustration of the emulsion synthesis of MAPbBr<sub>3</sub> QDs. e) Optical photographs of MAPbBr<sub>3</sub> emulsion and QD colloidal solution. d,e) Reproduced with permission.<sup>[56]</sup> Copyright 2015, American Chemical Society. f) Schematic illustration of the one-step blade coating method for single-crystalline 1D MAPbI<sub>3</sub> microwire arrays. g) cross-polarized optical image of the perovskite arrays. f,g) Reproduced with permission.<sup>[32]</sup> Copyright 2016, Wiley-VCH. h) A tilted MAPbI<sub>3</sub> serpentine structure prepared by 3D printing (scale bar: 2 μm). Reproduced with permission.<sup>[69]</sup> Copyright 2019, Wiley-VCH. i) The optical image of CsPbBr<sub>3</sub> microflakes on SiO<sub>2</sub> by solvent evaporation. The inset shows the schematic illustration of the growth process. Reproduced with permission.<sup>[72]</sup> Copyright 2017, American Chemical Society. j) The optical image of mechanically exfoliated 2D BA<sub>2</sub>MA<sub>2</sub>Pb<sub>3</sub>I<sub>10</sub> on SiO<sub>2</sub>/Si substrates (scale bar: 20 μm). Reproduced with permission.<sup>[78]</sup> Copyright 2019, American Chemical Society. k) TEM image of face-to-face stacked CsPbBr<sub>3</sub> nanoplatelets by hot injection. Red and blue areas represent nanoplatelets standing perpendicular to and tilted with the substrate, respectively. Reproduced with permission.<sup>[84]</sup> Copyright 2016, American Chemical Society.

in directed 1D growth mechanisms, but they are not necessarily required in solution-based syntheses of 1D MHPs. For instance, a solvent evaporation-induced crystallization method

was developed to achieve the anisotropic growth of 1D MAPbI<sub>3</sub>, producing NWs with the length up to 10 μm.<sup>[65]</sup> The saturated precursor is sandwiched between two glass substrates, and

the supersaturation-driven crystallization of MHP NWs happens during the relative motion of the glass substrates. After that, Deng et al. modified the solvent evaporation technique and introduced a blade coating method to prepare aligned single-crystalline perovskite microwire arrays (Figure 1f,g).<sup>[32]</sup> For the above surfactant-free preparation of 1D MHPs, the growth-directing role of the solvent *N,N*-dimethylformamide (DMF) and strong intermolecular interaction of perovskites are the possible causes of the preferential growth during solvent evaporation. Moreover, using ordered or prepatterned templates, such as anodized aluminum oxide (AAO) templates and polydimethylsiloxane (PDMS) nanochannels, is also an effective approach for the confined growth of 1D perovskite NWs.<sup>[66,67]</sup> In addition, many novel solution-based bottom-up synthetic strategies have been reported for the synthesis of 1D MHP nanostructures. For example, Tsai et al. fabricated uniform perovskite–polymer core–shell nanofibers with diameters of hundreds of nanometers using a one-step electrospinning technique.<sup>[68]</sup> The size and luminescent color of the core–shell nanofibers can be tuned easily by the perovskite composition and the polymer concentration, and the hydrophobic polymer shell provides better stability for MHP nanofibers. Chen et al. creatively introduced a nanoprecision 3D printing method into producing organic–inorganic hybrid MHP nanoarchitectures.<sup>[69]</sup> At the nanopipette tip, the precursor ink forms a femtoliter meniscus to guide the evaporation-induced perovskite crystallization. By controlling the printing parameters, freeform and freestanding MHP structures could be fabricated by the additive manufacturing technique, including NWs, nanowalls, meshes, and serpentine structures (Figure 1h).

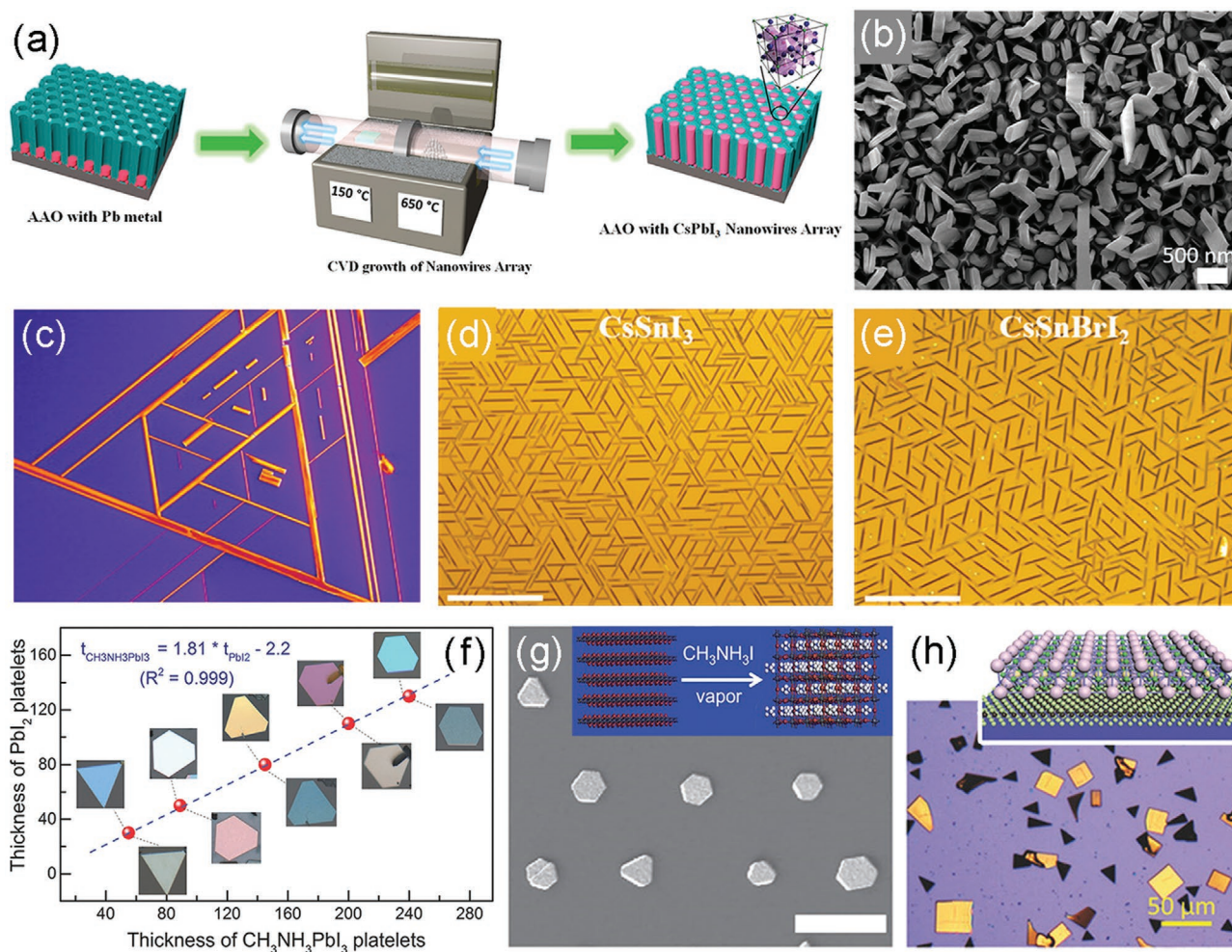
In recent years, by precisely introducing long-chain organic cations and controlling the stoichiometry, 2D layered Ruddlesden–Popper (RP) MHPs provide a variety of intriguing properties.<sup>[70]</sup> In this part, instead of discussing RP phase MHP thin films or single crystals, we mainly focus on the synthesis of MHPs with 2D morphologies, such as NSs and nanoplatelets. Solution-based methods are equally important for the synthesis of 2D MHP nanostructures, including both bottom-up and top-down approaches. Ultrathin 2D MHP NSs can be prepared by simply dropping precursor solution on substrates and subsequently evaporating the solvent (Figure 1i).<sup>[71,72]</sup> And poor solvents can be added into the precursor solution to assist the precipitation of 2D MHP nanostructures. Zhang et al. synthesized (PEA)<sub>2</sub>PbI<sub>4</sub> (PEA = C<sub>8</sub>H<sub>9</sub>NH<sub>3</sub>) NSs with a thickness down to 1.6 nm by adding toluene the poor solvent into the precursor solution and then evaporating the solvents after drop-casting.<sup>[73]</sup> Free-standing (PEA)<sub>2</sub>PbI<sub>4</sub> NSs could be produced by a similar technique, which involves dropping DMF precursor solution into toluene under stirring, producing NSs with an average lateral size and thickness of 531 ± 62 nm and 2.0 ± 0.1 nm, respectively.<sup>[74]</sup> Besides, Chen et al. found some polar solvents in solution systems could effectively suppress the crystal growth in the *c* axis, leading to ultrathin 2D MHPs on substrates after solvent evaporation.<sup>[75]</sup> As for top-down methods, exfoliation is a unique method for the synthesis of ultrathin 2D MHP structures from their layered bulk counterparts. Mechanical exfoliation possesses the advantage of producing 2D MHPs with ultrathin thickness and high quality,<sup>[76–78]</sup> with an example of exfoliated BA<sub>2</sub>MA<sub>2</sub>Pb<sub>3</sub>I<sub>10</sub> (BA = CH<sub>3</sub>(CH<sub>2</sub>)<sub>3</sub>NH<sub>3</sub>) shown in

Figure 1j. By contrast, liquid exfoliation is a low-cost and scalable method to produce large quantities of colloidal NSs.<sup>[43]</sup> This process, which usually involves ligand intercalation and sonication, lacks precise control of the size and thickness of 2D products. To this end, much effort has been made to improve the liquid exfoliation technique, such as ligand/solvent selection and controlled centrifugation, helping produce 2D MHPs with higher quality and better thickness selection.<sup>[79,80]</sup>

Apart from RP type MHPs with layered structure, 2D nonlayered MHP nanostructures were also prepared through various solution-based processes. Similar to the synthesis of MHP NCs, the hot injection method has been applied to produce colloidal 2D MHP NSs. At elevated temperature, the cation precursor is injected into the metal salt (MX<sub>2</sub>) solution containing ligands such as OA and OLA.<sup>[81]</sup> Teunis et al. found that a variety of MAPbBr<sub>3</sub> morphologies, from quantum cubes to large sheets, can be obtained by precisely controlling the combination of solvent systems, surface ligands, and reaction temperature via hot-injection method.<sup>[82]</sup> Recently, Klein et al. reported a modified hot-injection method to produce colloidal MAPbX<sub>3</sub> NSs with size up to micrometer scale, by dissolving PbX<sub>2</sub> NSs as precursors before the injection and carefully controlling process parameters.<sup>[83]</sup> Similar injection methods can also be applied to prepare 2D all-inorganic MHPs with various morphologies, such as CsPbBr<sub>3</sub> nanostructures (Figure 1k).<sup>[84]</sup> Recently, a space-confined growth strategy was applied to the synthesis of single-crystalline CsPbCl<sub>3</sub> microplatelets.<sup>[85]</sup> The researchers covered the precursor solution on a Si/SiO<sub>2</sub> substrate with another substrate, leaving a confined narrow space for MHP microplatelets to grow. After moving the two clipped substrates into the antisolvent (toluene) vapor, large and highly crystalline CsPbCl<sub>3</sub> microplatelets form between the substrates. In addition, some top-down approaches have also been developed for 2D nonlayered MHPs. For example, Tong et al. reported the formation of 2D MAPbBr<sub>3</sub> nanoplatelets via fragmentation of perovskite NCs by simply diluting a dispersion of those NCs, during which the osmotic pressure-induced effect comes into play.<sup>[86]</sup> Those nanoplatelets are highly luminescent, and the PL emission shows a blue-shift with increasing dilution level because of an increased exciton binding energy (*E<sub>b</sub>*).

### 3.1.2. Vapor Synthesis

Compared with solution-based synthesis methods, vapor-phase approaches are considered to produce MHP nanostructures with higher crystallinity and lower defect density,<sup>[87,88]</sup> which is beneficial to their charge transport and PD applications. Chemical vapor deposition (CVD), a crucial method to grow low-dimensional materials, can be employed in preparing 1D MHP structures.<sup>[89,90]</sup> Waleed et al. synthesized CsPbI<sub>3</sub> NWs inside an AAO template by CVD, and the growth process was performed in a tube furnace with two heating zones.<sup>[90]</sup> As is shown in Figure 2a, CsI precursor is placed at the higher temperature zone at 650 °C, and the prepared AAO membrane with Pb metal precursor deposited on its bottom is placed at the downstream low-temperature side (150 °C). CsI vapor is carried to the low-temperature zone by argon gas to form CsPbI<sub>3</sub> NWs inside the pores of AAO template (Figure 2b). Apart from



**Figure 2.** Typical low-dimensional MHP nanostructures synthesized by vapor-based methods. a) Schematic illustration of CsPbI<sub>3</sub> NWs prepared by chemical vapor diffusion of CsI using an AAO template. b) The top view SEM image of CsPbI<sub>3</sub> NWs coming out of AAO. a,b) Reproduced with permission.<sup>[90]</sup> Copyright 2017, American Chemical Society. c) The optical image of CsPbX<sub>3</sub> nanowire arrays prepared by vapor-phase epitaxy on mica substrate. Reproduced with permission.<sup>[91]</sup> Copyright 2016, American Chemical Society. The optical images of the as-grown d) CsSnI<sub>3</sub> and e) CsSnBrI<sub>2</sub> NW arrays by solid-source CVD method (scale bars: 100 μm). d,e) Reproduced with permission.<sup>[93]</sup> Copyright 2019, American Chemical Society. f) The images and thickness of PbI<sub>2</sub> templates (above data line) and CH<sub>3</sub>NH<sub>3</sub>PbI<sub>3</sub> nanoplatelets after being thermally intercalated by methyl ammonium halides (below data line). Reproduced with permission.<sup>[94]</sup> Copyright 2014, Wiley-VCH. g) The SEM image of CH<sub>3</sub>NH<sub>3</sub>PbI<sub>3</sub> microplatelet arrays fabricated by the intercalation of lithographically patterned PbI<sub>2</sub> precursor microplates (scale bar: 20 μm). The inset shows the schematic illustration of vapor-phase intercalation. Reproduced with permission.<sup>[96]</sup> Copyright 2015, AAAS. h) The optical image of CsPbBr<sub>3</sub>/MoS<sub>2</sub> van der Waals heterostructure and the corresponding schematic diagram. Reproduced with permission.<sup>[100]</sup> Copyright 2018, Wiley-VCH.

template-assisted methods, 1D MHPs can also directly grow on certain substrates by evaporating two sources simultaneously. For example, all-inorganic CsPbX<sub>3</sub> and CsSnX<sub>3</sub> single-crystalline NWs and NW arrays could be prepared without templates on various substrates, such as Si and mica (Figure 2c–e).<sup>[87,91–93]</sup>

For the vapor-phase synthesis of 2D MHP structures, methods based on converting PbX<sub>2</sub> NS templates into perovskites have been developed, which involve the intercalation of 2D PbX<sub>2</sub> structures by vapor MAX molecules.<sup>[94]</sup> A variety of chemical and physical approaches have been applied to produce 2D PbX<sub>2</sub> templates, opening opportunities for subsequent chemical conversion. For example, Ha et al. prepared PbX<sub>2</sub> NSs by van der Waals epitaxial growth on mica substrates, and found that after vapor conversion, the thickness of MAPbI<sub>3</sub> NSs is proportional to that of corresponding PbI<sub>2</sub>

templates (Figure 2f).<sup>[94]</sup> Liu et al. adopted a solution-based process to prepare 2D PbI<sub>2</sub> templates, by hot casting saturated precursor solution on substrates.<sup>[95]</sup> After that, 2D MAPbI<sub>3</sub> NSs with thickness down to a single unit cell were successfully synthesized by the vapor-phase conversion of PbI<sub>2</sub> templates. Furthermore, by using prepatterned substrates to prepare PbI<sub>2</sub> template arrays, large-area and regular MHP microplatelet arrays can be achieved for optoelectronic applications after the chemical conversion (Figure 2g).<sup>[96]</sup> Apart from those two-step methods using PbX<sub>2</sub> templates, single-step vapor-phase approaches have been utilized for the synthesis of all-inorganic 2D perovskite structures. For example, Hu et al. prepared CsPbBr<sub>3</sub> nanoplates by heating and evaporating mixed source powders of PbBr<sub>2</sub> and CsBr.<sup>[97]</sup> CsPbBr<sub>3</sub> nanoplates with lateral size up to a few tens of micrometers are formed on substrates

positioned at the downstream side of the tube. Moreover, the vapor-phase epitaxial growth has been developed for the preparation of high-quality 2D MHP crystals, which avoids the lattice matching restriction between perovskites and substrates. Huo et al. achieved van der Waals epitaxy of ultrathin CsPbX<sub>3</sub> platelets by evaporating mixed precursors of CsX and PbX<sub>2</sub>.<sup>[98]</sup> With the effect of substrate surface dangling bonds eliminated, CsPbX<sub>3</sub> platelets grown on fluorophlogopite mica substrates show high crystal quality and can be easily transferred to other substrates for subsequent device fabrication. Similarly, 2D CsPbBr<sub>3</sub> crystals are epitaxially grown on multifunctional substrates such as SrTiO<sub>3</sub>.<sup>[99]</sup> And, CsPbBr<sub>3</sub>/2D material van der Waals heterostructures are fabricated by van der Waals epitaxy for optoelectronic applications, such as CsPbBr<sub>3</sub>/MoS<sub>2</sub> heterostructure (Figure 2h).<sup>[100]</sup>

### 3.2. Optical Properties

The properties of MHP polycrystalline films and bulk single crystals have been intensively studied in recent years. Many unique and intriguing properties, including broad and tunable absorption, high luminescence quantum yield, and superior charge transport properties, make them attractive for advanced photovoltaic and optoelectronic devices.<sup>[101–103]</sup> Although studies on the properties of low-dimensional MHPs are fewer compared with those on their bulk counterparts, their rich chemistry and fascinating properties are now being gradually discovered. In this part, we focus on the basic concepts and recent advances in the study of their optical properties.

The light absorption is the first stage of the light–matter interaction, which is crucial to MHPs' unique optical properties and their diverse applications. It is found that polycrystalline MHPs and bulk single crystals show the advantage of a high light absorption coefficient (10<sup>4</sup>–10<sup>5</sup> cm<sup>-1</sup> for hybrid perovskites) in a broad spectral range, from UV to NIR.<sup>[104–106]</sup> Therefore, a thin layer (hundreds of nanometers) of MHPs could effectively absorb the incident light, which is necessary for a high photo-carrier conversion efficiency in optoelectronic devices.<sup>[104,107]</sup> Similarly, a high light absorption coefficient has been observed in MHPs with reduced dimensions. Zhang et al. observed strong excitonic absorption (~55%) and high absorption coefficients (>10<sup>5</sup> cm<sup>-1</sup>) in thick (PEA)<sub>2</sub>PbI<sub>4</sub> and (C<sub>4</sub>H<sub>9</sub>NH<sub>3</sub>)<sub>2</sub>PbI<sub>4</sub> nanoflakes (≥20 L).<sup>[73]</sup> Moreover, the light absorption of MHPs can be tuned by controlling chemical composition and dimensionality, providing great flexibility to broad applications.

After the light absorption, the generation of excitons and the dissociation of excitons into free charge carriers play a significant role in MHPs. The carrier dynamics and the performance of MHP-based optoelectronic devices are inextricably linked with the photoexcited species and their behavior. For excitons, the electron–hole pair binding strength is determined by the  $E_b$ . To date, various experimental techniques have been developed to measure the  $E_b$  of MHPs, such as the optical absorption and the temperature-dependent PL.<sup>[108,109]</sup> For bulk MAPbI<sub>3</sub>, the value of  $E_b$  was reported to range from a few meV to >50 meV,<sup>[109–112]</sup> and substituting iodide with bromide or chloride would give rise to higher  $E_b$ .<sup>[112–114]</sup> Since the thermal ionization energy at room temperature (RT) is around 26 meV,

Wannier excitons and free charge carriers may coexist in bulk MHPs at RT.<sup>[115]</sup> But some in-depth studies indicated that although the  $E_b$  may vary over a wide range at RT, free charge carriers are generated upon light illumination by fast dissociation of excitons, leading to a nonexcitonic behavior of these perovskites.<sup>[111,114,116,117]</sup> Such nonexcitonic behavior would lead to high charge collection efficiency for MHP-based PDs.

In the case of low-dimensional MHPs, the optical properties are more complex compared with those of their bulk counterparts. For perovskite nanostructures, the  $E_b$  is highly relevant to their size and dimensions because of confinement effects. An early attempt to theoretically calculate the  $E_b$  of low-dimensional Pb iodide MHP systems suggested that the  $E_b$  of Wannier excitons varies from ≈130 to 720 meV for different dimensions.<sup>[110]</sup> When decreasing the size of MHP NCs down to a scale that is close to the exciton Bohr radius, the  $E_b$  increases and can reach hundreds of meV.<sup>[52,54]</sup> For 1D NWs, Zhang et al. observed strong confinement effect in ultrathin CsPbBr<sub>3</sub> NWs with diameters of ≈2.2 nm, which is below the exciton Bohr radius.<sup>[118]</sup> After that, Zhang et al. prepared high density 1D MAPbI<sub>3</sub> NW arrays with variable diameters from ≈250 to ≈5.7 nm using porous alumina membrane templates.<sup>[119]</sup> With the diameters of NWs decreasing, quantum confinement is gradually introduced, and consequently the blueshift of PL spectra and decreased PL lifetime are observed. An increase of up to 42.6% in PLQY is also observed, which may be attributed to strong quantum confinement and low surface recombination of MAPbI<sub>3</sub> NWs. More recently, 2D RP type MHPs have gained much research interest owing to their unique layered structure. Typically, a RP type hybrid MHP series has the formula of A'<sub>2</sub>A<sub>n-1</sub>M<sub>n</sub>X<sub>3n+1</sub> ( $n = 1$  to  $\infty$ ), where A', A, M, and X refer to long-chained spacer cation, smaller organic cation, metal cation, and halide anion, respectively. Those organic–inorganic hybrid perovskites consist of MX<sub>6</sub> slabs separated by long-chain organic cation layers, forming the structure of multiple quantum wells.<sup>[120]</sup> On the one hand, the motion of charge carriers is limited within the quantum wells, giving rise to improved Coulomb interaction between electrons and holes. With the MX<sub>4</sub> layer thickness decreasing, quantum confinement becomes increasingly obvious in RP hybrid MHPs, resulting in the increased binding energy.<sup>[121,122]</sup> On the other hand, the organic cation layers between perovskite slabs would lower the dielectric constant in RP MHPs, further improving the Coulomb interaction between electron–hole pairs.<sup>[123]</sup> Many researchers have been focusing on the nature of photoexcited species in 2D perovskites, both theoretically and experimentally, giving new insights into their excitonic behavior.<sup>[124–126]</sup> Owing to the quantum confinement and dielectric enhancement effect, low-dimensional MHPs possess much higher  $E_b$  than that of 3D bulk counterparts.

The high absorption coefficient, as well as high  $E_b$  in low-dimensional MHPs, provides great possibilities for their light emission applications.<sup>[127,128]</sup> And the reduced dimension of low-dimensional MHPs decreases the exciton diffusion length and increases the possibility of radiative recombination of excitons.<sup>[129]</sup> Figure 3a,b shows strong bluish-white light emission of 1D bulk C<sub>4</sub>N<sub>2</sub>H<sub>14</sub>PbBr<sub>4</sub> crystals under UV light illumination.<sup>[128]</sup> For 2D RP type MHPs, organic cation layers between perovskite slabs can greatly decrease their defect



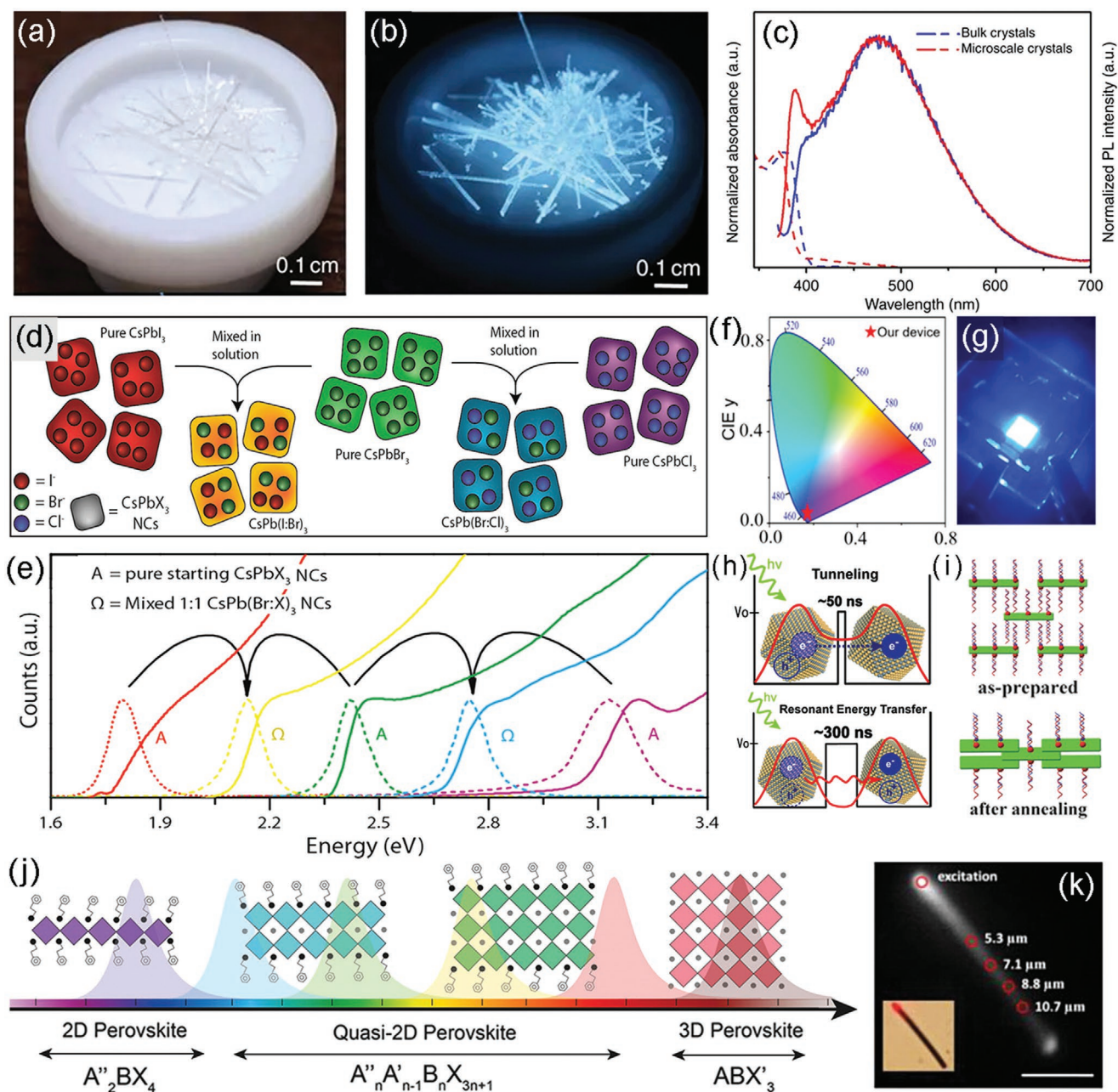


**Figure 3.** a) The image of needle-shaped bulk  $C_4N_2H_{14}PbBr_4$  crystals under ambient light. b) The crystals in (a) show strong bluish white-light emission under 365 nm UV light. c) The absorption (dash lines) and emission (solid lines) spectra of the needle-shaped bulk and 1D microscale  $C_4N_2H_{14}PbBr_4$  crystals. a–c) Reproduced under the terms of the CC-BY 4.0 license.<sup>[128]</sup> Copyright 2017, the Authors, published by Springer Nature. d) The schematic illustration of interparticle anion exchange among  $CsPbX_3$  perovskite NCs. e) The absorption and PL spectra of  $CsPb(Br_{1-x}Cl_x)_3$  and  $CsPb(Br_{1-x}I_x)_3$  NCs prepared by interparticle anion exchange. d,e) Reproduced with permission.<sup>[132]</sup> Copyright 2015, American Chemical Society. f) CIE color coordinates and g) photograph of a deep-blue LED based on 2D (PEA)<sub>2</sub>PbBr<sub>4</sub> nanoplates. Reproduced with permission.<sup>[131]</sup> Copyright 2019, Wiley-VCH. h) The illustration of the dominant exciton dissociation pathway via tunneling when interparticle distance is short and the coupling energy is high. When coupling energy decreases, the resonant energy transfer becomes dominant. Reproduced with permission.<sup>[142]</sup> Copyright 2010, American Chemical Society. i) The illustration of increased  $CsPbBr_3$  inter-NS coupling resulting from ligands rearrangement by annealing. Reproduced with permission.<sup>[138]</sup> Copyright 2018, Wiley-VCH. j) Schematic illustration of tuning the bandgap of perovskites by dimensionality engineering. Reproduced with permission.<sup>[182]</sup> Copyright 2018, Wiley-VCH. k) PL intensity image shows the carrier diffusion in an individual single-crystalline MAPbI<sub>3</sub> NW (scale bar: 5  $\mu$ m). Reproduced with permission.<sup>[156]</sup> Copyright 2015, American Chemical Society.

density and improve the PLQY because competitive nonradiative recombination at defects is obviously suppressed.<sup>[106,130]</sup> As a consequence, deep-blue LEDs based on RP type perovskite

NSs can be achieved (Figure 3f,g) because of the large  $E_b$  and improved stability, making them promising alternatives for wide bandgap emitters such as GaN.<sup>[131]</sup> In addition, the light

emission of low-dimensional MHPs can be precisely tuned by adjusting their chemical composition. For example, the PL property of CsPbX<sub>3</sub> NCs can be continuously adjusted in the visible range by controlled synthesis and anion exchange reaction (Figure 3d).<sup>[52,132]</sup> What's more, the high PLQY of low-dimensional MHPs makes it easier to investigate the exciton behavior and energy states by PL spectroscopy. In PL spectra of 1D C<sub>4</sub>N<sub>2</sub>H<sub>14</sub>PbBr<sub>4</sub> NWs shown in Figure 3c, free excitons yield narrowband emission with a shorter wavelength, and the lower energy broadband emission can be attributed to self-trapped excitons.<sup>[128]</sup> And, the role of energy funnels in the enhanced emission of quasi-2D MHPs was successfully identified using steady-state and time-resolved PL (TRPL) spectroscopy, respectively.<sup>[133]</sup> Moreover, similar to their bulk counterparts, low-dimensional MHPs show interesting nonlinear optical properties. Li et al. synthesized 2D MAPbI<sub>3</sub> NSs and then investigated their nonlinear optical properties.<sup>[134]</sup> They found MAPbI<sub>3</sub> NSs exhibit a higher nonlinear absorption coefficient than that of MoS<sub>2</sub> and graphene, as well as lower saturable intensity than that of MoS<sub>2</sub> and bulk perovskite, which favor potential applications in ultrafast pulsed lasers. Other researchers discovered that CsPbBr<sub>3</sub> NCs can act as multiphoton pumped optical gain media for nonlinear photonics.<sup>[135]</sup>

### 3.3. Optoelectronic Properties

In addition to the excellent absorption coefficient and emission properties, the optoelectronic properties of low-dimensional MHPs are equally intriguing. Their outstanding optoelectronic properties, such as high carrier mobility, long diffusion length, and efficient charge carrier collection, are beneficial for the development of advanced optoelectronic devices.<sup>[22,136]</sup> Nowadays, with a deeper understanding of the optoelectronic properties, much research has been done to optimize the properties for better performance, and devices with high sensitivity and fast response speed based on low-dimensional MHPs are being developed.

#### 3.3.1. Carrier Generation

As discussed above, the generation and dissociation of excitons are vital for both the carrier transport properties of MHPs and the development of high-performance optoelectronic devices based on them. It has been reported that after photon absorption, photogenerated excitons in bulk MHPs dissociate into free carriers within several picoseconds, leading to excellent optoelectronic properties.<sup>[137]</sup> For low-dimensional MHPs, although their high  $E_b$  is favorable for the light emission applications, such a characteristic blocks the generation of free carriers at RT, which limits their applications in high-performance PDs, solar cells, and other optoelectronic devices.<sup>[138–140]</sup> To solve this problem, much effort has been made to lower the  $E_b$  or facilitate the charge carrier separation. Li et al. reported the doping of RP perovskite (BA)<sub>2</sub>(MA)<sub>3</sub>Pb<sub>4</sub>I<sub>13</sub> by Li<sup>+</sup> ions can reduce the dielectric constant difference between organic layers and perovskite slabs, and therefore decreases the dielectric confinement of multiple quantum wells.<sup>[141]</sup> The method of

Li<sup>+</sup> doping not only decrease the  $E_b$ , but also improve the carrier mobility of the perovskite. Recently, Gao et al. employed first-principle calculations to search for ways to decrease the  $E_b$  in atomically thin 2D RP MHP series (BA)<sub>2</sub>(MA)<sub>*n*-1</sub>Pb<sub>*n*</sub>X<sub>3*n*+1</sub> (*n* = 1 and 2).<sup>[140]</sup> They predicted that by introducing neutral Pb vacancies into the lattice of the MHP series, the  $E_b$  could be lowered significantly for the generation of free carriers. In addition, some other investigations focused on the case of low-dimensional nanostructure assemblies where the interaction between individual nanostructures comes into play. Choi et al. found that excitons in lead salt NC assemblies can spontaneously tunnel through the potential barriers between NCs to dissociate when the electronic coupling energy is comparable to or larger than the  $E_b$  (Figure 3h).<sup>[142]</sup> Based on that, the coupling energy is successfully increased by partially removing the ligands in CsPbBr<sub>3</sub> NSs via annealing (Figure 3i), resulting in a higher exciton dissociation efficiency and higher photoreponse of devices.<sup>[138]</sup> Furthermore, the dissociation of excitons in low-dimensional MHPs can be enhanced by fabricating heterostructures with other 2D materials, such as graphene and MoS<sub>2</sub>.<sup>[101,143]</sup> Those MHP-2D material heterostructures facilitate the interfacial charge transport, providing those hybrid devices with both high absorption efficiency and improved carrier collection.

Among the most exciting features of low-dimensional MHPs, high surface-to-volume ratio and the loss of symmetry provide their surface and edges with distinct properties from those of the interior. For the optoelectronic properties of layered RP MHPs, their rich photophysics becomes even more intriguing when it comes to their edge states. Nowadays, cutting-edge characterization and measurement technologies give us better insights into the effect of edge states on the generation of free charge carriers. Blancon et al. investigated the edges of mechanically exfoliated few-layer RP type perovskite (BA)<sub>2</sub>(MA)<sub>*n*-1</sub>Pb<sub>*n*</sub>I<sub>3*n*+1</sub>.<sup>[124]</sup> They found the lower-energy edge states are conducive to the dissociation of excitons into free carriers, and can protect carriers from recombination through nonradiative processes, which contribute to the enhanced performance for both photovoltaic and light emission applications. After that, RP perovskite (BA)<sub>2</sub>(MA)<sub>*n*-1</sub>Pb<sub>*n*</sub>I<sub>3*n*+1</sub> (*n* = 2–5) was used by Feng et al. to fabricate single-crystalline NW array-based PDs.<sup>[31]</sup> The length direction of fabricated MHP NWs is perpendicular to the perovskite slabs, and photoexcited excitons efficiently diffuse to the edge of NWs and dissociate into free carriers, contributing greatly to the photocurrent of NW arrays. Furthermore, Shi et al. found that the PL peaks of 2D RP perovskite edges change after prolonged exposure to air.<sup>[78]</sup> After careful investigation, they deduced that the edge states in 2D MHPs are of extrinsic nature and can be triggered by an extremely low concentration of moisture (≈0.5 ppm). Those edge states can effectively facilitate the dissociation of excitons into free carriers with both long lifetime and high mobility. More recently, Wang et al. reaffirmed the role of lower-energy edge states in RP type MHP (C<sub>4</sub>H<sub>9</sub>NH<sub>3</sub>)<sub>2</sub>PbI<sub>4</sub>, and they observed the extraordinarily conducting layer edges of the MHP with an ultrahigh carrier density of ≈10<sup>21</sup> cm<sup>-3</sup>.<sup>[144]</sup> All those discoveries above demonstrate the distinct carrier generating properties of low-dimensional MHPs, paving ways for future research and device development.

### 3.3.2. Carrier Transport

The superior charge transport properties of MHPs have been well studied by many researchers, making them outstanding candidates for various optoelectronic applications. Generally, the charge transport process consists of two mechanisms, namely, carrier diffusion and carrier drift. The carrier diffusion is the motion of carriers driven by the carrier density gradient in semiconductors, and it usually does not involve an external electric field.<sup>[145]</sup> Without external field, the diffusion length ( $L_D$ ) is determined by the charge diffusion coefficient  $D$  and the charge carrier lifetime  $\tau$ <sup>[146]</sup>

$$L_D = \sqrt{D\tau} \quad (6)$$

A number of studies have shown that MHPs exhibit long carrier lifetime, which would contribute to their long carrier diffusion length before the recombination.<sup>[147]</sup> Because of the effect of grain boundary, the carrier diffusion length in polycrystalline thin films is in the range from 100 nm to a few  $\mu\text{m}$ , whereas MHP single crystals can exhibit the  $L_D$  of more than 100  $\mu\text{m}$ .<sup>[22,148,149]</sup> Besides, the carrier mobility is a vital parameter for charge carrier drift motion under an external electric field. Measured by various techniques, the charge carrier mobility of MHPs can vary greatly, even for the MHPs with the same chemical composition.<sup>[109]</sup> And because of the effect of scattering, it is reported the measured mobility of MHP thin films is relatively lower than that of single crystals.<sup>[109,150,151]</sup> For bulk MHPs, their carrier mobility is higher than that of some organic semiconductors but not comparable to some inorganic semiconductors such as Si and GaAs, owing to some intrinsic and extrinsic effects.<sup>[152,153]</sup>

In recent years, studies on the carrier transport properties of low-dimensional MHPs, although fewer than those of polycrystalline films and bulk single crystals, continue to burgeon. Some advanced measurement techniques have been developed for low-dimensional MHPs and a variety of interesting discoveries were made.<sup>[154]</sup> In contrast to bulk polycrystalline films, low-dimensional MHPs generally have higher crystallinity, fewer defects and grain boundaries.<sup>[88]</sup> Therefore, some low-dimensional MHP nanostructures exhibit relatively long carrier diffusion length and high carrier mobility, resulting in excellent charge transport properties.<sup>[32,88,155]</sup> For 0D halide perovskites, Yettapu et al. reported that the trapping effects of surface defects in colloidal CsPbBr<sub>3</sub> NCs are negligible, leading to their ultrahigh carrier mobility ( $\approx 4500 \text{ cm}^2 \text{ V}^{-1} \text{ s}^{-1}$ ) and large diffusion length ( $>9.2 \mu\text{m}$ ).<sup>[127]</sup> The high mobility and large diffusion length make CsPbBr<sub>3</sub> unique among colloidal NCs. Deng et al. utilized scanning photocurrent microscopy to measure the diffusion length of aligned 1D single-crystalline MAPb(Br<sub>x</sub>I<sub>1-x</sub>)<sub>3</sub> NW arrays prepared by template-assisted growth.<sup>[155]</sup> A long carrier diffusion length of  $\approx 41 \mu\text{m}$  is obtained in the MAPbI<sub>3</sub> NW arrays, higher than that of Si NWs and even some MAPbI<sub>3</sub> single crystals. Tian et al. achieved the visualization of carrier diffusion in individual MAPbBr<sub>3</sub> and MAPbI<sub>3</sub> NWs and nanoplates using time-resolved and PL-scanned imaging microscopy, and a typical image is shown in Figure 3k.<sup>[156]</sup> The measured average diffusion length is  $\approx 6$  and  $\approx 14 \mu\text{m}$  for MAPbBr<sub>3</sub> and MAPbI<sub>3</sub>, respectively. And, the carrier mobility ranges from 19.4 to

56.1  $\text{cm}^2 \text{ V}^{-1} \text{ s}^{-1}$  for MAPbBr<sub>3</sub> and 56.4 to 93.9  $\text{cm}^2 \text{ V}^{-1} \text{ s}^{-1}$  for MAPbI<sub>3</sub> nanostructures. Hu et al. later modified the mobility measuring method by applying an electric field when conducting PL imaging and TRPL measurements for hybrid and all-inorganic MHP nanoplates.<sup>[157]</sup> The comet-like PL emission patterns are elongated with the increase of the applied electric field, directly demonstrating the charge carrier drift driven by the electric field. By measuring the PL decay length, they measured the mobility of CsPbBr<sub>3</sub> nanoplates in the range of about 20–30  $\text{cm}^2 \text{ V}^{-1} \text{ s}^{-1}$ . More interestingly, MHPs show unique ambipolar carrier transport properties, and devices based on them are able to work in both the accumulation and inversion modes.<sup>[148,158]</sup> The ambipolar transport properties were also observed in low-dimensional MHPs. Yang et al. observed high carrier mobility in solution-processed CsPbBr<sub>3</sub> microcrystals by fitting PL decay curves, with measured mobility of 109 and 78  $\text{cm}^2 \text{ V}^{-1} \text{ s}^{-1}$  for electron and hole transport, respectively.<sup>[159]</sup> The ambipolar transport properties are favorable for their applications in optoelectronics and transistors.<sup>[160]</sup>

In a bid to use MHPs to best advantage, much effort has been made to improve their charge transport properties in recent years.<sup>[161]</sup> For low-dimensional MHPs, capping ligands are widely used to direct the preferential growth of nanostructures, passivate surface defects, and improve their environmental stability. However, the insulating long alkyl-chain capping ligands in MHP nanostructures block efficient carrier transport and limit the performance of optoelectronic devices. To solve this problem, multiple approaches have been proposed, including ligand design, exchange, and removal. Bi et al. achieved partial ligand exchange for all-inorganic CsPbI<sub>3</sub> QDs by substituting long-chain ligands, i.e., OA and OLA, with the short-chain ligand 2-aminoethanethiol (AET).<sup>[162]</sup> They found the AET-CsPbI<sub>3</sub> QD films exhibit higher electron mobility than that of the untreated CsPbI<sub>3</sub> QD films. Dai et al. replaced conventional insulating capping ligands with a conjugated alkyl-amine as the ligand to prepare MAPbBr<sub>3</sub> QDs.<sup>[163]</sup> Due to the delocalization effect of conjugated molecules, the QD-based LEDs show greatly enhanced transport properties and good stability, successfully overcoming the trade-off between conductivity and stability. For 2D RP perovskites, the organic cation layers between adjacent conductive inorganic slabs may limit the out-of-plane carrier transport, leading to the reduced efficiency of devices. To this end, researchers have tried to substitute long-chain and insulating organic cations in RP type MHP structures with short-chain alternatives to improve their optoelectronic performance without sacrificing their stability. For example, Dong et al. substituted linear chain BA with branched chain iso-butylamine (iBA) during the synthesis process of RP type MHP films, and observed improved photodetection performance.<sup>[164]</sup> Apart from the ligand exchange methods above, Zhang et al. adopted a mild reaction strategy to remove surface organic ligands on Ni–CsPbX<sub>3</sub> NCs.<sup>[165]</sup> Unlike conventional ligand-exchange approaches which may introduce surface defects because of the loss of coordinated halide ions, the mild reaction involves using thionyl halide (SOCl<sub>2</sub> or SOBr<sub>2</sub>) as passivating agents to coordinate to surface metal cations. The ligand-lacking NCs maintain the original morphology and >80% of the original PLQY, and exhibit obviously improved conductivity than that of as-synthesized ones.

In addition to focusing on capping ligands, controlling the crystalline orientation is another practical strategy to tackle the issue of out-of-plane transport of 2D RP MHPs. Tsai et al. exploited the hot-casting method for the fabrication of photovoltaic devices based on RP MHP  $(\text{BA})_2(\text{MA})_{n-1}\text{Pb}_n\text{I}_{3n+1}$  ( $n = 3$  and  $4$ ).<sup>[70]</sup> Compared with RT casting methods, the perpendicular orientation of perovskite octahedral slabs relative to fluorine-doped tin oxide (FTO) substrates forms direct charge transport channels between the electrodes, without the involvement of insulating spacer layers. The optimized crystalline orientation leads to enhanced charge transport and excellent long-term stability of the devices. After that, Chen et al. went further to investigate the formation mechanism of the RP MHPs with vertical orientation.<sup>[166]</sup> They replaced the solvent DMF with dimethylacetamide (DMAc) to prepare 2D RP MHP  $(\text{BA})_2(\text{MA})_3\text{Pb}_4\text{I}_{13}$  with preferentially vertical orientation. The in situ grazing incidence wide-angle X-ray scattering (GIWAXS) experiments revealed the dominant heterogeneous nucleation process at the precursor liquid–air interface, and this may result from the preferential orientation of organic molecules bound to inorganic slabs at the liquid–air interface. The research suggests the importance of controlling the interface nucleation of low-dimensional MHPs during the preparation process for improved charge transport.

#### 4. Bandgap Engineering

In addition to the excellent optical and optoelectronic properties, the tunable bandgap is one of the most attractive features of MHPs. By controlling the chemical composition, dimensionality, and structure, their broad tunability of bandgap renders them among the most versatile materials for photovoltaic and optoelectronic devices.<sup>[106,139]</sup> For bulk MHPs, their tunable bandgap provides a variety of advantages in optoelectronic applications, such as tunable light emission, tailorable spectral response, wavelength-selective photodetection, and better band alignment in heterostructures.<sup>[136,167,168]</sup> The properties are even more intriguing for low-dimensional MHPs because of their reduced dimensions and unique structures. Nowadays, bandgap engineering is making significant advances in the field of low-dimensional MHPs to further explore their properties and improve their performance.

For bulk halide perovskites, the tunability of bandgap can be achieved by changing their chemical composition. Considering the chemical formula of the MHP family, it is known that the substitution of either cations or anions can influence the electronic structure of MHPs and hence induce changes in their bandgap. As the hybridization between Pb-6s and halogen p orbitals governs the valence band maximum (VBM), changing halide anions or adjusting their ratios is the most commonly used bandgap engineering strategy by changing chemical composition.<sup>[169]</sup> Generally, substituting iodide with bromide and chloride can increase the bandgap of MHPs.<sup>[52,105,170]</sup> Therefore, by adjusting the halide ratio, the absorption edge can be tuned over a wide spectrum range, from UV (for  $\text{MAPbCl}_3$ ) to NIR (for  $\text{MAPbI}_3$ ).<sup>[136]</sup> This rule is also applicable to low-dimensional MHPs with various dimensions. In 2015, Akkerman et al. demonstrated the exciting possibility for bandgap engineering

of 0D  $\text{CsPbX}_3$  NCs ( $\approx 9$  nm) by halide anion exchange.<sup>[132]</sup> By simply adding another lead halide salt or  $\text{CsPbX}_3$  NCs with another halide composition, the halide exchange reaction is performed in solution, which continuously tunes the bandgap of  $\text{CsPbX}_3$  NCs (Figure 3d,e). The anion-exchanged NCs yield sharp PL emission covering the whole visible spectrum. Recently, Ma et al. prepared lead-free colloidal  $\text{Cs}_3\text{Sb}_2\text{X}_9$  QDs with size of about 5 nm by a supersaturation recrystallization method.<sup>[171]</sup> An obvious color change from red to violet was observed in QDs with different halide compositions under UV light, covering a wide wavelength range from 385 to 640 nm. Particularly, violet-emissive  $\text{Cs}_3\text{Sb}_2\text{Br}_9$  QDs show a high PLQY of 51.2%, as well as excellent stability against heat, UV, and moisture. For 1D MHP cases, Deng et al. prepared a series of  $\text{MAPb}(\text{I}_{1-x}\text{Br}_x)_3$  ( $x = 0-0.4$ ) NW arrays with tunable absorption cutoff wavelengths from 780 to 680 nm.<sup>[155]</sup> With the tunable optical properties, broadband PDs with ultrahigh and sequentially tunable photoresponse are achieved based on the MHP NW arrays. After that, Gao et al. extended the halide adjusting range of the  $\text{MAPbX}_3$  NW arrays, whose bandgap can vary in a broader range from 1.7 to 3.1 eV.<sup>[172]</sup> Moreover, free-standing ultrathin 2D RP type  $(\text{PEA})_2\text{PbX}_4$  NSs with tunable bandgap via adjusting the halide ratio were reported.<sup>[74]</sup> The synthesized MHP NSs dispersed in toluene show tunable PL under UV irradiation, with emission color changing from green for  $(\text{PEA})_2\text{PbI}_4$  to violet for  $(\text{PEA})_2\text{PbCl}_4$ .

In recent years, to replace the toxic element Pb at the “B” site of MHPs, lead-free MHPs, including Sn-, Ge-, and Sb-based perovskites have been developed, and the bandgap can be tuned accordingly by adjusting B-site metal cations.<sup>[168,173,174]</sup> Cheng et al. investigated the bandgap engineering of the lead-free hybrid MHP series  $(\text{PEA})_2\text{Ge}_{1-x}\text{Sn}_x\text{I}_4$  ( $x < 0.5$ ) experimentally and theoretically.<sup>[173]</sup> With the  $x$  value increasing, the color of samples turned dark as the bandgap linearly decreased. Similarly, the tunable bandgap, adjustable PL emission, and increased electrical conductivity were observed in all-inorganic MHP  $\text{CsPb}_x\text{Sn}_{1-x}\text{I}_3$  NWs.<sup>[175]</sup> The idea of bandgap engineering via B-site cation substitution is useful not only in tuning the photoresponse spectra, but also in obtaining better bandgap alignment with other materials in heterostructures. For instance, Ji et al. reported the bandgap engineering strategy of Pb–Sn mixed cation MHPs by simulation and experiment to improve the power conversion efficiency of inverted solar cells.<sup>[174]</sup> They found the higher Sn doping concentration results in the decreased bandgap, and at the same time, the rising position of both the VBM and the conduction band minimum (CBM). By optimizing the B-site cation ratio, a better band alignment with the charge transport layers in solar cells would enhance the collection of photogenerated carriers, and eventually improve the device efficiency. However, as substituting Pb with other B-site cations may cause inferior device performance or reduced stability, further research is still needed to tackle the issues.

Besides adjusting halide anions and B-site metal cations, it is also possible to tune the bandgap of MHPs by changing A-site cations, such as MA, FA, and  $\text{Cs}^+$ . Different from band structure engineering by halide substitution, the adjustment of A-site cations has an indirect effect on bandgap by influencing the structural distortion. A-site cations with a smaller size can lead to a more distorted Pb–X–Pb bond angle, and therefore

the position of valence band and conduction band shift upward because of the deformation of antibonding orbitals.<sup>[176]</sup> For example, mixed-cation MHP series  $\text{Cs}_x\text{Rb}_{1-x}\text{PbX}_3$  QDs were synthesized by Baek et al.<sup>[177]</sup> With the increasing amount of smaller  $\text{Rb}^+$  ions, the PL emission peaks of colloidal QDs show a slight blueshift ( $\approx 10$  nm). Theoretical work suggests the substitution of  $\text{Cs}^+$  with  $\text{Rb}^+$  introduces more severe octahedral tilting in MHP structure. The lattice distortion eventually results in the bandgap widening of  $\text{CsPbX}_3$  QDs by  $\text{Rb}^+$  doping. Dong et al. prepared bandgap tunable 1D hybrid perovskite  $\text{Cs}_x(\text{MA})_{1-x}\text{PbI}_3$  NWs via controlling the molar ratio of inorganic and organic A-site cations, and the bandgap could be tuned between 1.5 and 1.72 eV.<sup>[178]</sup> Since the approach of changing A-site cations is considered not as efficient as the method of adjusting halide anions in terms of bandgap engineering, this approach is mainly utilized for the balance between energy conversion efficiency and their structural stability.<sup>[179,180]</sup>

Apart from introducing structural distortion, changing A-site cations can also lead to crystal structure transformation in low-dimensional MHPs and further influence the bandgap. For example, with the unique 2D layered structure, RP type MHP nanostructures offer great flexibility and tunability in terms of bandgap engineering by adjusting A-site organic cations. The long-chained spacer cation layers separate the inorganic octahedral slabs, forming the structure of multiple quantum wells.<sup>[120]</sup> By adjusting the ratio of spacer cations and small cations like  $\text{MA}^+$ , the thickness of inorganic octahedral slabs (i.e., the  $n$  in the chemical formula) could be tuned, making bandgap engineering possible.<sup>[122,181]</sup> Figure 3j illustrates the bandgap engineering of RP type MHPs by changing the layer thickness,<sup>[182]</sup> and higher layer thicknesses can result in the redshift of light absorption and emission. Stoumpos et al. theoretically and experimentally investigated the effect of the spacer cation on the bandgap of RP type perovskite  $(\text{BA})_2(\text{MA})_{n-1}\text{Pb}_{n-1}\text{I}_{3n+1}$ .<sup>[181]</sup> By increasing the amount of bulky butylammonium cations, the optical absorption edge of the MHP series shows an obvious blueshift with the decreasing  $n$  value. The relationship between bandgap and  $n$  was reaffirmed by the density functional theory (DFT) calculation, when the energy of CBM becomes higher as  $n$  decreases, leading to the improved bandgap.<sup>[181]</sup> This layer thickness-controlling approach has been also applied to tune the bandgap of other RP perovskite series, such as Sn-based MHPs, and even newly discovered Dion–Jacobson organic–inorganic hybrid MHPs.<sup>[183,184]</sup> Besides, Zhang et al. discovered that without changing the thickness  $n$ , just stacking monolayer RP MHP  $(\text{C}_4\text{H}_9\text{NH}_3)_2\text{PbI}_4$  ( $n = 1$ ) into few-layer NSs would lead to a slight decrease of their optical bandgap.<sup>[73]</sup> In addition to changing the thickness of inorganic slabs in RP type MHPs, organic ligands also have an important effect on their crystal structure and the bandgap in other ways. Kamminga et al. replaced the MA cations in  $\text{MAPbI}_3$  by phenylalkylamines with various alkyl-chain lengths and investigated the crystal structure transformation.<sup>[185]</sup> When substituting MA with benzylamine, they obtained 2D RP type crystal structures consisting of corner-sharing  $\text{PbI}_6$  octahedral slabs. By introducing phenylalkylamines with longer alkyl chains, the MHPs show unusual crystal structures with both corner- and face-sharing  $\text{PbI}_6$  octahedral layers, leading to interesting 1D confinement effects. The enhanced confinement effect with the increasing

ligand length was also confirmed experimentally by the blueshift of PL emission peaks of the low-dimensional MHPs, suggesting the tunability of bandgap by this novel strategy.

In addition, the bandgap of low-dimensional MHP nanostructures can be tuned by controlling the size owing to the quantum confinement effect. Taking 0D MHPs as an example, when the size of perovskite NCs is reduced close to or less than their exciton Bohr radius, the continuous energy levels in the bulk material are converted to discrete states.<sup>[188]</sup> Consequently, the quantum confinement effect could affect the optical properties of perovskite QDs and NCs.<sup>[52,186]</sup> Kovalenko and co-workers reported the bandgap of  $\text{CsPbX}_3$  NCs could be successfully tuned by controlling the crystal size.<sup>[52]</sup> The light absorption edge of  $\text{CsPbX}_3$  NCs shows an obvious blueshift when the particle size decreases from 11.8 to 3.8 nm, with the corresponding bandgap tuned from 2.4 to 2.7 eV.<sup>[52]</sup> For 1D MHPs, the bandgap engineering via size control can be achieved by adjusting the diameter of NWs because of the 2D confinement effect. For instance, an obvious redshift of absorption edges was observed in  $\text{CsPbBr}_3$  NWs with increasing diameters owing to intraparticle ripening by prolonging reaction time.<sup>[187]</sup> The absorption edge of NWs with diameters increasing from 2.5 to 6.5 nm redshifts obviously from 2.95 to 2.39 eV. As for 2D nonlayered MHPs, by controlling growth parameters, the bandgap engineering is possible for 2D nanostructures with various thicknesses. Zheng et al. fabricated 2D  $\text{CsPbI}_3$  NSs with controlled square morphology by vapor-phase epitaxial growth.<sup>[188]</sup> This synthesis method involves a finely optimized balance between diffusion and reaction processes to obtain the desired morphology and thickness. They found the PL peaks of single  $\text{CsPbI}_3$  NSs exhibit a trend of redshift as their thickness increases from 3 to 60 nm, suggesting the decreased bandgap from 1.88 to 1.74 eV. In short, by controlling the chemical composition, structure, and size, bandgap engineering of low-dimensional MHPs opens the opportunity for broader applications, which is not easily achievable in inorganic semiconductors.

The above-mentioned bandgap engineering strategies by adjusting composition and dimensionality are effective, but virtually incapable of tuning the bandgap after synthesis processes. Therefore, it is of great importance to achieve bandgap engineering of MHPs by external stimuli. Low-dimensional MHPs, especially 2D ones, are often subjected to mechanical strain in synthesis, device fabrication, and flexible device applications. It is known that mechanical strain could introduce structural distortion and even phase change in MHPs, resulting in changes in their optical properties and bandgap.<sup>[189]</sup> DFT calculation performed by Som et al. shows that the bandgap of 2D  $\text{MAPbI}_3$  can be modulated linearly by applying biaxial strain, where compressive strain decreases the bandgap and tensile strain increases it.<sup>[190]</sup> Feng et al. studied the structural evolution and PL properties of 2D MHP  $(\text{BA})_2\text{PbBr}_4$  experimentally under hydrostatic compression.<sup>[191]</sup> When applying pressure, an obvious red-shift of PL peaks was observed, which may be primarily attributed to the contraction of  $\text{BA}^+$  cations and distortions of perovskite octahedra. The structural distortion induced by pressure leads to a decrease in the bandgap. Tu et al. investigated the effect of uniaxial mechanical tensile strain on the bandgap of 2D MHP flakes by bending polymer substrates to

cylinders with different radii.<sup>[192]</sup> They found the bandgap of  $(\text{BA})_2(\text{MA})_{n-1}\text{Pb}_n\text{I}_{3n+1}$  ( $n > 3$ ) increases linearly with the uniaxial mechanical tensile strain, and the MHPs with higher  $n$  values are more sensitive to applied tensile strain than those with low  $n$  values. Based on both experimental and theoretical results, they proposed the bandgap change is mainly ascribed to the deformation of inorganic octahedral slabs, with the effects of organic cations negligible. In the future, more efforts should be paid to engineer the bandgap of low-dimensional MHPs by effective external stimuli.

## 5. Low-Dimensional MHP PDs

Prominent intrinsic optical and electronic properties of MHPs are believed to achieve high-performance PDs. PDs based on polycrystalline MHP films showing high  $R$  and  $D^*$  have become a hot research topic in recent years.<sup>[104,158,193]</sup> However, polycrystalline MHP films have their disadvantages such as high bulk defects and large grain boundaries, limiting the carrier transport and the stability of devices,<sup>[194]</sup> which hinder the further improvement of PDs' performance and practical applications. Recent studies show that MHP single crystals with long carrier lifetime and high carrier mobility due to the low bulk defects and absence of grain boundaries could be another promising candidate for PDs.<sup>[195]</sup> Low-dimensional single-crystalline MHPs, possessing not only the advantages of single-crystalline perovskites but also the excellent mechanical properties for flexible devices, have attracted great attention. In this section, we survey the photodetection applications of various low-dimensional MHPs, such as 0D NCs, 1D nano- or microwires, 2D NSs or nanoplatelets, and hybrid structures.

### 5.1. PDs Based on 0D Perovskites

MHP QDs/NCs have attracted significant interest in LEDs due to their high PLQY.<sup>[196,197]</sup> There have been several studies showing the optical and electrical properties of 0D QDs/NCs are highly tunable, boosting their applications in various optoelectronic devices. Research concerning PD applications based on perovskite QDs is still rather new. Typically, 0D QD/NC films have better light-harvesting capability than planar bulk counterparts, and thus, PDs based on 0D MHPs are believed to have higher photocurrent, on/off ratio, and  $R$ . For example, Ramasamy et al. first reported PDs based on all-inorganic  $\text{CsPbX}_3$  ( $X = \text{I}, \text{Br}, \text{Cl}$ ) perovskite QDs in 2016 with a high on/off ratio of  $10^5$  and rise and decay times of 24 and 29 ms, respectively.<sup>[198]</sup> Moreover, the highly tunable bandgap of perovskite QDs exhibits the potential for photodetection in different spectra. Many groups have tried to apply 0D perovskites for photodetection in different spectral ranges from UV to NIR.<sup>[85,199–203]</sup> Among them, most of the MHP PDs mainly focus on I- or Br-based materials due to their easy preparation techniques, which limits their photodetection capacity in the shorter wavelength region due to their low bandgaps  $< 2.5$  eV. By contrast, Cl-based perovskites have wider bandgap, such as  $\text{CsPbCl}_3$  (bandgap = 2.5 eV). However, the poor film quality of spin-coated Cl-based perovskites due to the poor solubility of

$\text{CsCl}$  and  $\text{PbCl}_2$  in dimethyl sulfoxide (DMSO) would lead to high dark currents.<sup>[85]</sup> Gui et al. overcame this hurdle by using a space-confined growth method to synthesize high-quality microscale  $\text{CsPbCl}_3$  single crystals.<sup>[85]</sup> The  $\text{CsPbCl}_3$  microcrystal PDs demonstrate an  $R$  of  $0.45 \text{ A W}^{-1}$  at 5 V to near-ultraviolet (NUV) light with a high on/off ratio of  $5.6 \times 10^3$ . The dark current ( $2.23 \times 10^{-12} \text{ A}$ ) and noise current ( $\approx 10 \text{ fA } \sqrt{\text{Hz}^{-1}}$ ) are low, and the  $D^*$  is up to  $10^{11}$  Jones, which are attributed to their high crystalline quality.

Although 0D MHPs contribute to the improvement of PDs from the optical point of view, 0D MHP-based PDs still suffer from limited performance (Table 1). In terms of the electrical aspect, excitons in 0D perovskites are difficult to dissociate to free electrons and holes and be extracted due to the spatial confinement effects (i.e., high  $E_b$ ). Additionally, because the hopping transfer among neighboring NCs within 0D perovskite films is inevitable, the interfaces between NCs become barriers for smooth photocarrier transport and collection. Both two downsides make 0D MHP-based PD devices limited by suppressed  $R$ , low  $D^*$  and slow photoresponse. In early studies, 0D MHPs applied in PDs were often characterized by small-sized NCs (e.g., a few nanometers), which have high  $E_b$ , high surface trap states and are short of well-defined facets and irregularly stacked. Furthermore, charge transport in QD films may also be limited by surface ligands. The solution synthesis processes introduce capping ligands, such as ODE, OA, and OLA, which form an insulating layer on the surface of MHP NCs and are largely detrimental to the carrier transfer between NCs. For all types of PD devices, efficient carrier separation, transfer and collection are required for high performance. Only those photocarriers collected by electrodes can contribute to an electrical signal. Therefore, endeavors are urgently taken to overcome the disadvantages for achieving high-performance PDs. Here, we summarized those strategies into five types, including surface engineering, the size and morphology modification, NC networks, orientation control, and hybrid structures (Figure 4).

Surface engineering, including surface passivation<sup>[204,205]</sup> and surface ligand engineering,<sup>[205–209]</sup> is a strategy to minimize interface defects and facilitate carrier transfer among NCs. Since modifying the surface of NCs would affect the charge transfer efficiency in the films, surface passivation methods need to simultaneously consider interfacial carrier transfer as well. Wu et al. reported a surface ligand density control strategy to balance the surface passivation of QDs and the interfacial charge extraction/injection efficiency in the 0D perovskite–2D  $\text{MoS}_2$  system.<sup>[205]</sup> The 1-octane/ethyl acetate mixed solvent treatment is conducive to realize ligand density engineering, which improves the interface contact between QDs and  $\text{MoS}_2$ , and then enhances the interfacial charge carrier transfer efficiency. Poor interfacial charge transfer efficiency originating from the insulating ligands is always a serious issue for 0D MHP-based PDs. Replacing the insulating and unstable ligands outside NCs can facilitate the carrier transfer. Gong et al.<sup>[208]</sup> reported a method of passivating  $\text{CsPbCl}_3$  NC surface with 3-mercaptopropionic acid (MPA) ligand exchange. MPA has a shorter thiol ligand than the original organic ligands (OA and OLA) and can be more strongly capped on  $\text{CsPbCl}_3$  NCs, offering a highly efficient carrier-transfer avenue between NCs and from  $\text{CsPbCl}_3$  NCs to acceptors, such as graphene (Figure 4a). After

**Table 1.** Key figures of merit of typical PDs based on low-dimensional MHPs.

Device types	Materials	Perovskite morphology	$R$ [ $A W^{-1}$ ]	$D^*$ [Jones]	EQE [%]	On/off ratio	Gain	LDR [dB]	$\tau_{rise}/\tau_{decay}$ [ms]	Refs.
Photoconductor	CsPbBr <sub>3</sub>	QDs	24.5	$8.9 \times 10^{13}$		$1 \times 10^5$			4700/2300	[209]
Photoconductor	CsPbBr <sub>3</sub>	Microparticles	0.18	$6.1 \times 10^{10}$					1.8/1.0	[216]
Photoconductor	CsPbBr <sub>3</sub>	Microcrystals	$6 \times 10^4$	$1 \times 10^{13}$	$2 \times 10^7$		$1 \times 10^5$	100	0.5/1.6	[159]
Photoconductor	CsPbBr <sub>3</sub>	Microcrystals	0.172	$4.8 \times 10^{12}$		$1.3 \times 10^5$		113	0.14/0.12	[317]
Phototransistor	CsPbBr <sub>3</sub> /graphene	NCs	$2 \times 10^4$	$8.6 \times 10^{10}$					3100/24200	[318]
Photoconductor	CsPbBr <sub>3</sub> /NaYF <sub>4</sub> :Yb,Er nanoparticles	QDs	1.5			$1 \times 10^4$			5.0/5	[285]
Photoconductor	CsPbBr <sub>3</sub> /SnO <sub>2</sub> microwire	Microcrystals	1.9	$1 \times 10^{13}$					0.03/1.94	[302]
Photoconductor	CsPbBr <sub>3</sub> /TiO <sub>2</sub>	NCs	0.01	$4.56 \times 10^8$		$1 \times 10^6$			0.2/1.2	[217]
Phototransistor	CsPbBr <sub>3-x</sub> I <sub>x</sub> /graphene	NCs	$8.2 \times 10^8$	$2.4 \times 10^{16}$					810/3650	[276]
Phototransistor	CsPbBr <sub>3-x</sub> I <sub>x</sub> /MoS <sub>2</sub>	QDs	$7.7 \times 10^4$	$5.6 \times 10^{11}$	$1 \times 10^7$	$1 \times 10^4$			590/320	[282]
Phototransistor	CsPbBr <sub>3-x</sub> I <sub>x</sub> /MoS <sub>3</sub>	QDs	$1.13 \times 10^5$	$6.37 \times 10^{11}$					420/190	[205]
Photodiode	CsPbBrCl <sub>2</sub> /Si NWs	QDs	0.054						0.48/1.03	[286]
Phototransistor	CsPbCl <sub>3</sub> /graphene	NCs	$1 \times 10^6$	$2 \times 10^{13}$					300/350	[208]
Phototransistor	CsPbI <sub>3</sub>	NCs				$1 \times 10^5$			24/29	[198]
Photoconductor	CsPbI <sub>3</sub>	1D QD arrays	0.06		14				4.4/6.7	[219]
Photodiode	GaN/CsPbBr <sub>3</sub> /ZnO	Microcrystals	0.09	$1.03 \times 10^{14}$		$1 \times 10^5$			0.1/0.14	[319]
Phototransistor	MAPbBr <sub>3</sub> /graphene	Microislands	$6 \times 10^5$				$1 \times 10^9$		120/750	[199]
Phototransistor	MAPbI <sub>3</sub>	Microislands				$>10^4$			$<40/<50$	[320]
Photoconductor	MAPbI <sub>3</sub>	Microcrystals	275	$1 \times 10^{13}$	$1 \times 10^4$		409		0.03/0.02	[201]
Phototransistor	MAPbI <sub>3</sub> /graphene/Au nanoparticles	Nanoislands	$2.1 \times 10^3$						1500	[321]
Photoconductor	Cs <sub>3</sub> Sb <sub>2</sub> Cl <sub>9</sub>	Nanorods	$3.62 \times 10^3$	$1.25 \times 10^6$					130/230	[322]
Photoconductor	CsPb(Br/I) <sub>3</sub>	Nanorods				$2 \times 10^3$			680/660	[323]
Photoconductor	CsPbBr <sub>3</sub>	Single NW	$4.4 \times 10^3$				$1.3 \times 10^4$		0.252/0.3	[235]
Photodiode	CsPbBr <sub>3</sub>	NWs	0.3	$1 \times 10^{13}$		$1 \times 10^6$		135	0.4/0.43	[225]
Photoconductor	CsPbBr <sub>3</sub>	NWs				$1 \times 10^3$				[324]
Photoconductor	CsPbBr <sub>3</sub>	NWs				$1.1 \times 10^3$			82/54	[226]
Photoconductor	CsPbCl <sub>3</sub>	NWs				$5.8 \times 10^3$			70/45	[226]
Photoconductor	CsPbBr <sub>3</sub>	NW Network				$1 \times 10^3$			100	[87]
Photoconductor	CsPbBr <sub>3</sub>	NW arrays	$1.38 \times 10^3$			$1 \times 10^3$			0.0215/0.0234	[234]
Photoconductor	CsPbBr <sub>3</sub>	Microwires	118	$1 \times 10^{12}$	$1 \times 10^4$	100			38/36	[236]
Photoconductor	CsPbCl <sub>3</sub>	Microwire network	0.014			$2 \times 10^3$			3.212/2.511	[325]
Photoconductor	CsPbI <sub>3</sub>	Single NW				100				[326]
Photoconductor	CsPbI <sub>3</sub>	Single NW	$4.49 \times 10^3$	$7.9 \times 10^{12}$		$10^4$ – $10^5$	1564		$<50/<50$	[327]
Photoconductor	CsPbI <sub>3</sub>	Single NW	$2.92 \times 10^3$	$5.17 \times 10^{13}$	$9 \times 10^5$	$3.13 \times 10^3$			0.05/0.15	[237]
Photoconductor	CsPbI <sub>3</sub>	NWs	$6.7 \times 10^{-3}$	$1.57 \times 10^8$					292/234	[90]
Photoconductor	CsPbI <sub>3</sub>	NWs	$1.29 \times 10^3$	$2.6 \times 10^{14}$					0.85/0.78	[294]
Photoconductor	CsPbI <sub>3</sub>	Nanotube	$1.84 \times 10^3$	$9.99 \times 10^{13}$	$5.65 \times 10^5$	$2.36 \times 10^3$			3.78/3.59	[64]
Photoconductor	CsPbI <sub>3</sub>	NW arrays	0.35	$1.64 \times 10^{10}$						[328]
Photoconductor	CsSnI <sub>3</sub>	NW arrays	0.054	$3.85 \times 10^5$		$1 \times 10^3$			83.3/243.4	[93]
Photodiode	CsPbI <sub>3</sub> /CsPbBr <sub>3</sub>	NW arrays	0.125						0.7/0.8	[329]
Photoconductor	MAPbBr <sub>3</sub>	Porous NW				61.9			120/86	[223]
Photoconductor	MAPbBr <sub>3</sub>	Microwire arrays	$3.16 \times 10^3$			$1.08 \times 10^3$				[172]
Photoconductor	MAPbBr <sub>3</sub> /NaYF <sub>4</sub> :Yb,Er nanoparticles	Microwire arrays	0.27	$7.6 \times 10^{11}$	48	$2 \times 10^3$			52/67	[200]
Photoconductor	MAPbI <sub>3</sub>	NWs	$6 \times 10^6$						2000/5000	[330]

**Table 1.** Continued.

Device types	Materials	Perovskite morphology	$R$ [ $A W^{-1}$ ]	$D^*$ [Jones]	EQE [%]	On/off ratio	Gain	LDR [dB]	$\tau_{rise}/\tau_{decay}$ [ms]	Refs.
Photoconductor	MAPbI <sub>3</sub>	NWs				13			120/210	[228]
Photoconductor	MAPbI <sub>3</sub>	NWs	1.32	$2.5 \times 10^{12}$					0.2/0.3	[331]
Phototransistor	MAPbI <sub>3</sub>	NWs	$5 \times 10^{-3}$						0.35/0.25	[65]
Photoconductor	MAPbI <sub>3</sub>	NW Network	0.23	$7 \times 10^{11}$					53.2/50.2	[332]
Photoconductor	MAPbI <sub>3</sub>	NW Network	0.1	$1.02 \times 10^{12}$		340			0.3/0.4	[33]
Photoconductor	MAPbI <sub>3</sub>	NW arrays	$1.25 \times 10^4$	$1.73 \times 10^{11}$				150	0.00034/0.00042	[155]
Photoconductor	MAPbI <sub>3</sub>	NW arrays	4.95	$2 \times 10^{13}$					<0.1	[36]
Photoconductor	MAPbI <sub>3</sub>	Nanonets	10.33		$1.83 \times 10^3$	$2 \times 10^3$			0.02/0.01	[333]
Photoconductor	MAPbI <sub>3</sub>	Microwires	13.8	$2.55 \times 10^{12}$		$2 \times 10^4$			50/50	[239]
Photoconductor	MAPbI <sub>3</sub>	Microwires	13.57	$5.25 \times 10^{12}$				114	0.08/0.24	[32]
Phototransistor	MAPbI <sub>3</sub> /graphene	NWs	$2.6 \times 10^6$						55 000/75 000	[277]
Photoconductor	MAPbI <sub>3-x</sub> (SCN) <sub>x</sub>	NW Network	0.62	$7.3 \times 10^{12}$					0.227/0.216	[227]
Photoconductor	MASnI <sub>3</sub>	NWs	0.47	$8.80 \times 10^{10}$					1500/400	[230]
Photoconductor	CsPbBr <sub>3</sub>	NSs	0.64		54	> $10^4$			0.019/0.024	[241]
Phototransistor	CsPbBr <sub>3</sub>	NSs				100			17.8/15.2	[240]
Photoconductor	CsPbBr <sub>3</sub>	Nanoplates	34	$7.5 \times 10^{12}$		$1 \times 10^3$			0.6/0.9	[212]
Photoconductor	CsPbBr <sub>3</sub>	Micro/Nanoflakes	2.776		$1.25 \times 10^3$	100			40/20	[72]
Photoconductor	CsPbBr <sub>3</sub>	Microplatelets	1.33	$8.6 \times 10^{11}$		$4.6 \times 10^3$			20.9/24.6	[211]
Photoconductor	CsPbBr <sub>3</sub> /Carbon nanodots	NSs	0.61			217			1.51/1.77	[280]
Photoconductor	CsPbBr <sub>3</sub> /Carbon nanodots	NSs	0.608			102			1.55/1.77	[280]
Photoconductor	CsPbBr <sub>3</sub> /CNT	NSs	31.1		$7.49 \times 10^3$				0.016/0.38	[35]
Photoconductor	CsPbBr <sub>3</sub> /MoS <sub>2</sub>	NSs	4.4	$2.5 \times 10^{10}$	302	$1 \times 10^4$			0.72/1.01	[143]
Photoconductor	CsPbBr <sub>3</sub> /PCBM	NSs	10.85	$3.06 \times 10^{13}$		$1 \times 10^5$		73	0.044/0.39	[272]
Photoconductor	CsPbCl <sub>3</sub>	Single microplatelet	0.45	$1 \times 10^{11}$		$5.6 \times 10^3$			8.0/7	[85]
Phototransistor	graphene/MAPbI <sub>3</sub> /WSe <sub>2</sub> /graphene	Nanoflakes	950			$1 \times 10^6$	2200		22/37	[334]
Photoconductor	MAPbI <sub>3</sub>	NSs	0.036						320/330	[335]
Phototransistor	MAPbI <sub>3</sub>	NSs	22/12			100			20/40	[95]
Photoconductor	MAPbI <sub>3</sub>	Nanoflakes	12	$1 \times 10^{11}$	$5.89 \times 10^3$	$1 \times 10^4$			2.2/4	[336]
Phototransistor	MAPbI <sub>3</sub>	Microplate array	7						0.5/0.5	[96]
Photoconductor	(iBA) <sub>2</sub> ((MA) <sub>0.40</sub> (FA) <sub>0.60</sub> ) <sub>0.90</sub> Cs <sub>0.1</sub> <sub>0</sub> ) <sub>3</sub> Pb <sub>4</sub> I <sub>13</sub>	2D layered film	0.4	$1.68 \times 10^{12}$		720			43/22	[244]
Photoconductor	(iBA) <sub>2</sub> (MA) <sub>n-1</sub> Pb <sub>n</sub> I <sub>3n+1</sub>	2D layered film	0.12			400			16/15	[164]
Phototransistor	(BA) <sub>2</sub> (MA) <sub>n-1</sub> Pb <sub>n</sub> I <sub>3n+1</sub> /MoS <sub>2</sub>	2D layered flake	$1 \times 10^4$	$4 \times 10^{10}$					10.0/10	[284]
Photoconductor	(BA) <sub>2</sub> (MA)Pb <sub>2</sub> I <sub>7</sub>	2D layered crystal		$1 \times 10^{11}$	200	$1 \times 10^3$				[37]
Photoconductor	(C <sub>4</sub> H <sub>9</sub> NH <sub>3</sub> ) <sub>2</sub> (MA) <sub>2</sub> Pb <sub>3</sub> Br <sub>10</sub>	2D layered crystal		$3.6 \times 10^{10}$		$2.5 \times 10^3$			0.15/0.57	[337]
Phototransistor	(C <sub>4</sub> H <sub>9</sub> NH <sub>3</sub> ) <sub>2</sub> PbBr <sub>4</sub> /graphene	2D layered crystal	$2.1 \times 10^3$			$1 \times 10^3$				[101]
Photoconductor	(C <sub>5</sub> H <sub>11</sub> NH <sub>3</sub> ) <sub>2</sub> (MA)Pb <sub>2</sub> I <sub>7</sub>	2D layered crystal	$3.87 \times 10^{-3}$	$2.92 \times 10^{10}$		$1 \times 10^3$			0.0015/0.0017	[34]
Photoconductor	(PEA) <sub>2</sub> PbI <sub>4</sub>	2D layered crystal	$5 \times 10^{-3}$	$1.07 \times 10^{13}$		10.8				[316]
Photoconductor	(OA) <sub>2</sub> FA <sub>n-1</sub> Pb <sub>n</sub> Br <sub>3n+1</sub>	2D layered microplatelets	32			$7.1 \times 10^3$			0.25/1.45	[257]
Photoconductor	(PEA) <sub>2</sub> PbI <sub>4</sub>	2D layered crystal	139.6	$1.89 \times 10^{15}$	$3.77 \times 10^4$				0.021/0.037	[255]
Photoconductor	(R)- $\alpha$ (PEA) <sub>2</sub> PbI <sub>4</sub>	2D layered crystal	0.6	$3.06 \times 10^{11}$	140	124			22/34	[38]
Photoconductor	Cs <sub>3</sub> Bi <sub>2</sub> I <sub>9</sub>	2D layered crystal	0.033	$1 \times 10^{10}$	9.2	40			10.2/37.2	[338]
Photoconductor	(C <sub>4</sub> H <sub>9</sub> NH <sub>3</sub> ) <sub>n</sub> (MA) <sub>n-1</sub> Pb <sub>n</sub> I <sub>3n+1</sub>	2D layered crystal		$10^{11}$ – $10^{12}$		$1 \times 10^4$			0.002/0.004	[243]
Phototransistor	graphene/(PEA) <sub>2</sub> SnI <sub>4</sub> /MoS <sub>2</sub>	2D layered flake	$1.1 \times 10^3$	$8.09 \times 10^9$	38.2	500			34/38.2	[279]
Photoconductor	(C <sub>6</sub> H <sub>5</sub> (CH <sub>2</sub> ) <sub>3</sub> NH <sub>3</sub> ) <sub>3</sub> Pb <sub>2</sub> I <sub>7</sub>	2D layered flake		$1.2 \times 10^{10}$					0.85/0.78	[339]
Photoconductor	(BA) <sub>2</sub> (MA) <sub>n-1</sub> Pb <sub>n</sub> I <sub>3n+1</sub>	2D layered NW array	$1.5 \times 10^4$	$7 \times 10^{15}$					0.028/0.025	[31]



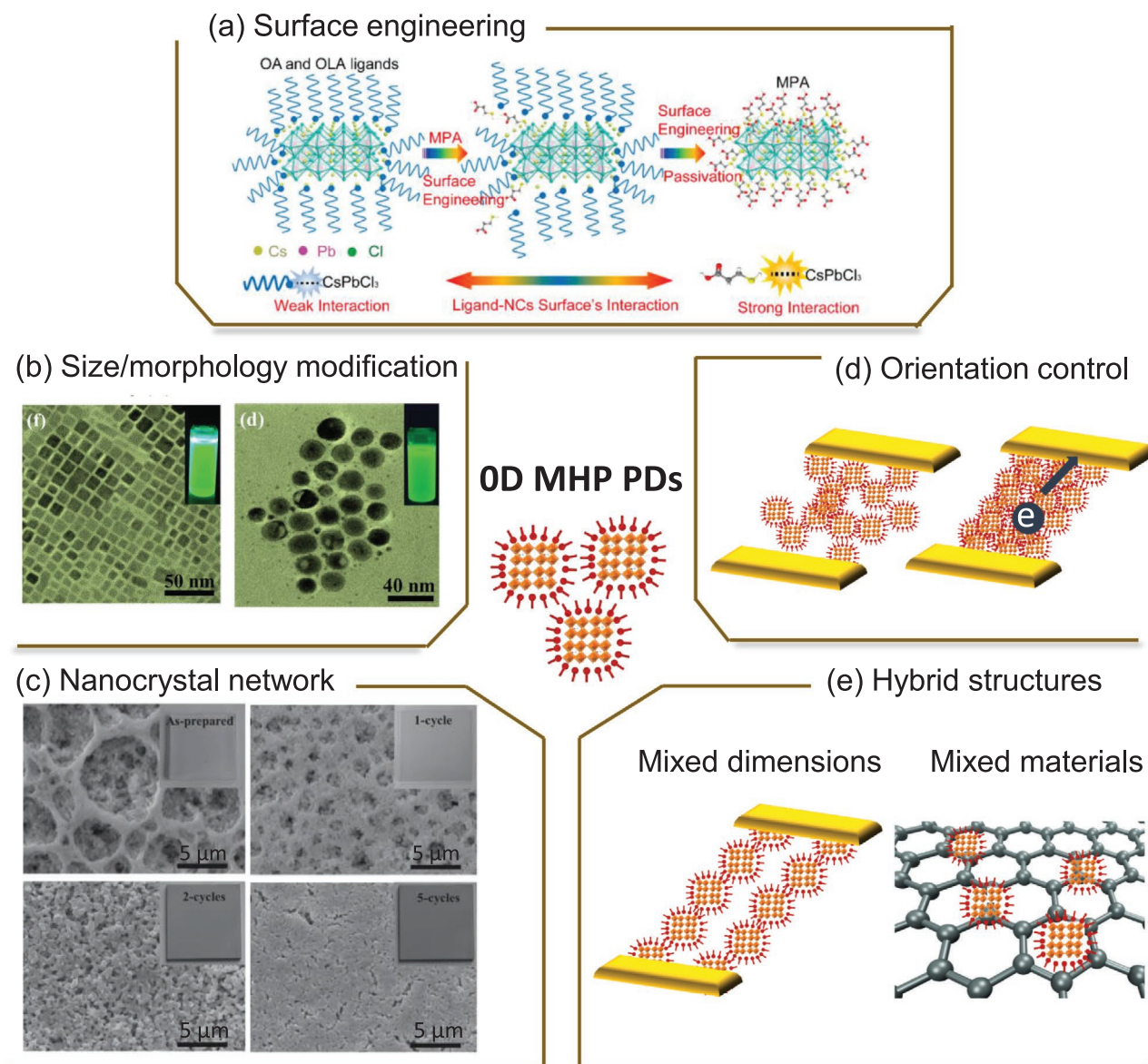


**Figure 4.** Strategies to improve 0D MHP PDs. a) Schematics of the surface engineering process by replacing weak-interaction OA, OLA, and ODE ligands with strong-interaction MPA ligands on CsPbCl<sub>3</sub> NCs. Reproduced with permission.<sup>[208]</sup> Copyright 2019, American Chemical Society. b) TEM images of different shapes of CsPbBr<sub>3</sub> NCs. c) SEM images of the pristine CsPbBr<sub>3</sub> NC thin film, and the films treated with 1, 2, and 5 times of film modification. All the scale bars are 5 μm and the insets are graphs of corresponding samples. b,c) Reproduced with permission.<sup>[216]</sup> Copyright 2016, Wiley-VCH. d) Schematics of NC films before and after centrifugal casting treatment. e) Examples of 0D MHP-based hybrid structures.

the MPA exchange, the radiative electron–hole recombination is completely quenched according to PL emission spectra, and the photoresponse time decreases from 191.8 to 0.3 s. The treated devices exhibit a high  $R$  exceeding  $10^6$  A W<sup>-1</sup>, a high  $D^*$  of  $2 \times 10^{13}$  Jones, and less than 10% degradation of the photocurrent under ambient conditions after 2400 h.

Size/morphology modification of single NCs could tune the  $E_b$  and decrease the surface defects originating from NCs or microcrystals in nature.<sup>[159,201,210–212]</sup> Larger 0D perovskites such as microcrystals provide lower  $E_b$  and surface  $n_{traps}$ , leading to longer carrier lifetime and higher electron diffusion coefficient. These properties are believed to improve the  $D^*$  and response speed of PDs. Zhang et al.<sup>[210]</sup> synthesized FAPbBr<sub>3</sub>

microcrystals (few tens of micrometers in size) with a low  $n_{trap}$  of  $6.98 \times 10^{11}$  cm<sup>-3</sup>. Compared with microcrystal layers, perovskite NC absorber layers or polycrystalline films have relatively high  $n_{trap}$  ( $>10^{14}$  cm<sup>-3</sup>) and low mobility ( $<10$  cm<sup>2</sup> V<sup>-1</sup> s<sup>-1</sup>), which therefore hinder their photodetection performance.<sup>[213–215]</sup> Yang et al.<sup>[159]</sup> fabricated CsPbBr<sub>3</sub> microcrystal layers (few tens of micrometers in size) by using a solution growth method, exhibiting a low  $n_{trap}$  of  $10^{12}$  cm<sup>-3</sup> and high carrier mobility over 100 cm<sup>2</sup> V<sup>-1</sup> s<sup>-1</sup>. Taking the advantage of efficient charge transfer in the perovskite layers based on microcrystals, the CsPbBr<sub>3</sub> microcrystal PDs show an ultrahigh  $R$  of  $6 \times 10^4$  A W<sup>-1</sup>, a gain of  $10^5$ ,  $D^*$  value of  $>10^{13}$ , and the fast response time of  $\approx 1$  ms, which defeat most of the previous perovskite PDs.<sup>[159]</sup>

In addition to modulating individual NCs, strategies for modifying NC absorber layers to improve PD performance have been demonstrated. An as-deposited NC layer possesses a high density of voids within the film as well as high surface roughness, limiting the carrier hopping transfer. Constructing compact NC layers, NC networks, and NC arrays has been proposed to solve this problem.<sup>[216–220]</sup> Zeng's group fabricated compact and smooth-surfaced CsPbBr<sub>3</sub> film via recyclable dissolution-recrystallization method, which can build smooth carrier channels like a network.<sup>[216]</sup> The 0D MHP network reduces the quantum confinement effect and improves interfacial charge-carrier transport, which boosts the separation and extraction of electrons and holes. By controlling the solubility equilibrium of the solution containing perovskite crystals, polar solvents, and surfactants, the NC network film becomes denser with only a small number of holes, and thus, PD based on treated CsPbBr<sub>3</sub> NC films exhibits improved *R*, EQE, response speed, and stability (Figure 4c). The same group demonstrated the PDs constructed from CsPbBr<sub>3</sub> NC arrays with a preferred orientation by centrifugal casting (Figure 4d).<sup>[217]</sup> Combining with the localized surface plasmonic effect of Au NCs, the photocurrent rises from 245.6 to 831.1 μA and the on/off ratio reaches 10<sup>6</sup>.

Overall, PDs based on 0D MHP layers possess superior light-harvesting ability but poor carrier collection. Although several strategies have been proposed to address the poor charge separation and interfacial carrier transport of 0D MHP layers, the improvement is still limited. One alternative powerful approach to improve the performance of 0D MHP film-based PDs is to integrate perovskites with other dimensional perovskite or functional materials (Figure 4e), which will be discussed in Section 5.4.

## 5.2. PDs Based on 1D Perovskites

1D MHPs offer additional advantages over their 0D counterparts. Compared with 0D MHPs, single-crystalline NWs with well-defined structures provide more direct charge transport pathways. Photogenerated carriers would be constrained and smoothly flow within the 1D single-crystalline conductive channels. Much fewer barriers for carrier collection by the electrodes result in larger carrier mobilities and longer carrier diffusion lengths than those of 0D and polycrystalline perovskite films.<sup>[32,221,222]</sup> Horváth et al.<sup>[65]</sup> first synthesized 1D form of MHPs and then integrated them into PDs (Figure 5a,b). MAPbI<sub>3</sub> NWs with mean diameters of 50 and 400 nm and length up to 10 μm are obtained by a simple slip-coating approach, however, the corresponding PD shows a low *R* of 5 mA W<sup>-1</sup>. Sequentially, many groups reported 1D MHP PDs, but no promising results have been presented.<sup>[223–227]</sup> The poor performance might be attributed to a lack of precise control of the 1D NW distributions and dimensions. Not all NWs provide direct carrier pathways to the electrodes (Figure 5a–c). Random distributions and morphologies of NWs are detrimental to the collection of photocarriers by electrodes and remain an obstacle to their potential for integrated optoelectronic applications. Therefore, strategies for synthesizing controllable NWs are essential for optoelectronic devices.

A well-connected NW network serves as a straightforward platform to address the problem of carrier transport (Figure 5d).<sup>[33,87,228]</sup> Deng et al.<sup>[33]</sup> synthesized uniform and transparent MAPbI<sub>3</sub> networks as PD arrays by controlling the crystallization. The stronger X-ray diffraction (XRD) peak of MHP networks at (110) plane located at 14.2° than that of polycrystalline films and NWs indicates the preferential orientation growth of perovskite networks (Figure 5d1). Moreover, the photocurrent ranges of thin film and network-based PDs are much narrower than those of random NW-based PDs, which reveals the significant improvement of the uniformity of network structures (Figure 5d2). The on/off ratio and *D*\* of PD arrays reach 300 and 1.02 × 10<sup>12</sup> Jones, respectively. Afterward, a vapor-phase epitaxial growth method is proposed to synthesize horizontal single-crystalline CsPbX<sub>3</sub> (X = Cl, Br, I) NW networks with controlled crystallographic orientations on the (001) plane of muscovite and phlogopite mica (Figure 2d,e).<sup>[87,91,93]</sup> The density of interconnected epitaxial networks can be controlled by the growth time, and the on/off ratio of CsPbBr<sub>3</sub> NW network PDs is calculated to be >10<sup>3</sup>.<sup>[87]</sup>

Preparing aligned NW arrays is an even better choice to study the optical and electrical properties of 1D MHPs and to improve the reproducibility of optoelectronic devices.<sup>[229]</sup> Perovskites with different compositions tend to form different morphologies. For instance, cubic MAPbCl<sub>3</sub> and cubic MAPbBr<sub>3</sub> usually exhibit cube and plate morphologies, while tetragonal MAPbI<sub>3</sub> tends to crystallize along one dimension. Therefore, developing strategies to control the morphology of MHPs with different compounds or compositions is necessary for systematic studies.<sup>[32,90,155,230]</sup> Gao et al.<sup>[172]</sup> developed a method with controlled dewetting for patterning 1D single-crystalline perovskite arrays with diverse halide stoichiometry. Jie's group developed single-crystalline aligned MAPbI<sub>3</sub> microwire arrays by using a blade coating method (Figure 1f), which is applicable for processing highly uniform microwire arrays with large area onto flexible substrates.<sup>[32]</sup> With the blade gradually receding, MAPbI<sub>3</sub> nuclei will self-organize and grow preferentially to form aligned 1D structures. The microwire array-based PDs exhibit an *R* of 13.57 A W<sup>-1</sup> and a *D*\* of 5.25 × 10<sup>12</sup> Jones. The same group then reported a fluid-guided antisolvent vapor-assisted crystallization method to synthesize high quality aligned MAPb(I<sub>1-x</sub>Br<sub>x</sub>)<sub>3</sub> NW arrays.<sup>[155]</sup> The corresponding PDs exhibit a remarkable performance with a high *R* of 12 500 A W<sup>-1</sup> and an LDR of 115 dB, which are among the best values for pure MAPbI<sub>3</sub>-based PDs (*R* = 320 A W<sup>-1</sup> for PDs based on polycrystalline thin-film MAPbI<sub>3</sub>;<sup>[158]</sup> *R* = 953 A W<sup>-1</sup> for PDs based on MAPbI<sub>3</sub> single crystals<sup>[195]</sup>). The high performance is attributed to the high-quality single-crystalline and smooth NW arrays obtained by the slow crystallization process. As for all-inorganic MHPs, CsPbX<sub>3</sub> has triggered enormous attention owing to its high ambient stability, however, stabilizing the cubic phase of CsPbI<sub>3</sub> under RT is still challenging. Generally, most groups synthesize CsPbI<sub>3</sub> QDs to stabilize their cubic phase. Fan's group reported the method of growing perovskite NWs inside AAO templates, which consist of organized hexagonal pore arrays.<sup>[90,230]</sup> The CsPbI<sub>3</sub> NW arrays are identified to be in a stable cubic phase at RT due to the effective confinement of NWs by AAO. Furthermore, the same group built an artificial eye by using a curved perovskite NW PD arrays as

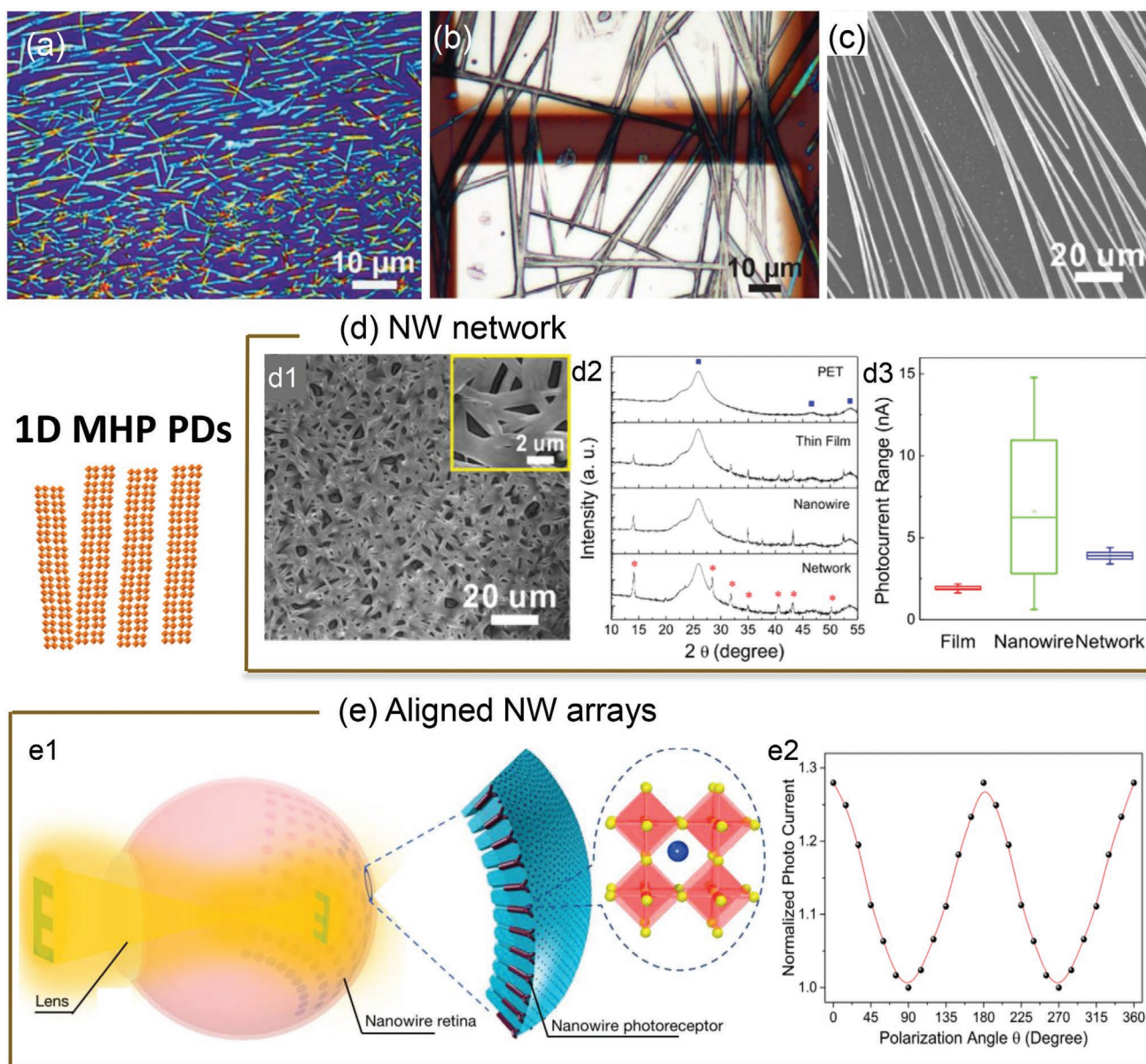


**Figure 5.** Optical microscopy image of a) the MAPbI<sub>3</sub> NWs and b) NWs crossing the Pt source–drain contacts. a,b) Reproduced with permission.<sup>[65]</sup> Copyright 2014, American Chemical Society. c,d1) SEM images of MAPbI<sub>3</sub> NWs and networks synthesized by controlling the crystallization. d2) XRD patterns of MAPbI<sub>3</sub> thin film, NWs, and networks deposited on PET. The peaks of OTP and PET substrates are marked as red and blue marks, respectively. d3) Photocurrent statistical boxplots of PD arrays made by MAPbI<sub>3</sub> thin film, NWs, and networks. c,d1–d3) Reproduced with permission.<sup>[33]</sup> Copyright 2015, American Chemical Society. e1) Schematic of working mechanism of a biomimetic eye with a hemispherical MHP NW array retina. Reproduced with permission.<sup>[231]</sup> Copyright 2020, Springer Nature. e2) Normalized photocurrent of a MAPbI<sub>3</sub> NW-based PD as a function of the polarization angle  $\theta$ , the unity corresponds to the photocurrent when  $\theta = 90^\circ$  or  $270^\circ$ . Reproduced with permission.<sup>[36]</sup> Copyright 2016, American Chemical Society.

hemispherical retina, which will discuss more details in Section 7.3 (Figure 5e1).<sup>[231]</sup>

By taking the advantage of the anisotropic geometry, aligned 1D MHPs can serve as polarization-sensitive PDs because of their anisotropic optical absorption, and that could be useful in applications including integrated photonic circuits, optical switches, near-field imaging, and high-resolution detection.<sup>[232,233]</sup> Gao et al.<sup>[36]</sup> first presented obvious polarization-dependent light absorption of 1D MAPbI<sub>3</sub> NW arrays made by a one-step self-assembly method. The peak-to-valley ratio of the

photocurrent of 1.3 shows the strong polarization-dependent photodetection (Figure 5e2). The maximum photocurrent emerges where the light is polarized parallel to the NW orientation axis, while the minimum photocurrent emerges when the light is polarized perpendicular to the axis. In a similar manner, Feng et al.<sup>[234]</sup> demonstrated the highly polarization-sensitive character of PDs based on CsPbBr<sub>3</sub> NW arrays made through the asymmetric-wettability system. The normalized absorption intensity and photocurrent show a polarization ratio of  $\approx 2.8:1$  and  $2.6:1$  with the polarization parallel and perpendicular to the

orientation axis of NWs, respectively. Owing to the high-crystallinity and crystallographic-ordering features of 1D single-crystalline NW arrays, a high-performance PD with the  $R$  exceeding  $1000 \text{ A W}^{-1}$  and fast response speed (21.5 and  $23.4 \mu\text{s}$  for the rise and decay time) has been achieved.

Single 1D perovskite NW-based PD is another approach to reach high performance.<sup>[235–237]</sup> Shoaib et al.<sup>[235]</sup> grew ultralong single-crystalline CsPbBr<sub>3</sub> NWs with smooth surfaces and a well-defined cross-section (with a diameter of several hundred nanometers) by a controlled vapor growth approach. PDs based on the CsPbBr<sub>3</sub> NWs show a high  $R$  of  $4400 \text{ A W}^{-1}$  and a response speed of  $252 \mu\text{s}$ . Yang et al.<sup>[237]</sup> grew CsPbI<sub>3</sub> NWs with a uniform diameter of 150 nm and a length of  $2 \mu\text{m}$  via a facile solution process. The as-constructed PD based on a single CsPbI<sub>3</sub> NW exhibits an  $R$  of  $2920 \text{ A W}^{-1}$ , a response time of  $50 \mu\text{s}$ , and a  $D^*$  of  $5.17 \times 10^{13}$  Jones. Gui et al.<sup>[236]</sup> reported a polycrystalline single CsPbBr<sub>3</sub> microwire PD, showing an  $R$  of  $118 \text{ A W}^{-1}$  and a  $D^*$  of  $>10^{12}$  Jones. In addition, all-inorganic lead-free CsCu<sub>2</sub>I<sub>3</sub> single crystals with 1D crystal structure were prepared by Li et al.<sup>[238]</sup> Under illumination, [CuI<sub>4</sub>] tetrahedra chains provide fast 1D transport pathway in which photo-generated carriers are localized, leading to anisotropic carrier transport properties and good photodetection performance.

Despite the reduced grain boundary and interfaces of 1D single-crystalline MHPs for efficient photocarrier transport, as the same as 0D structures, the concomitant disadvantage associated with optoelectronic devices employing 1D perovskites is their large surface area, which leads to the high density of electronic surface trap states. Moreover, the dangling bonds can act as reacting sites for material decomposition when subject to moisture or light exposure, and thus significantly decrease the device stability. Many groups proposed perovskite microwires or passivation methods, lowering the surface trap states to improve the device performance and stability.<sup>[32,36,172,236,239]</sup> Unlike 0D structures, the passivation layers on the surfaces of 1D MHPs could be an insulating layer because the photocarriers transport within 1D single crystals without hopping transfer. Thus, the device performance and stability based on 1D perovskites could be improved by introducing surface passivating ligands. For example, by introducing OA soaking treatment to passivate surface defects of MAPbI<sub>3</sub> NWs, the corresponding PDs exhibited twice the photocurrent, half the dark current, a high  $D^*$  of  $2 \times 10^{13}$  Jones, and much improved stability.<sup>[36]</sup>

Typically, PDs based on 1D MHPs have shown satisfactory performance, such as high  $R$ . However, the high surface defects of these nanostructured MHPs might still dominate the electrical properties and stability of optoelectronic devices, which seriously hinder their practical applications.

### 5.3. PDs Based on 2D Perovskites

We divided the studies of 2D MHP-based PDs into two aspects. One is 2D nonlayered MHPs directly thinned down from 3D MHP structures into nanometer scale or atomically thin films, and the other is 2D layered MHPs. The former is similar to 0D and 1D nanostructures but with in-plane anisotropic planar geometry, which is expected to have the stronger light absorption and faster in-plane charge carrier transport

arising from the reduced hopping barriers. Wang et al.<sup>[96]</sup> first reported the patterned growth of nonlayered MHP microplate arrays with the size of  $\approx 10 \mu\text{m}$ , and the thickness of 300–500 nm by combining solution process and vapor-phase conversion method. The  $R$  of MAPbI<sub>3</sub> microplate PD arrays is calculated to be  $\approx 7 \text{ A W}^{-1}$  with a fast response speed of  $500 \mu\text{s}$ . For the fundamental understanding of the photodetection ability of ultrathin 2D MHPs, Liu et al.<sup>[95]</sup> first synthesized 2D MAPbI<sub>3</sub> NSs as thin as a single unit cell ( $\approx 1.3 \text{ nm}$ ) by the same method. **Figure 6a–c** shows the MAPbI<sub>3</sub> NSs with different layers. The PL emission shifts from 760 to 720 nm (i.e., bandgap shifts from 1.63 to 1.72 eV) when the MAPbI<sub>3</sub> bulk crystals thin down to a single layer, yielding a tunable photodetection (**Figure 6d**). The  $R$  of the single layered MAPbI<sub>3</sub> NS phototransistor at 1 V bias is calculated to be  $22 \text{ A W}^{-1}$  under a 405 nm laser and  $12 \text{ A W}^{-1}$  under 532 nm, respectively, and the on/off ratio reaches up to 2 orders of magnitude. The high performance can be attributed to the strong light–matter interaction and broadband light-harvesting capability in MHP NSs. Solution-based colloidal synthesis is proposed to fabricate all-inorganic CsPbX<sub>3</sub> NS assembled films to improve both the performance and stability.<sup>[240,241]</sup> Besides, these NSs are suitable to make large-area, crack-free, high-quality films for flexible and ultrathin optoelectronic devices. **Figure 6e,f** shows flexible PDs based on CsPbBr<sub>3</sub> NSs with a thickness of  $\approx 3.3 \text{ nm}$  and an edge length of  $\approx 1 \mu\text{m}$ . The ultrafast response time of the PD (19 and  $25 \mu\text{s}$  for the rise and decay time, respectively) is attributed to the high crystal quality and efficient carrier transport. It is noted that these flexible PDs with good photodetection performance are made by simple and cost-effective ink-printing process.

As discussed above, 2D layered perovskites are built by layered structures of perovskite slabs separated by long-chain organic cations. The presence of hydrophobic organic chain spacers would prevent [MX<sub>6</sub>]<sup>4-</sup> octahedral sheets from directly contacting with moisture in ambient conditions, thus leading to greater environmental stability compared to that of 3D or other nanostructures. This is also the reason that among various types of MHP structures (including 0D single-crystalline NCs/microcrystals, 1D single-crystalline NWs/microwires, 2D single-crystalline NSs, 3D polycrystalline films), the 2D layered structure is particularly interesting for practical optoelectronic devices. Since the optical and electrical properties can be tuned by changing either the layer number ( $n$ ) or chemical composition, PDs based on 2D layered MHPs with different  $n$  were studied.<sup>[11,126,164,242,243]</sup> Zhou et al.<sup>[242]</sup> reported the synthesis and investigation of 2D layered MHP (C<sub>4</sub>H<sub>9</sub>NH<sub>3</sub>)<sub>2</sub>(CH<sub>3</sub>NH<sub>3</sub>) <sub>$n-1$</sub> Pb <sub>$n$</sub> I <sub>$3n+1$</sub>  ( $n = 1, 2, 3$ ) (**Figure 7a**). They found PDs based on the layered MHP show the layer number-dependent photoresponse with short response time in milliseconds. The PD based on the three-layered perovskite has better performance than that of the PD based on single-layered perovskite, in terms of the photocurrent,  $I_{\text{light}}/I_{\text{dark}}$  ratio, and response time, which is attributed to the smaller optical bandgap, better absorption, and higher carrier mobility of the three-layered perovskite than that of others (**Figure 7b**). These results drive researchers to develop PDs based on quasi-2D and 2D/3D hybrid MHPs to improve the light absorption as well as the carrier transport, which will be discussed in Section 5.4.

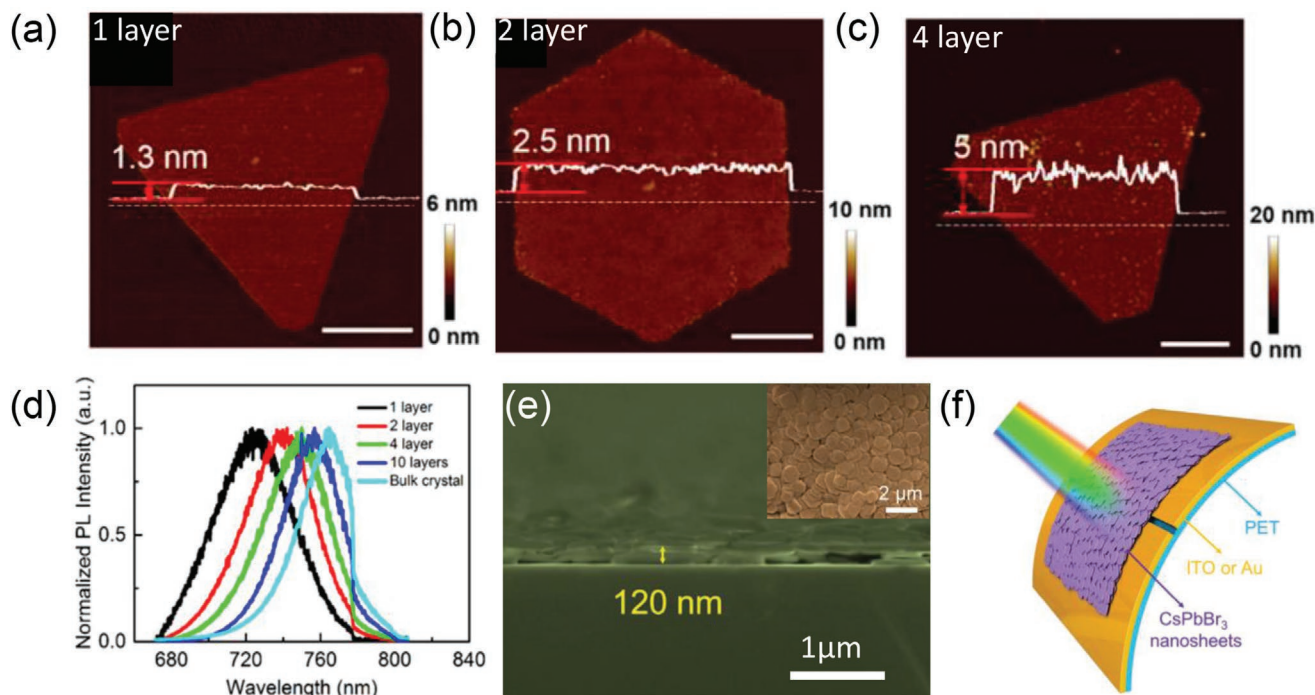


**Figure 6.** a–c) AFM images of 2D MAPbI<sub>3</sub> NSs with different thicknesses (1-, 2-, and 4-unit cell MAPbI<sub>3</sub>). Scale bars: 2 μm. d) Normalized PL spectra of 2D MAPbI<sub>3</sub> NSs with different thicknesses. a–d) Reproduced with permission.<sup>[95]</sup> Copyright 2016, American Chemical Society. e) Top view and cross-sectional SEM images of the CsPbBr<sub>3</sub> NS film; inset: high-resolution SEM image. f) Schematic diagram of the printed flexible 2D MHP PDs. e, f) Reproduced with permission.<sup>[241]</sup> Copyright 2016, Wiley-VCH.

From the perspective of crystalline structures, 2D layered perovskites are like quantum wells originating from their crystal structure in nature. The inorganic layers are sandwiched by organic spacers, leading to quantum and dielectric confinement effects in 2D layered perovskites. The inorganic layers act as “wells” that facilitate the carrier transport, whereas the long-chain organic cations act as “barriers” that hinder the carrier transport. Strategies have been developed to improve the carrier transport, including the investigation of organic spacer cations, the improvement of crystallinity, fabrication of 2D NS networks, and hybrid structures (Figure 7c–f).

Various organic cations, which act as different barriers of quantum wells, could affect the optoelectronic properties of 2D perovskites.<sup>[38,164,244]</sup> He’s group found that the dielectric confinement effect can be modified by inserting organic layers with different dielectric constants.<sup>[14]</sup> Their results demonstrated that the dielectric confinement and  $E_b$  in 2D layered perovskites were largely reduced by using organic cations with a large dielectric constant (Figure 7c), and therefore, the carrier separation efficiency can be significantly improved. From the devices point of view, due to the low- $E_b$  and high carrier mobility, the 2D\_EA perovskite ((HOCH<sub>2</sub>CH<sub>2</sub>NH<sub>3</sub>)<sub>2</sub>PbI<sub>4</sub>) presents better photoexcited carrier extraction efficiency compared to 2D\_PEA perovskite ((PEA)<sub>2</sub>PbI<sub>4</sub>) in terms of  $R$ , photogain, and response time.<sup>[14]</sup> Dong et al.<sup>[164]</sup> demonstrated the  $R$  of 2D-layered MHP-based PDs could be significantly improved by six times via the substitution of butylamine (BA) with iBA cations, where iBA is an isomer to linear  $n$ -BA and has short-branched chains. Moreover, the (iBA)<sub>2</sub>(MA) <sub>$n$ -1</sub>Pb <sub>$n$</sub> I<sub>3 $n$ +1</sub> perovskite films synthesized by the hot-casting method show

improved crystallinity than that synthesized by RT casting, leading to a low dark current, an on/off ratio of 400, and an  $R$  of 117 mA W<sup>-1</sup>.

In terms of improving the crystallinity of 2D MHPs, Peng et al.<sup>[11]</sup> revealed that introducing large spacer organic cations in 2D perovskites may suppress defects formation. Electrically active intrinsic point defects, which lead to unintentional mid-gap defect states including interstitials and vacancies with shallow energy levels, are detrimental to the optoelectronic device performance.<sup>[20]</sup> Therefore, investigations on 2D MHPs with low defect density were reported. PDs based on (PEA)<sub>2</sub>PbI<sub>4</sub>·(CH<sub>3</sub>NH<sub>3</sub>PbI<sub>3</sub>) <sub>$n$ -1</sub> with low defect density can achieve high  $D^*$  of 10<sup>13</sup> Jones due to lower defect levels compared with 3D perovskites.<sup>[11]</sup> Han et al.<sup>[34]</sup> developed 2D layered MHP (C<sub>5</sub>H<sub>11</sub>NH<sub>3</sub>)<sub>2</sub>(CH<sub>3</sub>NH<sub>3</sub>)Pb<sub>2</sub>I<sub>7</sub> (EMA) with high crystalline quality. The hole- $n_{traps}$  is calculated as low as 5.53 × 10<sup>10</sup> cm<sup>-3</sup>, which is much smaller than that of traditional inorganic semiconductors (e.g.,  $n_{traps}$  (polycrystalline Si) = 10<sup>13</sup>–10<sup>14</sup> cm<sup>-3</sup>,  $n_{traps}$  (CdTe) = 10<sup>11</sup>–10<sup>13</sup> cm<sup>-3</sup>, and  $n_{traps}$  (CIGS) ≈ 10<sup>13</sup> cm<sup>-3</sup>, etc.)<sup>[245–247]</sup> and comparable to the reported high-quality 3D single-crystalline MAPbX<sub>3</sub> (10<sup>9</sup>–10<sup>10</sup> cm<sup>-3</sup>).<sup>[248]</sup> Such a low  $n_{traps}$  of EMA promotes carrier transport during laser on/off cycles, which greatly helps to achieve record-high ultrafast response speed of 1.52 μs. Moreover, the high on/off ratio on the order of 1 × 10<sup>3</sup> as well as a low dark current (10<sup>-10</sup> A) also indicates the high crystallinity quality of EMA-based 2D perovskites. However, in both cases above, the large insulating organic cations might be a disadvantage for photoelectric conversion, leading to a low  $R$  of 0.15 A W<sup>-1</sup> for (PEA)<sub>2</sub>PbI<sub>4</sub>·(CH<sub>3</sub>NH<sub>3</sub>PbI<sub>3</sub>) <sub>$n$ -1</sub> ( $n$  = 1, 2, 3) and 3.87 mA W<sup>-1</sup> for EMA.

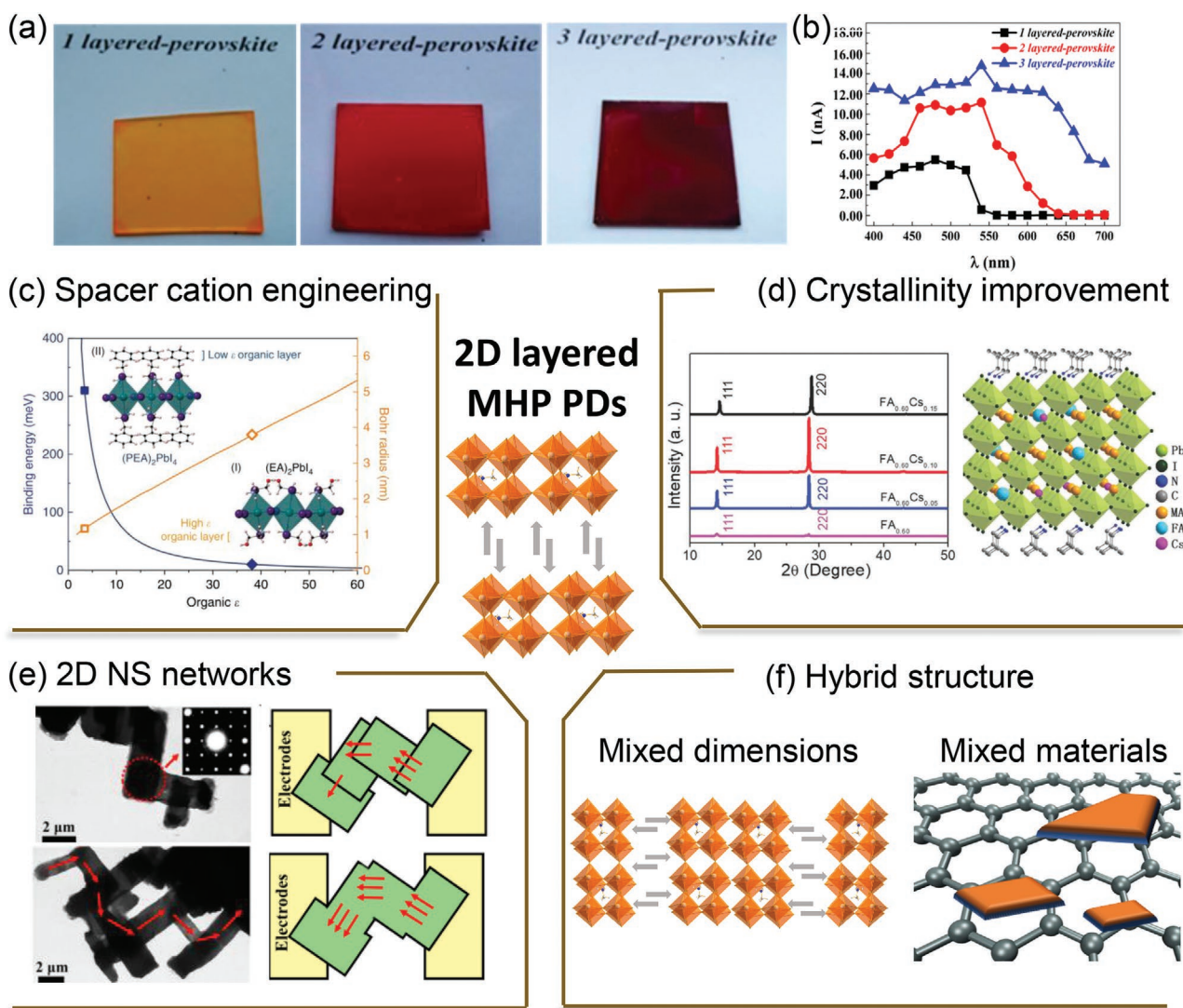


**Figure 7.** a) Photo images of 2D layered perovskite materials with the formula of  $(C_4H_9NH_3)_2(CH_3NH_3)_{n-1}PbI_{3n+1}$  ( $n = 1, 2, 3$ ). b) Wavelength-dependent photocurrent of the PDs based on 2D layered perovskite  $(C_4H_9NH_3)_2(CH_3NH_3)_{n-1}PbI_{3n+1}$  ( $n = 1, 2, 3$ ) with a bias of 30 V. a,b) Reproduced with permission.<sup>[242]</sup> Copyright 2016, American Chemical Society. c) The exciton  $E_b$  and Bohr radius as a function of organic-group dielectric constant in 2D perovskites as predicted by the image charge model. Calculated exciton  $E_b$  and Bohr radii of PEA (square) and EA (diamond) based 2D perovskites are indicated. Reproduced under the terms of the CC-BY 4.0 license.<sup>[14]</sup> Copyright 2018, the Authors, published by Springer Nature. d) XRD characterization of mixed cation (FA and Cs) incorporated layered perovskite  $(iBA)_2((MA_{1-x}FA_x)_{1-y}Cs_y)_3Pb_4I_{13}$  films ( $FA_{0.60}Cs_x$ , ( $x = 0.60, y = 0, 0.05, 0.10, \text{ and } 0.15$ )). Reproduced with permission.<sup>[244]</sup> Copyright 2019, Royal Society of Chemistry. e) TEM images of the 2D  $(OA)_2FA_{n-1}Pb_nBr_{3n+1}$  microplatelets after the intermicroplatelet fusion treatment and schematic illustration of the carrier transport in pristine and treated PDs. The inset shows the single-crystalline essence of the joint. Reproduced with permission.<sup>[257]</sup> Copyright 2017, American Chemical Society. f) Examples of 2D MHP-based hybrid structures.

The mixture of cations in 3D perovskites has the potential to improve the crystallinity and phase stability.<sup>[249–251]</sup> It has been revealed that appropriate incorporation of FA or Cs ions in 2D MHP structures can effectively control the crystallization kinetics and reduce the nonradiative recombination centers to acquire high-quality films, providing additional versatility in fine-tuning the film characteristics.<sup>[244,252–254]</sup> Ho's group investigated mixed cations in 2D MHP-based PDs, where FA and Cs partially substitute MA in 2D layered perovskites.<sup>[244]</sup> XRD patterns were acquired to obtain insights into the crystal structure (Figure 7d). The  $2\theta$  range of  $14^\circ$ – $15^\circ$  and  $28^\circ$ – $29^\circ$  corresponds to the (111) and (220) planes of the perovskite crystal structure.

After Cs incorporation, the stronger diffraction intensity and the smaller FWHM represent an enhanced phase purity and an improved crystallinity. The TRPL decay spectra were conducted to investigate the recombination dynamics. After incorporating with FA and Cs components, all the films exhibit much longer carrier lifetimes than that of the pristine perovskite. The  $(iBA)_2((MA_{0.4}FA_{0.6})_{0.9}Cs_{0.1})_3Pb_4I_{13}$  film displays the longest lifetime of 210.5 ns among the samples, which is  $\approx 52$  times longer than that of the pristine perovskite without Cs<sup>+</sup> doping, indicating the slower recombination characteristics as well as its potentially better device performance. The PDs based on FA- and Cs-doped quasi-2D  $(iBA)_2(MA)_{n-1}Pb_nI_{3n+1}$  perovskites ( $n = 4, (iBA)_2$

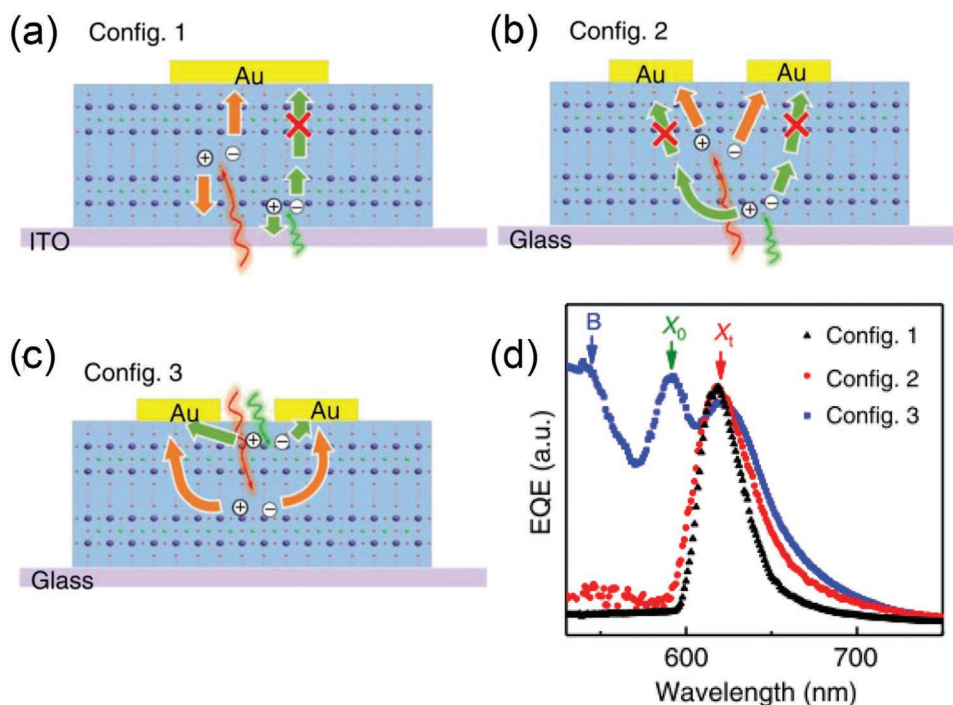


**Figure 8.** a–c) Schematic of the carrier generation and extraction process for three different device configurations: the 2D  $(\text{BA})_2(\text{MA})_{n-1}\text{Pb}_n\text{I}_{3n+1}$  layered perovskite single crystal-based vertical device (Config. 1) and lateral device with illumination from back side (Config. 2) and front side (Config. 3). Red: long-wavelength light and bulk-generated charge carriers. Green: short-wavelength light and surface-generated carriers. d) Normalized EQE spectra of the 2D  $(\text{BA})_2(\text{MA})\text{Pb}_2\text{I}_7$  layered perovskite-based devices with three different configurations. The blue, green, and red arrows represent band-to-band (B), free exciton ( $X_0$ ), and self-trapped state ( $X_i$ ), respectively. a–d) Reproduced under the terms of the CC-BY 4.0 license.<sup>[37]</sup> Copyright 2019, the Authors, published by Springer Nature.

$(\text{MA}_{0.40}\text{FA}_{0.60})_{0.90}\text{Cs}_{0.10})_3\text{Pb}_4\text{I}_{13}$  demonstrate an improved  $R$  of  $400 \text{ mA W}^{-1}$ , a high  $D^*$  up to  $1.68 \times 10^{12}$  Jones and an on/off ratio of  $7.2 \times 10^2$  with fast response speed of 43 and 22 ms for rise and decay time, respectively. Liu et al.<sup>[255]</sup> demonstrated a surface-tension-controlled crystallization method to grow 36 mm sized 2D layered  $(\text{PEA})_2\text{PbI}_4$  single crystals with an even lower  $n_{\text{trap}}$  of  $1.14 \times 10^{10} \text{ cm}^{-3}$ . The PD based on the (001) plane exhibits an ultrahigh EQE of 37 719.6%, an  $R$  of  $139.6 \text{ A W}^{-1}$ , and a  $D^*$  of  $1.89 \times 10^{15}$  Jones, which is two orders of magnitude higher than commercial Si PDs.<sup>[256]</sup> Furthermore, the anisotropic optoelectronic properties of the 2D MHP are demonstrated. The photocurrent of PDs on the in-plane (001) planes is more than 50 times higher than their counterparts on the out-of-plane (010) planes of the 2D  $(\text{PEA})_2\text{PbI}_4$  due to the large anisotropy between the in-plane and out-of-plane electrical conductivity, indicating that the organic cation spacer significantly affects the performance of PDs.

PDs based on MHP NSs usually suffer from the quantum confinement and interfacial charge-carrier scattering problems. Increasing the lateral scale of 2D perovskites can meliorate the problems. However, growing thin but large-scale single-crystalline 2D MHP membranes is still challenging. Yu et al.<sup>[257]</sup> synthesized 2D MHP networks through a postsynthetic treatment, which simultaneously engineers the dimensionality and interface of 2D microcrystalline perovskites and then significantly improves the performance of corresponding PDs. By immersing the 2D perovskites in  $\text{FA}^+$  containing solution, the independent 2D microplatelets are fused and become a 2D

microplatelet network, reducing the quantum confinement and providing an increased mean-free path to reduce carrier hopping (Figure 7e). The EQE and  $R$  of treated PDs (7100% and  $32 \text{ A W}^{-1}$ , respectively) are  $\approx 36$  and 42 times higher than those of the pristine PDs.

Wavelength-selective narrowband PDs are attractive in the field of biomedical sensing, defense, imaging, and machine vision.<sup>[258]</sup> In general, narrowband photodetection can be realized in four strategies: 1) combining a broadband PD with an optical filter, 2) using a material with narrowband photodetection ability, 3) enhancing the absorption in a selected wavelength range by the plasmonic effect, and 4) charge collection narrowing by manipulating the carrier collection efficiency.<sup>[37]</sup> 2D layered MHPs also exhibit the potential for filterless narrowband PDs.<sup>[37,242,258]</sup> Zhou et al.<sup>[242]</sup> observed the selective absorption characteristics of light for layer-structured perovskites. Li et al.<sup>[37]</sup> demonstrated a highly tunable narrowband filterless PD based on 2D perovskites with high EQE (200%), low dark current ( $10^{-12} \text{ A}$ ), and high on/off ratio ( $10^3$ ). The narrowband photodetection ability is ascribed to the extremely low electrical conductivity in the out-of-plane direction of 2D layered perovskites and the enhanced sub-bandgap absorption by self-trapped states (Figure 8). Since incident light with various wavelengths penetrates different distances into materials, the EQE of 2D layered MHP PDs at different wavelengths can be manipulated by engineering the device configurations. The carrier generation and extraction processes are explained in Figure 8a–c. For those device configurations owning the carrier extraction on the different side from the

light-receiving side (Figure 8a,b), the surface photogenerated carriers (i.e., short-wavelength light) have lower collection efficiency due to the extremely low conductivity in the out-of-plane direction of 2D perovskites and high surface recombination losses, and therefore, only those photocarriers generated from specific wavelength range can be collected in these device configurations. From their results, the presence of self-trapped states can enhance light absorption and EQE at the narrowband response range ( $X_t$  in Figure 8d). The density of self-trapped states dramatically increases with the decrease in dimensionality of the systems, thus, 2D layered MHP narrowband PDs are expected to have higher performance than that of their 3D counterparts.

Chiral materials with the ability to emit and detect CPL have attracted increasing attention in recent years for their wide potential applications such as magnetic memory devices, telecommunication, optical information processing, display technologies, and chiral catalysis.<sup>[259–262]</sup> Nevertheless, traditional CPL detectors require an achiral detector with other bulky optical elements such as linear polarizers and quarter waveplates, which cannot meet the demands of miniaturization. With the rapid development of perovskite materials, it has been demonstrated that by incorporating chiral organic ammonium into the lattice of 2D layered perovskites, the chiral 2D perovskites enable miniaturized PDs to detect CPL.<sup>[263–265]</sup> For previous chiral perovskites, CPL emission was only observed at low temperatures. Wang et al. synthesized 2D achiral perovskites ((*S*)- $\alpha$ -(PEA)<sub>2</sub>PbI<sub>4</sub> (left-handed) and (*R*)- $\alpha$ -(PEA)<sub>2</sub>PbI<sub>4</sub> (right-handed)) by single crystal aqueous synthetic method.<sup>[38]</sup> The chiral 2D perovskites (*S*)- $\alpha$ -(PEA)<sub>2</sub>PbI<sub>4</sub> (left-handed) and (*R*)- $\alpha$ -(PEA)<sub>2</sub>PbI<sub>4</sub> (right-handed) exhibit efficient CPL emission and detection at RT. Then, in order to relieve strong electron–photon coupling and improve the charge collection efficiency in 2D layered perovskite optoelectronic devices, Yuan's group first demonstrated the CPL detection capability of chiral quasi-2D perovskites and the corresponding PD showed an *R* of 3.8 A W<sup>-1</sup> and LDR of 102 dB, which are comparable with the best reported results to date.<sup>[39]</sup>

2D layered MHPs have the advantages of great ambient stability, reduced grain boundaries, and fewer surface defects. Moreover, it has been found that 2D layered MHPs have their potentials for wavelength-selective narrowband PDs and CPL detectors. However, from the performance of PDs we summarized in Table 1, the *R* of PDs based on 2D MHPs is generally lower as compared with other structures. This relatively low *R* may be caused by the large  $E_b$ , poor mobility due to the large insulating organic cations, inefficient absorption, or poor contact between 2D perovskites and electrodes. To bring MHP to photoelectronic market, great ambient stability is essential. Since stability of MHPs is the biggest problem limiting their commercial viability and path to market, boosting the performance of stable 2D layered MHP-based PDs becomes increasingly important than any other structures. The potential solution will be summarized in the following section.

#### 5.4. PDs Based on Hybrid Structures

The problems mentioned above might be relieved by constructing hybrid structures. Hybridizing MHPs with different

dimensions or other materials to form heterostructures has been considered as an alternative and effective approach for enhancing the performance of PDs as well as their stability. Based on this concept, a variety of high-performance PDs based on MHP hybrid structures have been reported. In this section, we divide hybrid perovskite structures into two parts: mixed/hierarchical dimensions and mixed materials.

##### 5.4.1. Mixed or Hierarchical Dimensions

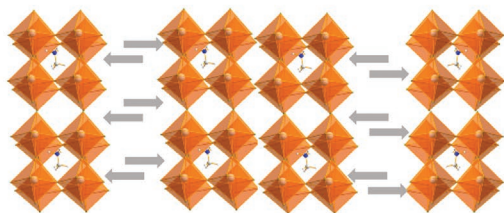
Dimensional tailoring, such as mixed or hierarchical dimensions, is a promising approach to simultaneously boost the performance and stability of optoelectronic devices (Figure 9a).<sup>[139,266–269]</sup> Nazeeruddin's group first developed an innovative concept by engineering a multidimensional junction made of 2D/3D perovskites, which takes advantage of great stability of 2D layered MHPs and high absorption and excellent charge transport of the 3D ones, indicating the possibility of practical application for MHPs. The solar cells based on the 2D/3D perovskites demonstrate promising one-year stability with an efficiency of 14.6%.<sup>[270]</sup> Snaith's group then demonstrated 2D/3D perovskite solar cells with stability over 4000 h and a high efficiency of 17.5%.<sup>[271]</sup> These promising results have attracted tremendous attention to mixed-dimensional MHPs for next-generation optoelectronic devices.

Generally, 2D layered perovskites with  $n > 4$  are referred to as quasi-2D perovskites. With  $n$  increasing, a quasi-2D perovskite is equivalent to fitting 3D perovskites into long-chain organic spacer cation structures. Therefore, the material properties of quasi-2D perovskites fall between 3D and 2D perovskites. Zhou et al.<sup>[242]</sup> first demonstrated that PDs based on three-layered perovskite have higher *R*, higher on/off ratio, and faster response speed than those based on one-layered perovskite (perovskite formula: (C<sub>4</sub>H<sub>9</sub>NH<sub>3</sub>)<sub>2</sub>(MA)<sub>*n*-1</sub>Pb<sub>*n*</sub>I<sub>3*n*+1</sub> ( $n = 1, 2, 3$ ); the thickness of perovskite films with  $n = 1, 2, 3$ , are 260, 690, and 560 nm, respectively). Then, Ho's group reported the studies of the layer number and organic cation of quasi-2D MHPs.<sup>[164,244]</sup> The PDs based on quasi-2D (iBA)<sub>2</sub>(MA)<sub>*n*-1</sub>Pb<sub>*n*</sub>I<sub>3*n*+1</sub> perovskite films show the higher *R*, higher on/off ratio, and faster response speed than PDs based on 2D layered perovskite film with  $n = 1$  (the thickness of perovskite films with  $n = 1, 2, 3, 4$  are 665, 405, 540, and 419 nm, respectively). Wang et al.<sup>[243]</sup> demonstrated a fast synthetic method to grow inch-scale quasi-2D MHPs (perovskite formula: (C<sub>4</sub>H<sub>9</sub>NH<sub>3</sub>)<sub>*n*</sub>(CH<sub>3</sub>NH<sub>3</sub>)<sub>*n*-1</sub>Pb<sub>*n*</sub>I<sub>3*n*+1</sub> ( $n = 1, 2, 3, 4, \infty$ ); the film thickness is unclear). The spontaneous alignment of alkylammonium and high chemical potentials of precursor molecules at the water-air interface enable fast in-plane crystal growth of quasi-2D MHPs with a uniform orientation at the water-air interface. They found the PDs based on perovskites with higher  $n$  represent better *R*. Interestingly, the PD based on the 2D layered perovskite with  $n = 1$  exhibits the highest on/off ratio of  $\approx 10^4$  and the fastest response time ( $\tau_{\text{rise}} = 1.7 \mu\text{s}$  and  $\tau_{\text{decay}} = 3.9 \mu\text{s}$ ) in comparison to those of PDs based on quasi-2D perovskites with larger quantum well thicknesses ( $n > 1$ ), which shows an opposite trend to previous studies. They explained that the ion migration in perovskites, which hinders the charge transport, can be relieved in low-dimensional

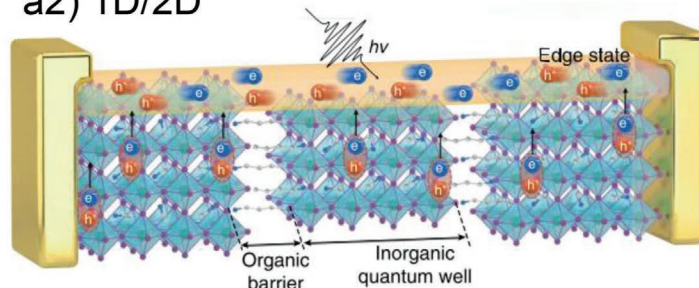


## (a) Dimensional tailoring

a1) 2D/3D



a2) 1D/2D



## (b) Mixed materials

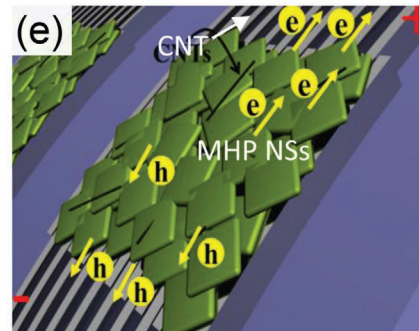
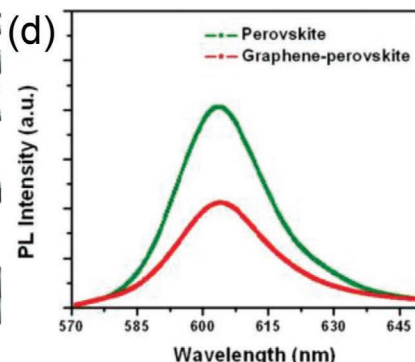
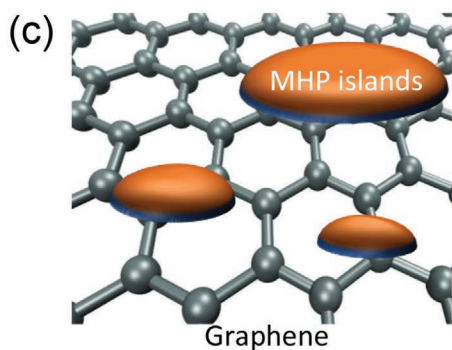
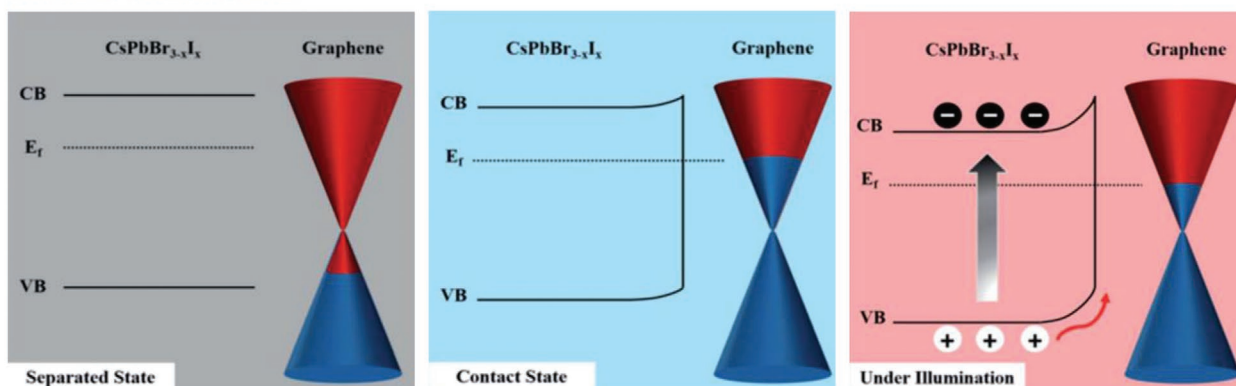


**Figure 9.** a1) Examples of mixed-dimensional MHP structures. a2) Schematics of carrier dynamics in single-crystalline (101)-oriented  $(\text{BA})_2(\text{MA})_{n-1}\text{Pb}_{n-1}\text{I}_{3n+1}$  layered perovskite NW-based PDs. a1,a2) Reproduced with permission.<sup>[31]</sup> Copyright 2018, Springer Nature. b–e) Examples of mixed materials system (carbon-based nanostructure/perovskite hybrid systems). b) Energy diagram of graphene/ $\text{CsPbBr}_{3-x}\text{I}_x$  NC PDs in the separated state (left) and contact state under dark (middle) and illumination (right). Reproduced with permission.<sup>[276]</sup> Copyright 2016, Royal Society of Chemistry. c) Schematic of MHP islands on graphene. d) PL spectra excited at 532 nm of pure perovskite (green) and graphene–perovskite (red) thin films. Reproduced with permission.<sup>[199]</sup> Copyright 2015, Wiley-VCH. e) Schematic of the  $\text{CsPbBr}_3$  NS film and CNTs. Reproduced with permission.<sup>[35]</sup> Copyright 2017, American Chemical Society.

perovskites, consequently giving rise to a faster response speed. Moreover, the smaller quantum well structure can effectively confine the charge transport within the “well” and drastically reduce the dark current ( $\approx 10^{-13}$  A for 2D perovskite with  $n = 1$ ), resulting in a high on/off ratio. Unlike solar cells based on quasi-2D or 2D/3D perovskites studied intensively, PDs based on multidimensional perovskites are still in their infancy. As the thickness of quasi-2D MHP films is different or even unknown in the studies summarized above, it is hard to make a comparison of material or device studies among MHPs with different  $n$ . More systematic studies are still needed.

In addition to involving 3D MHPs into 2D layered structures for improving absorption and carrier transport, Zhang's group designed layered MHPs in the form of 1D NW for more efficient exciton dissociation, free-carrier generation and transport.<sup>[31]</sup> It is found that with the layer number  $n > 2$ , lower-energy local states at the edges dominate the photophysics of layered MHPs. These states provide a more conductive channel for exciton dissociation and free carrier transport.<sup>[25,124]</sup> The carrier generation and extraction processes of layered MHP NWs are demonstrated in Figure 9a1. Photocarriers generated in perovskite NWs transport through conductive

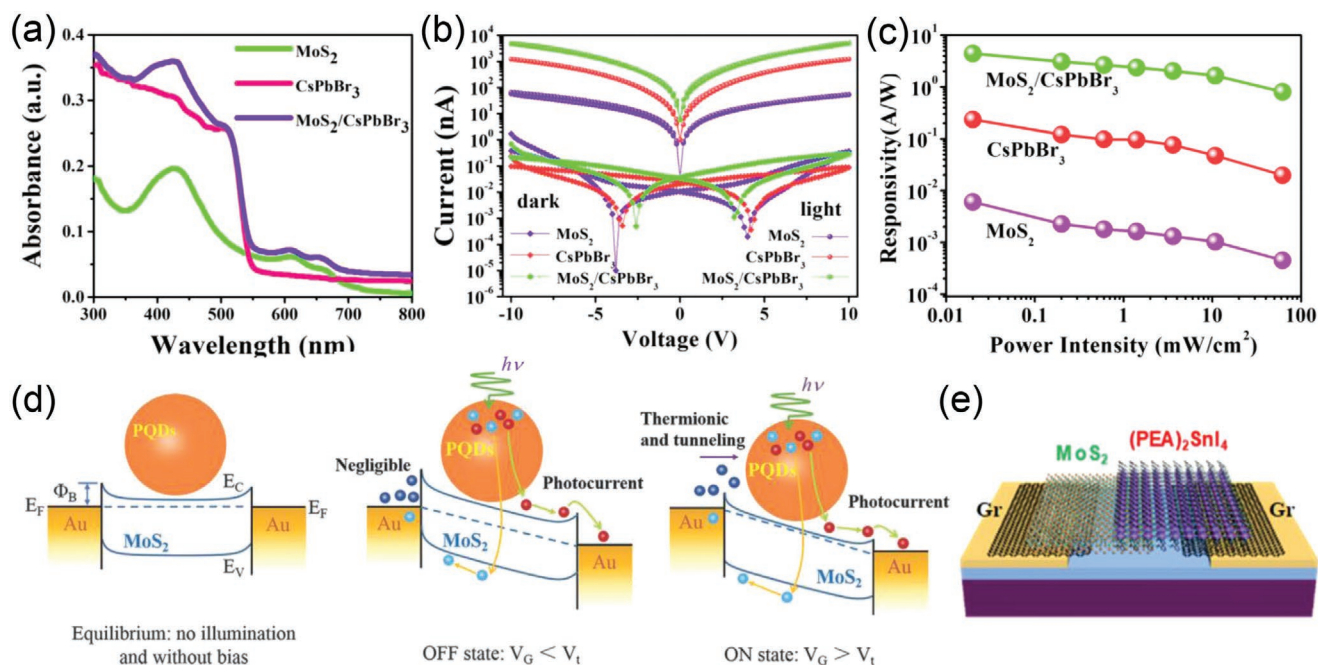


**Figure 10.** Examples of mixed materials system (TMD/perovskite hybrid systems). a) UV-vis absorption spectra of MoS<sub>2</sub>, CsPbBr<sub>3</sub>, and MoS<sub>2</sub>/CsPbBr<sub>3</sub> hybrid film. b) *I*-*V* characteristics of the PDs based on CsPbBr<sub>3</sub> NS layers with or without MoS<sub>2</sub>, in darkness and under 442 nm laser illumination. c) Photoresponsivity of the PDs based on MoS<sub>2</sub>, CsPbBr<sub>3</sub>, and MoS<sub>2</sub>/CsPbBr<sub>3</sub> hybrid film as a function of the power intensity. a-c) Reproduced with permission.<sup>[143]</sup> Copyright 2017, American Chemical Society. d) The schematic illustration of channel current transport mechanism and energy band diagram of the mixed-dimensional van der Waals heterostructure based phototransistors under equilibrium conditions (left), OFF-state (middle), and ON-state (right). Reproduced with permission.<sup>[282]</sup> Copyright 2018, Wiley-VCH. e) Schematic of the graphene/2D (PEA)<sub>2</sub>SnI<sub>4</sub>/MoS<sub>2</sub>/graphene device under different bias. Reproduced with permission.<sup>[279]</sup> Copyright 2019, American Chemical Society.

inorganic layers to the edge pathways. The design of layered MHP NW arrays possesses the advantage of 2D layered perovskites (insulating long-chain organic barriers for suppressing the dark current) and improves the carrier extraction by increasing the exposed crystalline edges, giving rise to a high-performance PD (*R* exceeding  $1.5 \times 10^4 \text{ A W}^{-1}$  and *D*\* exceeding  $7 \times 10^{15}$  Jones).

Li's group developed 2D/2D MHP heterostructures (C<sub>4</sub>H<sub>9</sub>NH<sub>3</sub>)<sub>2</sub>PbI<sub>4</sub>/(C<sub>4</sub>H<sub>9</sub>NH<sub>3</sub>)<sub>2</sub>(CH<sub>3</sub>NH<sub>3</sub>)PbI<sub>7</sub> by diffusion-controlled growth method for narrow dual-band photodetection.<sup>[258]</sup> Wavelength-selective PDs with multiple narrowband spectral response could be applied in a variety of areas such as remote-sensing, mineral exploration, and biological medicine. PDs based on the 2D/2D perovskite heterostructures exhibit low dark current ( $\approx 10^{-12}$  A), high on/off ratio ( $\approx 10^3$ ), and highly narrow dual-band spectral response with the FWHM of 20 and 34 nm at wavelengths of 540 and 610 nm, respectively.

#### 5.4.2. Hybrid Materials

PDs based on pure MHPs have their intrinsic limitations. The most serious problems are the high *E<sub>b</sub>* and limited carrier mobility. Although several strategies have been proposed, the progress is still limited. To tackle this problem, hybridizing low-dimensional MHPs with other materials to form heterostructures has been considered as an alternative and effective approach to break the bottleneck and further enhance the performance of perovskite PDs (Figures 9 and 10). Forming hybrid material

systems can take advantage of the properties of each material. Since nanostructured perovskite films generally have strong absorption but high *E<sub>b</sub>* and low carrier mobility, materials chosen for the incorporation of hybrid systems mainly have the capability to improve the carrier separation and transportation. Based upon this concept, a variety of high-performing PDs based on mixed materials have been reported, such as PDs based on the perovskite-graphene, perovskite-PCBM,<sup>[272]</sup> perovskite-transition metal dichalcogenides (TMDs) hybrid material systems, etc.

**Carbon-Based Nanostructure/Perovskite Hybrid Systems:** The ultrahigh carrier mobility ( $\approx 200\,000 \text{ cm}^2 \text{ V}^{-1} \text{ s}^{-1}$ ) makes graphene attractive to be combined with perovskite PDs as a channel material. High-performance PDs based on the hybridization between graphene and MHPs have been reported in recent years. Cho's group first demonstrated graphene/perovskite heterostructured PDs.<sup>[273]</sup> The hybrid devices (polycrystalline MAPbI<sub>3</sub> films/graphene PDs) exhibit superior performance with 1, 2, and 5 of magnitude of the enhancement of *R* ( $180 \text{ A W}^{-1}$ ) in comparison with pure MAPbI<sub>3</sub> PDs ( $6.1 \text{ A W}^{-1}$ ),<sup>[274]</sup> MAPbI<sub>3</sub>/ITO PDs ( $3.49 \text{ A W}^{-1}$ ),<sup>[193]</sup> and pure graphene PDs ( $10^{-3} \text{ A W}^{-1}$ ),<sup>[275]</sup> respectively. The dramatical enhancement is attributed to not only the photogating effect of the hybrid structures but also the combination of the superior electronic characteristics of graphene and the high absorption cross-section of MHPs, which simultaneously maximizes both the light harvesting and the photoinduced carrier extraction. When electron-hole pairs generate in this hybrid system, electrons in the graphene layer transfer to the perovskite layer and fill the

empty states in the valence band of perovskites. The trapped electrons generate an electric field that shifts Fermi level ( $E_F$ ) of graphene, resulting a band bending at the perovskite/graphene interface, which facilitates the carrier collection (Figure 9b); photogenerated holes transfer to graphene and alter the conductivity of the graphene channel through capacitive coupling, leading to photogating effect. Since electrons trapped in perovskites would get a long lifetime, holes in the graphene would recirculate many times, resulting in an increase in conductivity and ultrahigh photoconductive gain. These devices working on the strong photogating effect can exhibit several orders of magnitude higher  $R$  values than others (Table 1).

Although a promising improvement has been made compared with pure perovskite devices, the photoconductive gain is not yet comparable to other graphene-based heterostructure PDs due to the high bulk recombination rate of photocarriers in thick polycrystalline MHP films. The photogenerated holes might be trapped within the perovskite films before transfer to graphene. Therefore, single-crystalline nanostructured perovskite/graphene heterostructures have their potential to further improve the photodetection performance. Wang et al.<sup>[199]</sup> demonstrated hybrid PDs that consist of monolayer graphene covered with a thin layer of dispersive MAPbBr<sub>2</sub>I islands, which show high  $R$  ( $\approx 6.0 \times 10^5 \text{ A W}^{-1}$ ) and high photoconductive gain ( $\approx 10^9$ ). The PL quenching behavior and shortened photocarrier lifetime suggest efficient charge transfer between graphene and perovskite in Figure 9c,d. Kwak et al.<sup>[276]</sup> reported all-inorganic 0D CsPbBr<sub>3-x</sub>I<sub>x</sub> NC/graphene PDs with a high  $R$  of  $8.2 \times 10^8 \text{ A W}^{-1}$  and an ultrahigh  $D^*$  of  $2.4 \times 10^{16}$  Jones under 405 nm illumination ( $0.07 \mu\text{W cm}^{-2}$ ), which are much higher than those of PDs based on pure perovskite NCs, indicating a significant improvement of carrier transfer by introducing graphene in PDs. Horváth's group demonstrated 1D MAPbI<sub>3</sub> NW network/graphene PDs.<sup>[277]</sup> The ultrahigh  $R$  of  $\approx 2.6 \times 10^6 \text{ A W}^{-1}$  is measured under a low incident power of 3.3 pW, which is 4 orders of magnitude higher than polycrystalline MAPbI<sub>3</sub> film/graphene PDs. The results demonstrate that nanostructured perovskites are a superior candidate than polycrystalline perovskite films for graphene-based heterostructure PDs.

Photogenerated carriers transferring between MHPs and graphene could also be trapped by trapped states at the interfaces, which is a particularly serious problem in nanostructures due to their high surface-to-volume ratio. 2D layered perovskites can dramatically reduce defects and notably enhance carrier diffusion length.<sup>[215]</sup> Tan et al.<sup>[101]</sup> first reported PDs based on 2D layered perovskite (C<sub>4</sub>H<sub>9</sub>NH<sub>3</sub>)<sub>2</sub>PbBr<sub>4</sub>/graphene hybrid system. The PDs based on the 2D/2D hybrid structure exhibit low dark current ( $\approx 10^{-10}$  A), indicating less recombination in the system due to reduced defect density. Moreover, 2D layered perovskite/2D material heterostructures with the out-of-plane van der Waals bonding have no surface dangling bonds and thus atomically sharp interfaces, which are particularly important for high-performance PDs with low noise.<sup>[278]</sup> Furthermore, the van der Waals bonding in 2D perovskite/2D material heterostructures can eliminate the influence of lattice matching and deposition temperature, providing a significant advantage over 3D material-based heterostructures.<sup>[279]</sup>

Apart from 2D graphene, carbon nanotube (CNT) or carbon QDs are also developed for constructing conductive carrier

tracks for perovskite PDs.<sup>[35,280]</sup> The perovskite/CNT or carbon QDs composite films exhibit both high light harvesting and high conductivity, offering the potential for corresponding high-performance PDs. The PDs based on CsPbBr<sub>3</sub> NS/CNT were reported by Li et al., showing a high EQE of 7488% and high responsivity of  $31.1 \text{ A W}^{-1}$  (Figure 9e).<sup>[35]</sup> Besides, the efficient charge extraction also contributes to the fast response speed ( $\tau_{\text{rise}} = 16 \mu\text{s}$ ) of the hybrid PDs.

The above results demonstrate that by introducing carbon-based materials into low-dimensional MHP PDs, the photodetection performance has a significant enhancement than pure perovskite PDs. However, the bandgapless graphene usually leads to high  $I_{\text{dark}}$ , and thus low  $I_{\text{light}}/I_{\text{dark}}$  ratio, low  $D^*$ , and high NEP of the hybrid devices.<sup>[281]</sup> Therefore, TMDs such as MoS<sub>2</sub>, MoSe<sub>2</sub>, WS<sub>2</sub>, and WSe<sub>2</sub> become popular candidates for the hybridization with perovskites because of their high carrier mobility, tunable bandgap, and low driving currents.

**TMD/Perovskite Hybrid Systems:** Kang et al.<sup>[160]</sup> first demonstrated perovskite films/TMD hybrid structures for PD applications. The MAPbI<sub>3</sub>/MoS<sub>2</sub> heterojunction is capable of sensing light over the entire visible and NIR wavelength ranges due to the broadening of light absorption spectrum of hybrid materials. The corresponding device exhibits an enhanced  $I_{\text{light}}$  (eight times higher than pristine MoS<sub>2</sub>-based devices), an  $R$  of  $4.9 \times 10^3 \text{ A W}^{-1}$ , and a  $D^*$  of  $8.76 \times 10^9$  Jones under 520 nm light ( $6 \text{ mW cm}^{-2}$ ). By adopting a new encapsulation bilayer of octadecyltrichlorosilane (OTS)/poly(methyl methacrylate) (PMMA), the degradation of performance is less than 20% after a continuous operation of 200 h.

Song et al.<sup>[143]</sup> presented a nanostructured perovskite/TMD hybrid system for PD applications. Figure 10a shows the enhanced light absorbance of the heterostructure at the wavelength range of 350 to 500 nm after introducing MoS<sub>2</sub>. The PD based on 2D CsPbBr<sub>3</sub> NS/MoS<sub>2</sub> shows an  $R$  of  $4.4 \text{ A W}^{-1}$  and an EQE of 302%. The value of the  $I_{\text{dark}}$  for the CsPbBr<sub>3</sub>/MoS<sub>2</sub>, CsPbBr<sub>3</sub>, and MoS<sub>2</sub> devices is approximately in the same range of 0.1–1 nA, and the photocurrents of the three devices are 5030, 1230, and 54 nA, respectively, suggesting the improved on/off ratio of the hybrid PDs (Figure 10b,c). Wu et al.<sup>[282]</sup> demonstrated PDs based on all-inorganic perovskite QDs (CsPbI<sub>3-x</sub>Br<sub>x</sub>) integrated with MoS<sub>2</sub> heterostructures, and the optimized device exhibits an extremely high  $R$  of  $77 \times 10^4 \text{ A W}^{-1}$ , a  $D^*$  of  $\approx 5.6 \times 10^{11}$  Jones, and an ultrahigh EQE exceeding 107%. The promising performance is derived from the synergistic effect of photogating effect and the modulation of Schottky barriers.<sup>[283]</sup> A favorable energy band alignment between TMDs and MHPs in the hybrid systems facilitates interfacial photocarrier separation and efficient carrier injection into the MoS<sub>2</sub> layer (Figure 10d). The presence of the built-in field reduces carrier recombination and suppresses the  $I_{\text{dark}}$ .

To further reduce the  $I_{\text{dark}}$  caused by traps at interfaces between perovskite/2D materials, 2D layered perovskite/2D material hybrid structures are great candidates. The exfoliated 2D layered perovskite (BA)<sub>2</sub>(MA)<sub>n-1</sub>Pb<sub>n</sub>I<sub>3n+1</sub> flakes/MoS<sub>2</sub> hybrid PDs exhibit superior performance with  $\approx 6$  orders of magnitude enhancement of  $R$  ( $10^4 \text{ A W}^{-1}$ ) and 2 orders of magnitude enhancement of  $D^*$  ( $4 \times 10^{10}$  Jones) in comparison with pure perovskite counterparts, which demonstrates the facile charge transfer between the two 2D materials.<sup>[284]</sup> Li's group<sup>[279]</sup> reported graphene/2D perovskite (PEA)<sub>2</sub>SnI<sub>4</sub>/MoS<sub>2</sub>/graphene

heterojunction PDs as shown in Figure 10e. By using few-layer graphene flakes as electrical contacts, which can form good contacts with both MoS<sub>2</sub> and Au electrodes, the performance of the heterostructures can be further improved. The device exhibits an  $R$  of 1100 A W<sup>-1</sup> at 3 V bias, a response speed of ≈40 ms under zero bias, and a high rectification ratio of 500. Importantly, the EQE can achieve 38.2% at zero bias, which is comparable or even higher than that of 3D perovskite/2D material PDs.

In addition to improving the carrier separation and collection, mixed materials can also enhance the light harvesting through various approaches, such as up/downconversion and plasmonic coupling.<sup>[200,217,285–287]</sup> Liu's group extended the response range of PDs to the NIR (≈1100 nm) by integrating the up-conversion material (NaYF<sub>4</sub>:Yb,Er QDs) with low-dimensional perovskites to absorb NIR light.<sup>[285]</sup> The PDs based on  $\alpha$ -CsPbI<sub>3</sub> QD/NaYF<sub>4</sub>:Yb,Er QDs are capable of broad-bandwidth photodetection from the deep UV to the NIR region (260–1100 nm) with a high  $R$ . Similarly, the PDs based on MAPbI<sub>3</sub> microwires/NaYF<sub>4</sub>:Yb,Er QDs exhibit enhanced NIR photodetection capability (Figure 11a,b), with an  $R$  of 0.27 A W<sup>-1</sup> and  $D^*$  of  $0.76 \times 10^{12}$  Jones under 980 nm light.<sup>[200]</sup> CsPbBr<sub>3</sub> NC PDs enhanced by the localized surface plasmon resonance (LSPR) of Au NCs were demonstrated by Dong et al.<sup>[217]</sup> Figure 11c–f presents the performance of PDs with and without Au NCs. The  $R$  of Au NC plasma-enhanced PD measured under 520 nm is 10.04 mA W<sup>-1</sup> at 2 V bias, exhibiting an improvement of 213% compared with pristine 4.71 mA W<sup>-1</sup>. The  $I_d$  of both devices are in the same range of nA and the  $I_p$  of Au-plasma enhanced PDs increase from 245.6 to 831.1  $\mu$ A at 2 V bias (an improvement of 3.38 times), leading to an improved on/off ratio and  $D^*$ . Perovskite QDs with strong UV absorption were also integrated with Si PDs by Lu et al. and Zhong's group.<sup>[286,287]</sup> The perovskite QDs improve the light harvesting by the self-absorption of the QDs film as well as the scattering effects.

In short, due to the natural limitations of a single nanostructured perovskite, PDs based on hybrid structures start to attract much attention. The above results of hybrid structures demonstrate a significant enhancement of the photodetection performance over pure perovskite PDs, which have been considered as a promising device architecture. Nevertheless, studies on heterostructures based on nanostructured perovskites and other materials are still new and there are still some problems needed to be addressed. For example, the slow response time of phototransistors would limit the progress of these mixed materials hybrid system. It is noted that the response time of most mixed materials phototransistors summarized in Table 1 is typically in a range of hundred milliseconds to seconds, which is much higher than conventional PDs. PDs based on 2D–2D heterostructures suffer from limited performance due to the strong interlayer coupling,<sup>[288]</sup> weak optical absorption, and limited carrier mobility. Mixed-dimensional material systems such as quasi-2D perovskite/MoS<sub>2</sub> could be the next popular candidate for PDs.

## 6. Stability and Flexibility of PDs Based on Low-Dimensional MHPs

Despite the unique optical and optoelectronic properties of MHPs, the instability remains a crucial challenge for their

application in optoelectronic devices. Organic–inorganic hybrid halide perovskites intrinsically suffer from stability issues such as degradation when exposed to moisture, oxygen, heat, UV light, mechanical stress, and under reverse bias.<sup>[21]</sup> Many previous researchers have reported the instable properties of MHP films or bulk crystals. The intrinsic chemical instability makes MHPs decompose easily and perform poor thermal and moisture stability. Take MAPbX<sub>3</sub> as an example, it can gradually decompose to PbX<sub>2</sub> and several volatile products under exposure to various environmental factors, including moisture, heat, oxygen, and light.<sup>[50,289,290]</sup> Another form of instability in MHPs comes from the polymorphism, especially identified in iodide-based MHPs, where the size of A-site cations is not suitable to be included in Pb-iodide cages, resulting in the phase transition from 3D MHP polymorphs to those of a lower dimensionality and a wider bandgap.<sup>[291,292]</sup> Moreover, MHPs may decompose when exposed to nearly all polar organic solvents owing to their ionic bonding character.

The instability issues mentioned above also remain in low-dimensional MHPs. However, it is worthwhile to mention that the change of dimensionality of MHPs indeed influences the stability to some extent. For instance, limiting the size of CsPbX<sub>3</sub> in nanoscale can form the metastable alpha phase at RT.<sup>[293,294]</sup> Protesescu et al. found that in contrast to the instable cubic-phase CsPbX<sub>3</sub> bulk crystals at RT, CsPbX<sub>3</sub> NCs exhibit improved cubic-phase stability.<sup>[52]</sup> CsPbX<sub>3</sub> NCs with the size of 4–15 nm can remain fully stable in the cubic phase at RT, which is attributed to the large contribution of surface energy. Swarnkar et al. also verified the contribution of the nanostructure to the phase stability of CsPbI<sub>3</sub> NCs at RT.<sup>[293]</sup> This is an exciting result for perovskite development.

The incorporation of low-dimensional MHPs broadens the application of perovskites with different compositions, such as all-inorganic perovskites, which have superior stability against oxygen and moisture than that of hybrid organic–inorganic perovskites. Therefore, the intrinsic instability of MHPs due to the inevitable decomposition and volatilization of organic components could be eliminated to some extent. Yang et al. demonstrated that PDs based on all-inorganic perovskite  $\alpha$ -CsPbI<sub>3</sub> nanorods behave steadily with nearly no reduction in the current intensity after being stored under ambient conditions for one week.<sup>[237]</sup> Besides, it is reported that adding polymers can improve the stability of devices based on low-dimensional MHPs. Chen et al. found the PD device based on CsPbI<sub>3</sub> NWs arrays with poly-vinylpyrrolidone (PVP) maintain 90% of its initial performance after 30 days of storage in ambient conditions, suggesting their stability under ambient conditions.<sup>[294]</sup> By introducing PVP into CsPbI<sub>3</sub> precursors, the black  $\alpha$  phase CsPbI<sub>3</sub> can keep stable with no obvious change in the XRD patterns after 30 days, while the sample without PVP shows yellow  $\delta$  phase, because polymers play an important role by passivating the crystal surface and restricting the crystal growth of low-dimensional MHPs.<sup>[295,296]</sup>

As we mentioned in Section 5.3, 2D layered MHPs have much greater environmental stability compared to their 3D or other low-dimensional counterparts because hydrophobic organic long-chain spacers would prevent [MX<sub>6</sub>]<sup>4-</sup> octahedral slabs from directly contacting with moisture in ambient conditions. For example, 2D (C<sub>4</sub>H<sub>9</sub>NH<sub>3</sub>)<sub>2</sub>PbBr<sub>4</sub> nanobelts exhibit

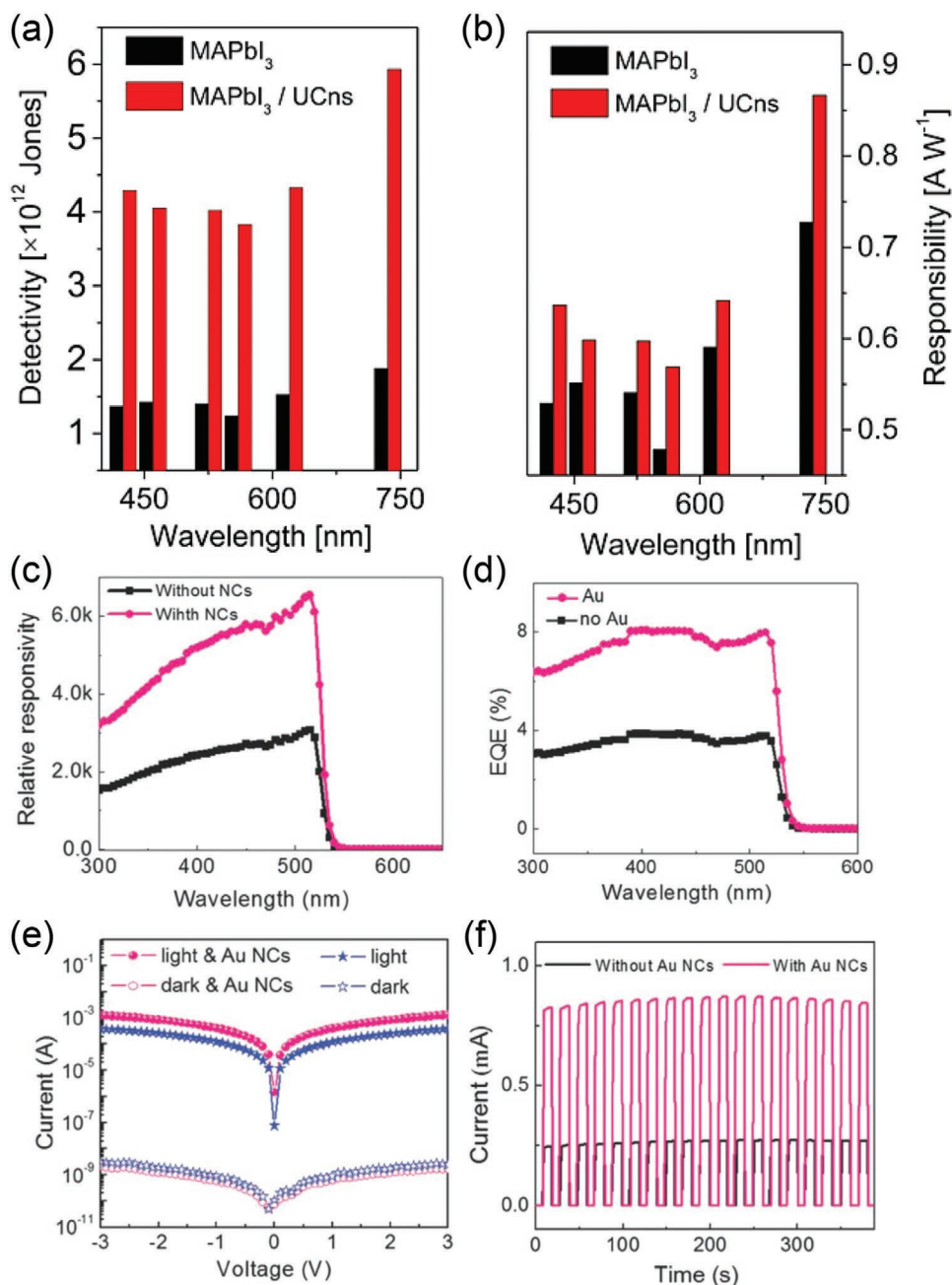


**Figure 11.** a) The  $D^*$  and b)  $R$  of MAPbI<sub>3</sub> microwire PDs with and without upconversion nanoparticles (UCNs) in the visible regions. Reproduced with permission.<sup>[200]</sup> Copyright 2017, American Chemical Society. c) Relative responsivity and d) EQE spectra of CsPbBr<sub>3</sub> NC-based devices with and without Au nanoparticles under 2 V bias from front illumination. e)  $I$ - $V$  characteristics of CsPbBr<sub>3</sub> NC-based PDs with and without Au nanoparticles under 532 nm laser (4.65 mW cm<sup>-2</sup>). f) The reproducible  $I$ - $t$  curves of CsPbBr<sub>3</sub> NC-based PDs with and without Au nanoparticles under 532 nm laser illumination (4.65 mW cm<sup>-2</sup>) at 2 V bias. c-f) Reproduced with permission.<sup>[217]</sup> Copyright 2016, Wiley-VCH.

high stability under ambient conditions without any phase degradation after 20 days of storage.<sup>[224]</sup> Song et al. recorded the photocurrent changes of the 2D CsPbBr<sub>3</sub> NS PDs under ambient conditions.<sup>[241]</sup> The devices exhibit high stability during irradiating for 12 h with a 442 nm laser (10 mW cm<sup>-2</sup>). Han et al. performed the switching operation by measuring the photocurrent of 2D layered perovskite (C<sub>5</sub>H<sub>11</sub>NH<sub>3</sub>)<sub>2</sub>(CH<sub>3</sub>NH<sub>3</sub>)Pb<sub>2</sub>I<sub>7</sub> PDs for 10<sup>5</sup> switching cycles in 10<sup>4</sup> s;<sup>[34]</sup> Liu et al. showed

photostability of on/off switching behavior of 2D (PEA)<sub>2</sub>PbI<sub>4</sub> PDs over 5000 s (2530 on/off cycles).<sup>[255]</sup> The photocurrent signals of both results maintain almost unchanged after the switching operation, indicating the high stability and reliability of 2D layered MHP devices.<sup>[34,255]</sup> Moreover, He and co-workers studied the influences of surface conditions on the optoelectronic properties and moisture stability of 2D layered MHP.<sup>[30]</sup> Smooth 2D MHP achieves the  $D^*$  of  $2.6 \times 10^{13}$

Jones, which is 23.6 times higher than that of the rough MHP and the better moisture resistance due to defect-free surface and relatively continuous organic linker of the smooth MHP. Their results reveal the strong dependence of the stability and optoelectronic properties of 2D layered MHPs on their surface conditions.

Besides, Deng et al. showed PDs fabricated from MAPbI<sub>3</sub> microwire arrays exhibit long-term stability of >50 days in air; by contrast, the PDs made with polycrystalline MAPbI<sub>3</sub> films gradually degrade with time and nearly fully degrade after 40 days.<sup>[32]</sup> The result indicates that devices made with microwire arrays have much higher resistance to degradation than those based on thin films, which is attributed to the highly crystalline structures, fewer grain boundaries, and the unique 1D enclosing surfaces. However, some researches show that 1D wire structures may catalyze the decomposition of perovskites when exposed to moisture and light due to their large surface area, and the stability of MHP NWs largely depends on their crystalline quality and surface morphology.<sup>[36,155]</sup> More detailed studies are still needed.

Mechanical stress and strain affect the rate of perovskite degradation and reduce the intrinsic stability of perovskite films to moisture, heat, and light.<sup>[21]</sup> PDs based on low-dimensional structures can release part of mechanical stress, thus enabling the fabrication of flexible devices. Many groups demonstrated the  $I_{\text{light}}/I_{\text{dark}}$  ratio of the flexible PDs based on low-dimensional MHPs bent with various radii remained nearly unchanged (Figure 12).<sup>[32,33,35,224,227,239,241,297]</sup> Song and Zeng's group presented the outstanding flexibility (>10 000 cycles) of PDs with low-dimensional MHPs (Figure 12a–c).<sup>[33,35,241]</sup> Zhu et al. compared the flexibility of PDs made by (C<sub>4</sub>H<sub>9</sub>NH<sub>3</sub>)<sub>2</sub>PbBr<sub>4</sub> nanobelts and microplatelets.<sup>[224]</sup> Their results demonstrate that during the bending test, the switching ratio of nanobelt-based PDs decrease slightly after 1000 bending cycles while that of microplatelet-based PDs show a sharp drop, indicating the better flexibility of nanobelt structures (Figure 12d–g).<sup>[224]</sup>

In addition to phase, environmental and mechanical stability, ion migration is another limit factor for the long-term operational stability of MHP-based devices. Recent studies have indicated that the ion migration could be suppressed in low-dimensional MHPs both in the dark and under illumination, though this area is not fully explored yet.<sup>[298,299]</sup> Huang and co-workers found the ion-migrating activation energy in 2D perovskites is much higher than that of their 3D counterparts, which is beneficial for device stability.<sup>[298]</sup>

Generally, low-dimensional perovskites have shown signs of better stability than polycrystalline ones, including phase stability, environmental stability, mechanical stability, and suppressed ion migration. Low-dimensional structures could stabilize all-inorganic perovskites in the black phase. Introducing alternative inorganic substitutes to MA, such as cesium, and large organic cations to form 2D layered structures, are two ways to enhance the environmental stability. However, the performance of 2D layered structured PDs is not as good as their 3D counterparts. Fabricating perovskite heterostructures is now a strategy to balance low-dimensional and 3D perovskites, but it still shows the trade-off between performance and stability. To break this trade-off, more exploration and further research are needed.

## 7. PD Applications Using Low-Dimensional MHPs

### 7.1. Self-Powered PDs

The majority of PDs usually require externally applied voltage to detect incident photons. However, in many application scenarios where an external power source is not easily accessible, self-powered PDs gain the advantage because they can function without external voltage. There are several strategies to achieve self-powered photodetection, and practical high-performance self-powered PDs based on various materials, including low-dimensional MHPs, have been developed.

One commonly used strategy is to fabricate heterostructures or Schottky junctions, in which photogenerated carriers are separated by built-in electric field, and consequently self-powered PDs could be achieved. Generally, the materials chosen to construct heterostructures are supposed to form the required band alignment with perovskites and exhibit excellent properties to facilitate charge transport and extraction. For example, p-type CuI is a promising alternative for organic hole transport materials in solar cells owing to its high hole conductivity and transparency, which could be utilized in PD applications. Zhang et al. fabricated millimeter-sized CsPbBr<sub>3</sub>/CuI p–n heterostructures via a facile solvent-evaporation and immersion process.<sup>[300]</sup> Under light illumination, the devices exhibit excellent self-powered performance, including high photocurrent, on/off ratio of  $1.5 \times 10^3$ , and fast response speed ( $\tau_{\text{rise}} = 0.04$  ms,  $\tau_{\text{decay}} = 2.96$  ms) at zero bias (Figure 13a). Similarly, all-inorganic lead-free Cs<sub>3</sub>Cu<sub>2</sub>I<sub>5</sub>/GaN heterojunctions were reported by Li et al. for UV photodetection, and the devices based on the p–n junction can function without external power supply.<sup>[301]</sup> Because of the sharp absorption edge and surface-charge recombination, the PDs can further achieve spectrum-selective narrowband UV photodetection (Figure 13b,c). Zhang et al. reported a dual-color self-powered PD based on SnO<sub>2</sub> micro- and millimeter wires decorated with CsPbBr<sub>3</sub> particles.<sup>[302]</sup> The fabricated PDs based on the novel n–n junction can operate under both UV and green light illumination at zero bias, because of the different bandgap of the two components and the asymmetric junction barriers between their conduction band (Figure 13d–f). Lim et al. constructed self-powered photodiodes with a vertical geometry based on quasi-2D RP MHP (PEA)<sub>2</sub>(MA)<sub>n-1</sub>Pb<sub>n</sub>I<sub>3n+1</sub>.<sup>[303]</sup> Thanks to the optimized perovskite phase and reduced leakage current, the photodiodes show high  $R$  of 0.28 A W<sup>-1</sup> for the perovskite with  $n = 10$  and  $\approx 0.5$  A W<sup>-1</sup> for  $40 < n < \infty$  at zero bias, which is among the highest values of self-powered photodiodes. Furthermore, the idea of fabricating self-powered perovskite PDs based on Schottky junctions is equally important, and many Schottky junction PDs with asymmetric electrodes have been demonstrated.<sup>[304,305]</sup>

In addition to the fabrication of junctions, self-powered PDs can be achieved by spontaneous polarization of perovskite ferroelectrics due to their unique structural features. Liu et al. achieved self-powered photodetection by ferroelectric polarization of homogeneous 2D RP perovskite (EA)<sub>2</sub>(MA)<sub>2</sub>Pb<sub>3</sub>Br<sub>10</sub> (EA = ethylammonium).<sup>[306]</sup> The structural distortion provides the perovskite with ferroelectric properties (Figure 13g,h) and superior spontaneous polarization of 3.7  $\mu\text{C cm}^{-2}$ . Under illumination, the spontaneous polarization promotes the

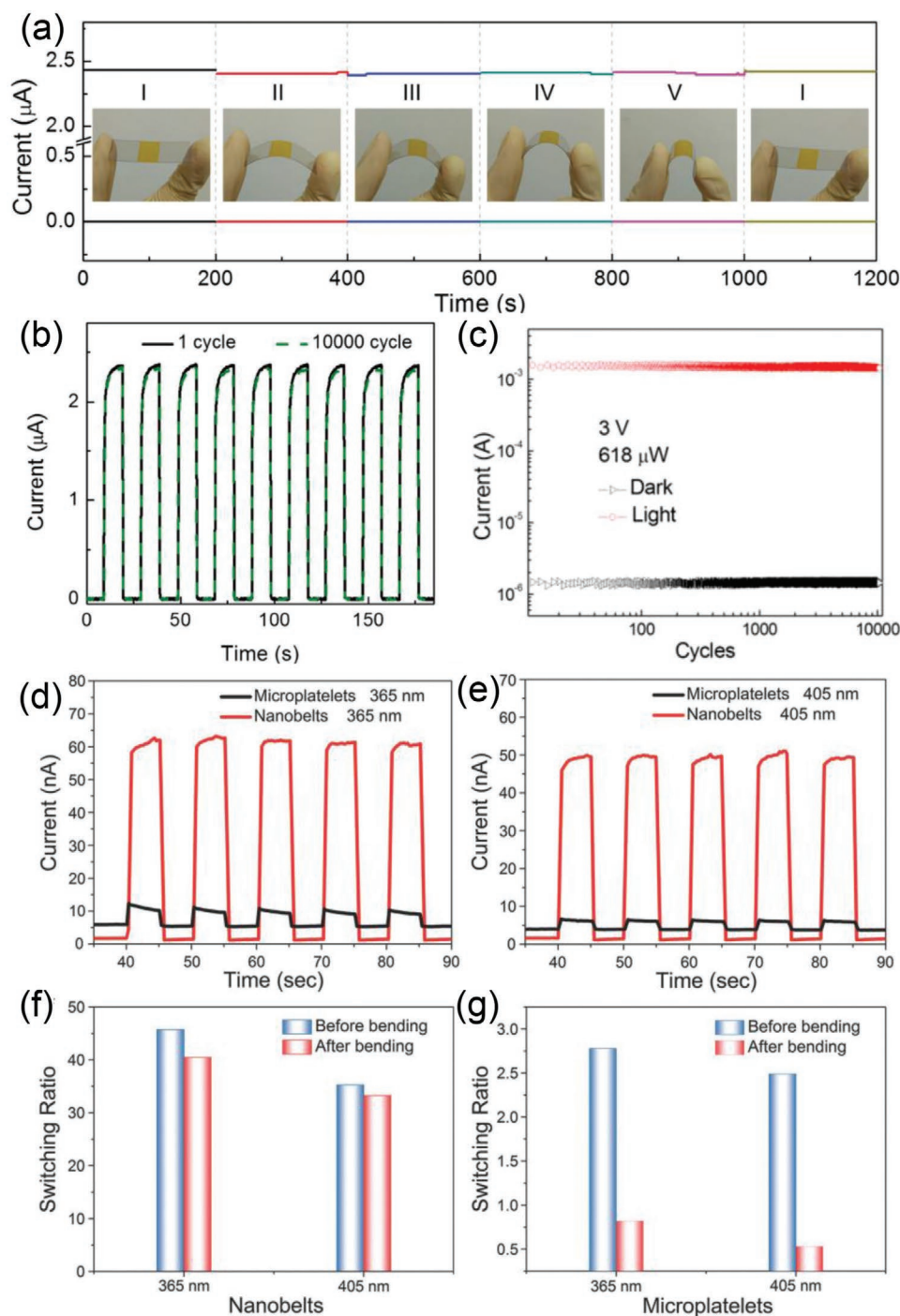


**Figure 12.** a)  $I-t$  curves of the flexible CsPbBr<sub>3</sub> NS PDs when bent at different curvatures under a bias voltage of 5 V. The insets show the corresponding photographs of the device under different bending states. b) Photoresponse at 5 V bias of the CsPbBr<sub>3</sub> NS PDs for the 1st and 10 000th bending-recovery cycle. a,b) Reproduced with permission.<sup>[24]</sup> Copyright 2016, Wiley-VCH. c) Photocurrent and dark current of CsPbBr<sub>3</sub> NS/CNT flexible PDs after more than 10 000 cycles under 3 V bias with 442 nm light illumination (618  $\mu$ W). Reproduced with permission.<sup>[35]</sup> Copyright 2017, American Chemical Society. d,e)  $I-t$  curves of a (C<sub>4</sub>H<sub>9</sub>NH<sub>3</sub>)<sub>2</sub>PbBr<sub>4</sub> nanobelt-based PD and a microplatelet-based PD after 1000 bending-recovery cycles at 5 V bias under 365 and 405 nm light illumination, respectively. f,g) Comparison of the switching ratio of MHP nanobelt-based PDs and MHP microplatelet-based PDs before and after 1000 bending-recovery cycles. d–g) Reproduced with permission.<sup>[224]</sup> Copyright 2017, Wiley-VCH.

separation of photogenerated carriers inside itself, leading to a high on/off ratio of  $>10^6$  and ultrafast response speed ( $\tau_{\text{rise}} = 96 \mu\text{s}$ ,  $\tau_{\text{decay}} = 123 \mu\text{s}$ ) at zero bias. Later, Wang et al.

expanded the response range of self-powered ferroelectric perovskite PDs to the visible-blind UV range by developing the wide-bandgap ( $\approx 3.39 \text{ eV}$ ) 2D layered MHP EA<sub>4</sub>Pb<sub>3</sub>Cl<sub>10</sub>.<sup>[307]</sup> The

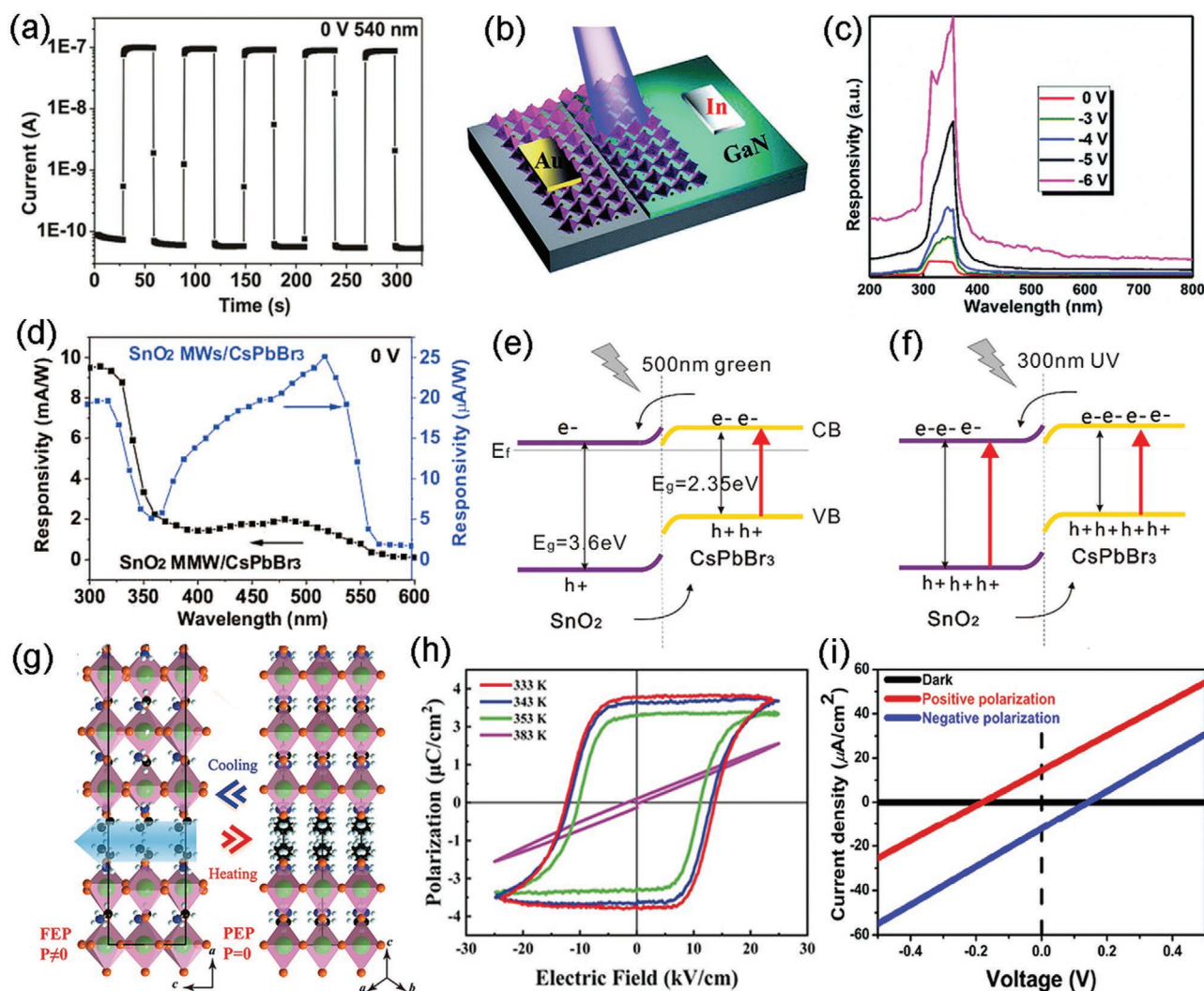


**Figure 13.** a)  $I-t$  characteristics of self-powered  $\text{CsPbBr}_3/\text{CuI}$  PDs under 540 nm on/off cycles at zero bias. Reproduced with permission.<sup>[300]</sup> Copyright 2019, American Chemical Society. b) Schematic illustration and c) response spectra of a  $\text{Cs}_3\text{Cu}_2\text{I}_5/\text{GaN}$  self-powered PD at different bias voltages. b, c) Reproduced with permission.<sup>[301]</sup> Copyright 2020, Royal Society of Chemistry. d) Response spectra of PDs based on  $\text{CsPbBr}_3$  and a single  $\text{SnO}_2$  millimeter wire (MMW) and  $\text{SnO}_2$  microwires (MWs) at zero bias. Schematic band diagrams of the  $\text{SnO}_2/\text{CsPbBr}_3$  PDs under e) 500 nm and f) 300 nm light, respectively. d–f) Reproduced with permission.<sup>[302]</sup> Copyright 2019, American Chemical Society. g) The illustration of  $(\text{EA})_2(\text{MA})_2\text{Pb}_3\text{Br}_{10}$  crystal structure (part), ferroelectric phase along the [010] direction (left), and paraelectric phase along [110] (right), respectively. h)  $P-E$  hysteresis loops along the  $c$ -axis at different temperatures. g, h) Reproduced with permission.<sup>[306]</sup> Copyright 2019, Wiley-VCH. i) Switchable behaviors of self-powered UV PDs based on 2D  $(\text{EA})_4\text{Pb}_3\text{Cl}_{10}$  with different polarization orientations. Reproduced with permission.<sup>[307]</sup> Copyright 2019, American Chemical Society.

2D MHP  $\text{EA}_4\text{Pb}_3\text{Cl}_{10}$  exhibits the higher spontaneous polarization and higher Curie temperature than  $(\text{EA})_2(\text{MA})_2\text{Pb}_3\text{Br}_{10}$  discussed above. Under UV illumination, a high zero-bias photocurrent of  $18.6 \mu\text{A cm}^{-2}$  was observed for the self-powered PDs based on  $\text{EA}_4\text{Pb}_3\text{Cl}_{10}$  ferroelectrics. By switching the polarization orientation, the photocurrent of the PD could be adjusted accordingly (Figure 13i), showing great potential of low-dimensional perovskite ferroelectrics for self-powered PDs.

## 7.2. PDs for the Optical Communication

IoT system is one of the fastest growing technological revolutions for recent years and the IoT market is expected to grow

over \$2.4 trillion annually by 2027.<sup>[308]</sup> However, today's 4G wireless technology will not be able to support the requirement of internet demands by the enormous number of connections and ensure low latency. The 5G wireless system, which is set to accelerate data up to 100 times faster than 4G technology, will especially help establish and expand the IoT system. Paving the way to 5G, broader bandwidth and high-clarity communications are required. Due to the saturated bandwidth of radio frequency (RF) spectra, optical wireless communication (OWC), including visible light communication (VLC) and UV-based communication, is considered as a potential access option. By increasing the channel bandwidth, the data capacity can be greatly increased with low latency. Moreover, the recent wireless technologies come with high energy consumption, high-frequency



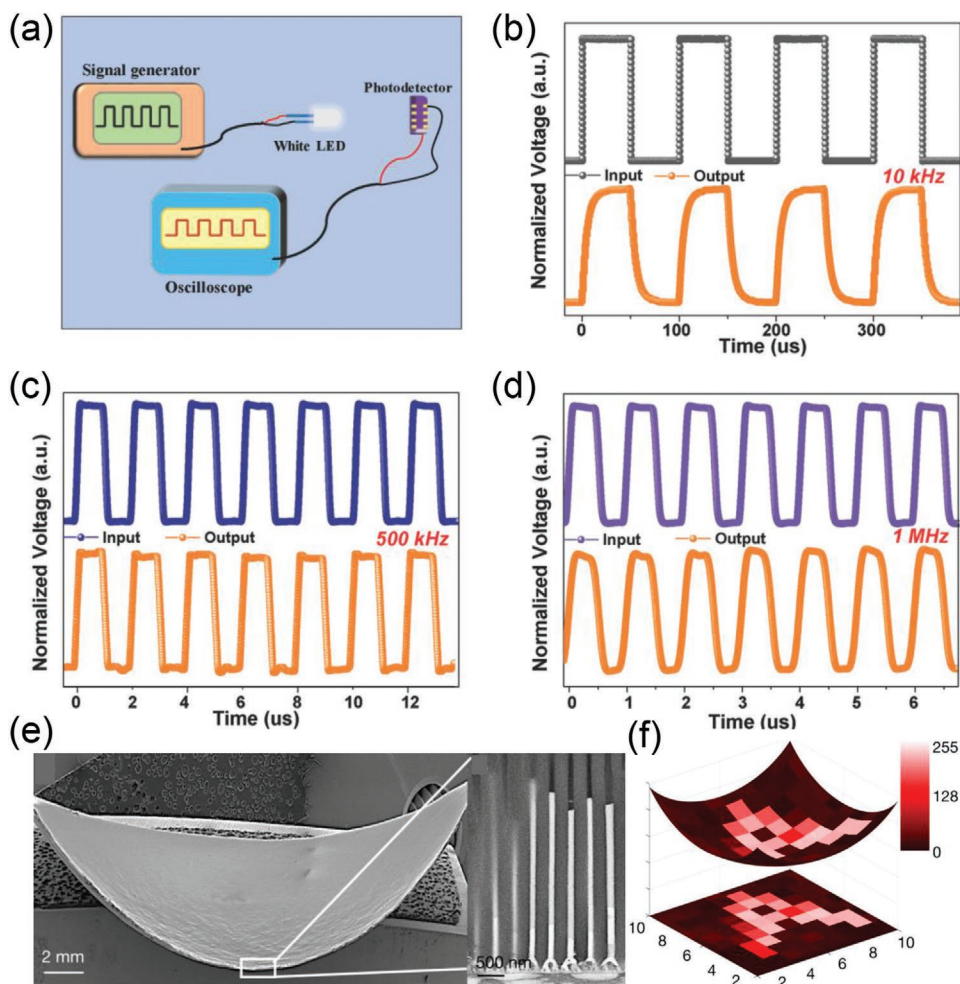


**Figure 14.** a) The schematic diagram of white LED OWC system. The input and output signals for different frequencies: b) 10 kHz, c) 500 kHz, and d) 1 MHz, respectively. a–d) Reproduced with permission.<sup>[310]</sup> Copyright 2019, Wiley-VCH. e) Low-resolution cross-sectional SEM image of the hemispherical porous aluminum oxide membrane/NWs and cross-sectional SEM images of MHP NWs in porous aluminum oxide membrane. f) Image-sensing demonstration. The reconstructed image (letter “A”) of the biomimetic eye and its projection on a flat plane. e,f) Reproduced with permission.<sup>[231]</sup> Copyright 2020, Springer Nature.

radio electromagnetic waves on human body or surrounding electronic machines and security issues. OWC can achieve near-zero energy-consuming communication, anti-interference ability, and anti-interception security information space. The two key components in the OWC system are optical sources and PDs, which are for data transmission and reception. The “on” (“off”) state of the light sources is driven by “1” (“0”) signal in the control command. MHP PDs with high detectivity and fast response speed are attractive for OWC applications.

To investigate the potential of MHP PDs to the OWC, some groups simulated the core optocoupler of an OWC system, which consists of a signal generator, driving a light source (e.g., LED) to turn on and off quickly and an MHP PD connecting to a rapid oscilloscope, as shown in **Figure 14a**.<sup>[120,309–312]</sup> Gao’s group first integrated MHP PDs into an OWC system as an optical signal receiver on transmitting text and audio signals.<sup>[309]</sup> Li et al. demonstrated MAPbI<sub>3</sub> PDs applied in a VLC system.<sup>[310]</sup> The output signals well match the original input signals from low to high frequency at 10 kHz, 500 kHz, and

1 MHz, respectively (Figure 14b–d).<sup>[310]</sup> Further, Liu et al. used the CsPb<sub>2</sub>Br<sub>5</sub>–CsPbBr<sub>3</sub> PD as a self-powered signal receiver in a voice-controlled OWC system, which can control the mechanical, electrical or electronic systems by voice commands.<sup>[311]</sup> The voice commands are coded by the master controller into a sequence of “1” and “0” to control “on” and “off” of the LED. The OWC system can accurately and smoothly execute the 9-bit code in the 0/1 mode by the voice commands to open/close light, doors, and fans, showing the potential applications in the smart home market. Moreover, MHP with strong absorption in the UV region, such as CsPbBr<sub>3</sub> can help with UV-based communication. Kang et al. reported a hybrid CsPbBr<sub>3</sub>–Si PD for UV communication.<sup>[312]</sup> By incorporating CsPbBr<sub>3</sub> NCs as a downconverting layer, a nearly threefold improvement in *R* and 25% enhancement in EQE of the solar-blind UV region compared to pure Si PDs were demonstrated. A high data rate of up to 34 Mbps in solar-blind UV communication was achieved. These results demonstrate the feasibility of practical PD applications combined with OWC.

### 7.3. PDs for the Biomimetic Eyes

Biomimetic eye is highly desirable in robotics and visual prostheses. The spherical-shape retina is required to accurately translate visual signals into electrical neural impulses and then to our brain, which is like an image sensor. However, commercial image sensors made by CCD and CMOS are mainly planar due to their planar microfabrication processes. Fan's group built a hemispherical retina made by high-density MHP NW PD arrays, mimicking the photoreceptors on a human retina.<sup>[231]</sup> The biomimetic retina is made with a porous aluminum oxide membrane, which serves as a round casing, filled with perovskites as wired photosensors (Figure 14e). MHP NW PDs detect light and send the signal through liquid-metal wires to external image-processing electronics. The artificial eye is able to image-sensing and detect a range of light intensities, which has a high degree of similarity to that of a human eye (Figure 14f).

## 8. Conclusions and Outlook

With the demand for high-performance, miniaturized, and flexible optoelectronic devices increasing, there has been a burgeoning interest in low-dimensional MHPs nowadays because of the outstanding properties inherited from bulk perovskites and their reduced dimensionality. In this review, we summarized recent advances in synthesis, investigation of the optical and optoelectronic properties, as well as performance, stability, and applications of PDs based on low-dimensional MHPs. Various synthesis strategies, as the necessary prerequisite to the study of material properties and device performance, offer exciting possibilities for the preparation of low-dimensional MHPs. The synthesis strategies are classified into solution-based synthesis and vapor-phase approaches. With the participation of selected solvents and ligands, solution synthesis is suitable for the preparation of different colloidal MHP nanostructures, from 0D QDs to 2D NSs, through either bottom-up or top-down approaches. By contrast, vapor-phase approaches produce low-dimensional MHPs, especially 1D and 2D ones, with relatively higher crystalline quality and lower defect density. The development of novel synthesis methods and the modification of existing techniques have been promoting the preparation of high-quality low-dimensional MHPs for diverse PD applications.

Research on low-dimensional MHPs with various dimensionalities has already revealed many of their common features and distinct properties. Similar to their bulk counterparts, low-dimensional MHPs have a number of intriguing properties such as high and tunable light absorption, long carrier diffusion length, high quantum efficiency, ambipolar carrier transport, and nonlinear optical properties, while some of them have unique advantages over bulk perovskites including higher PLQY, fewer defects, and higher environmental stability. Among them, 0D MHPs have high light-harvesting capability and high PLQY. Well-aligned 1D MHPs exhibit large carrier mobilities and long carrier diffusion lengths owing to their conductive channels and fewer barriers, and they can serve as polarization-sensitive PDs because of the anisotropic

geometry. 2D MHP nanostructures show outstanding in-plane carrier transport, while 2D layered MHPs show better stability and layer thickness-dependent properties due to their unique structure consisting of quantum wells. The unique edge states of 2D layered MHPs can facilitate the carrier generation and transport, improving the carrier concentration, lifetime, and mobility. The mechanical properties of low-dimensional MHPs are considered better than those of bulk or polycrystalline MHPs, showing the potential for flexible and wearable devices.

Despite the above-mentioned advantages, some problems arise in terms of the PD applications of low-dimensional MHPs. For instance, with the crystal size or layer thickness decreasing, the high  $E_b$  hinders the generation of free carriers in PD devices. Long-chain organic molecules outside MHP nanostructures and between 2D MHP layers, which are widely used to direct the crystal growth, passivate surface defects, and improve the stability of low-dimensional MHPs, undoubtedly limit the charge transport. In order to tackle the problems, much effort has been made to optimize the properties and improve device performance. Strategies for changing, decreasing, or removing organic ligands could improve the exciton dissociation efficiency and increase the carrier transport between nanostructures without lowering their stability. It is also possible to improve carrier transport and to lower the  $E_b$  and  $n_{traps}$  by increasing the crystal size to some extent. Controlling the crystalline orientation in 2D layered MHP-based devices is useful to tackle the issue of out-of-plane carrier transport. Besides, the effective control of doping atoms, vacancies, chemical composition, and crystal size of low-dimensional MHPs makes bandgap engineering a highly efficient way to adjust their properties. By changing the A-site cations, the crystal structure, layer thickness, and bandgap could be tuned accordingly. In addition, utilizing mixed-dimensional MHPs or fabricating heterostructures is expected to enhance light absorption and carrier separation, and even achieve self-powered PD devices. The device configuration is equally important to meet certain needs.

Though recent years have seen rapid progress in the development of low-dimensional MHPs, there are still several issues that need to be addressed in the future. Despite their superior stability than that of 3D ones, more work should be done to further improve the phase and environmental stability against factors including moisture, oxygen, light, heat, stress, and bias. Besides, the toxic Pb widely used in high-performance MHPs poses a threat to the environment, and therefore it is imperative to improve the device performance and stability of PDs based on lead-free MHPs, such as Sn-, Ge-, Sb-, and Bi-based MHPs. In terms of the synthesis methods, although MHPs are famous for their facile preparation and rich morphology, the growth kinetics underlying the growth processes need to be more carefully investigated to produce high-quality low-dimensional MHPs with various and precisely controlled morphologies. Machine learning combined with high-throughput experimentation will accelerate the discovery and development of new MHPs and might free researchers from trial and error.<sup>[313]</sup> Mass-production methods of low-dimensional MHPs for large-scale industrial purposes are also needed. For example, the quality, cost, reliability, and stability of metal contacts in PD devices must be more carefully investigated to ensure efficient

charge transport and achieve better device performance.<sup>[314]</sup> The possible damages to vulnerable MHPs caused by nanofabrication processes, such as solvent processing and lithography, should be further reduced to prevent device degradation in mass production.<sup>[315,316]</sup> As for device performance, many low-dimensional MHP-based PD devices are still facing the trade-offs between, for example, light-harvesting and transparency, stability and performance, and cost and efficiency. While sometimes a compromise has to be reached to meet certain needs, we are confident the fast progress in low-dimensional MHPs will create more win-wins from trade-offs in the future.

## Acknowledgements

H.-P.W. and S.Y.L. contributed equally to this work. H.-P.W. and J.-H.H. acknowledge the financial support from City University of Hong Kong. X.S.F. acknowledges the support from the National Key R&D Program of China (2017YFA0204600), the National Natural Science Foundation of China (51872050), and the Science and Technology Commission of Shanghai Municipality (Nos. 19520744300, 18520710800, and 18520744600).

## Conflict of Interest

The authors declare no conflict of interest.

## Keywords

bandgap engineering, carrier transport, low-dimensional perovskites, photodetectors, stability

Received: May 14, 2020

Revised: July 21, 2020

Published online: December 21, 2020

- [1] G. Konstantatos, E. H. Sargent, *Nat. Nanotechnol.* **2010**, *5*, 391.
- [2] G. Konstantatos, J. Clifford, L. Levina, E. H. Sargent, *Nat. Photonics* **2007**, *1*, 531.
- [3] F. P. García de Arquer, A. Armin, P. Meredith, E. H. Sargent, *Nat. Rev. Mater.* **2017**, *2*, 16100.
- [4] A. M. Al-Amri, B. Cheng, J.-H. He, *IEEE Trans. Nanotechnol.* **2019**, *18*, 1.
- [5] M.-W. Chen, J. R. D. Retamal, C.-Y. Chen, J.-H. He, *IEEE Electron Device Lett.* **2012**, *33*, 411.
- [6] H. Wang, D. H. Kim, *Chem. Soc. Rev.* **2017**, *46*, 5204.
- [7] G. Yan, B. Jiang, Y. Yuan, M. Kuang, X. Liu, Z. Zeng, C. Zhao, J.-H. He, W. Mai, *ACS Appl. Mater. Interfaces* **2020**, *12*, 6064.
- [8] U. Chang, J. T. Lee, J.-M. Yun, B. Lee, S. W. Lee, H.-I. Joh, K. Eom, T. F. Fuller, *ACS Nano* **2018**, *13*, 1490.
- [9] D. Periyangounder, T. Wei, T. Li, C. Lin, T. P. Gonçalves, H. Fu, D. Tsai, J. Ke, H. Kuo, K. Huang, N. Lu, X. Fang, J. He, *Adv. Mater.* **2020**, *32*, 1904634.
- [10] W. Peng, L. Wang, B. Murali, K.-T. Ho, A. Bera, N. Cho, C.-F. Kang, V. M. Burlakov, J. Pan, L. Sinatra, C. Ma, W. Xu, D. Shi, E. Alarousu, A. Goriely, J.-H. He, O. F. Mohammed, T. Wu, O. M. Bakr, *Adv. Mater.* **2016**, *28*, 3383.
- [11] W. Peng, J. Yin, K.-T. Ho, O. Ouellette, M. De Bastiani, B. Murali, O. El Tall, C. Shen, X. Miao, J. Pan, E. Alarousu, J.-H. He, B. S. Ooi, O. F. Mohammed, E. Sargent, O. M. Bakr, *Nano Lett.* **2017**, *17*, 4759.
- [12] T.-C. Wei, H.-P. Wang, T.-Y. Li, C.-H. Lin, Y.-H. Hsieh, Y.-H. Chu, J.-H. He, *Adv. Mater.* **2017**, *29*, 1701789.
- [13] T.-C. Wei, S. Mokkapatil, T.-Y. Li, C.-H. Lin, G.-R. Lin, C. Jagadish, J.-H. He, *Adv. Funct. Mater.* **2018**, *28*, 1707175.
- [14] B. Cheng, T.-Y. Li, P. Maity, P.-C. Wei, D. Nordlund, K.-T. Ho, D.-H. Lien, C.-H. Lin, R.-Z. Liang, X. Miao, I. A. Ajia, J. Yin, D. Sokaras, A. Javey, I. S. Roqan, O. F. Mohammed, J.-H. He, *Commun. Phys.* **2018**, *1*, 80.
- [15] S. De Wolf, J. Holovsky, S.-J. Moon, P. Löper, B. Niesen, M. Ledinsky, F.-J. Haug, J.-H. Yum, C. Ballif, *J. Phys. Chem. Lett.* **2014**, *5*, 1035.
- [16] D. Venkateshvaran, M. Nikolka, A. Sadhanala, V. Lemaire, M. Zelazny, M. Kepa, M. Hurhangee, A. J. Kronemeijer, V. Pecunia, I. Nasrallah, I. Romanov, K. Broch, I. McCulloch, D. Emin, Y. Olivier, J. Cornil, D. Beljonne, H. Sirringhaus, *Nature* **2014**, *515*, 384.
- [17] P. Wangyang, C. Gong, G. Rao, K. Hu, X. Wang, C. Yan, L. Dai, C. Wu, J. Xiong, *Adv. Opt. Mater.* **2018**, *6*, 1701302.
- [18] D. Zhang, C. Liu, K. Li, W. Guo, F. Gao, J. Zhou, X. Zhang, S. Ruan, *Adv. Opt. Mater.* **2018**, *6*, 1701189.
- [19] W. Nie, H. Tsai, R. Asadpour, J.-C. Blancon, A. J. Neukirch, G. Gupta, J. J. Crochet, M. Chhowalla, S. Tretiak, M. A. Alam, H.-L. Wang, A. D. Mohite, *Science* **2015**, *347*, 522.
- [20] H.-P. Wang, C. M. Sutter-Fella, P. Lobaccaro, M. Hettick, M. Zheng, D.-H. Lien, D. W. Miller, C. W. Warren, E. T. Roe, M. C. Lonergan, H. L. Guthrey, N. M. Haegel, J. W. Ager, C. Carraro, R. Maboudian, J.-H. He, A. Javey, *Chem. Mater.* **2016**, *28*, 4602.
- [21] C. C. Boyd, R. Checharoen, T. Leijten, M. D. McGehee, *Chem. Rev.* **2019**, *119*, 3418.
- [22] Q. Dong, Y. Fang, Y. Shao, P. Mulligan, J. Qiu, L. Cao, J. Huang, *Science* **2015**, *347*, 967.
- [23] D. W. de Quilletes, S. M. Vorpahl, S. D. Stranks, H. Nagaoka, G. E. Eperon, M. E. Ziffer, H. J. Snaith, D. S. Ginger, *Science* **2015**, *348*, 683.
- [24] Z. Liu, L. You, N. Faraji, C.-H. Lin, X. Xu, J.-H. He, J. Seidel, J. Wang, H. N. Alshareef, T. Wu, *Adv. Funct. Mater.* **2020**, *30*, 1909672.
- [25] B. Cheng, T.-Y. Li, P.-C. Wei, J. Yin, K.-T. Ho, J. R. D. Retamal, O. F. Mohammed, J.-H. He, *Nat. Commun.* **2018**, *9*, 5196.
- [26] J. Yin, P. Maity, R. Naphade, B. Cheng, J.-H. He, O. M. Bakr, J.-L. Brédas, O. F. Mohammed, *ACS Nano* **2019**, *13*, 12621.
- [27] C. Kang, C. Lin, C. Lin, T. Li, S. Huang Chen, C. Tsai, C. Sher, T. Wu, P. Lee, X. Xu, M. Zhang, C. Ho, J. He, H. Kuo, *Adv. Sci.* **2019**, *6*, 1902230.
- [28] P. Maity, J. Yin, B. Cheng, J.-H. He, O. M. Bakr, O. F. Mohammed, *J. Phys. Chem. Lett.* **2019**, *10*, 5259.
- [29] A. M. Alamri, S. Leung, M. Vaseem, A. Shamim, J.-H. He, *IEEE Trans. Electron Devices* **2019**, *66*, 2657.
- [30] K.-T. Ho, S.-F. Leung, T.-Y. Li, P. Maity, B. Cheng, H.-C. Fu, O. F. Mohammed, J.-H. He, *Adv. Mater.* **2018**, *30*, 1804372.
- [31] J. Feng, C. Gong, H. Gao, W. Wen, Y. Gong, X. Jiang, B. Zhang, Y. Wu, Y. Wu, H. Fu, L. Jiang, X. Zhang, *Nat. Electron.* **2018**, *1*, 404.
- [32] W. Deng, X. Zhang, L. Huang, X. Xu, L. Wang, J. Wang, Q. Shang, S.-T. Lee, J. Jie, *Adv. Mater.* **2016**, *28*, 2201.
- [33] H. Deng, X. Yang, D. Dong, B. Li, D. Yang, S. Yuan, K. Qiao, Y.-B. Cheng, J. Tang, H. Song, *Nano Lett.* **2015**, *15*, 7963.
- [34] S. Han, P. Wang, J. Zhang, X. Liu, Z. Sun, X. Huang, L. Li, C. Ji, W. Zhang, B. Teng, W. Hu, M. Hong, J. Luo, *Laser Photonics Rev.* **2018**, *12*, 1800060.
- [35] X. Li, D. Yu, J. Chen, Y. Wang, F. Cao, Y. Wei, Y. Wu, L. Wang, Y. Zhu, Z. Sun, J. Ji, Y. Shen, H. Sun, H. Zeng, *ACS Nano* **2017**, *11*, 2015.
- [36] L. Gao, K. Zeng, J. Guo, C. Ge, J. Du, Y. Zhao, C. Chen, H. Deng, Y. He, H. Song, G. Niu, J. Tang, *Nano Lett.* **2016**, *16*, 7446.

- [37] J. Li, J. Wang, J. Ma, H. Shen, L. Li, X. Duan, D. Li, *Nat. Commun.* **2019**, *10*, 806.
- [38] J. Wang, C. Fang, J. Ma, S. Wang, L. Jin, W. Li, D. Li, *ACS Nano* **2019**, *13*, 9473.
- [39] L. Wang, Y. Xue, M. Cui, Y. Huang, H. Xu, C. Qin, J. Yang, H. Dai, M. Yuan, *Angew. Chem., Int. Ed.* **2020**, *59*, 6442.
- [40] S.-F. Leung, K.-T. Ho, P.-K. Kung, V. K. S. Hsiao, H. N. Alshareef, Z. L. Wang, J.-H. He, *Adv. Mater.* **2018**, *30*, 1704611.
- [41] W. Ouyang, L. Su, X. Fang, *Small* **2018**, *14*, 1801611.
- [42] Q. Li, J. van de Groep, Y. Wang, P. G. Kik, M. L. Brongersma, *Nat. Commun.* **2019**, *10*, 4982.
- [43] S. Li, Y. Zhang, W. Yang, H. Liu, X. Fang, *Adv. Mater.* **2020**, *32*, 1905443.
- [44] H. Chen, H. Liu, Z. Zhang, K. Hu, X. Fang, *Adv. Mater.* **2016**, *28*, 403.
- [45] Y. Fang, Q. Dong, Y. Shao, Y. Yuan, J. Huang, *Nat. Photonics* **2015**, *9*, 679.
- [46] M.-L. Lu, T.-M. Weng, J.-Y. Chen, Y.-F. Chen, *NPG Asia Mater.* **2012**, *4*, e26.
- [47] M. Razeghi, A. Rogalski, *J. Appl. Phys.* **1996**, *79*, 7433.
- [48] S. Liu, Z. Wei, Y. Cao, L. Gan, Z. Wang, W. Xu, X. Guo, D. Zhu, *Chem. Sci.* **2011**, *2*, 796.
- [49] K. Hu, F. Teng, L. Zheng, P. Yu, Z. Zhang, H. Chen, X. Fang, *Laser Photonics Rev.* **2017**, *11*, 1600257.
- [50] L. C. Schmidt, A. Pertegás, S. González-Carrero, O. Malinkiewicz, S. Agouram, G. Mínguez Espallargas, H. J. Bolink, R. E. Galian, J. Pérez-Prieto, *J. Am. Chem. Soc.* **2014**, *136*, 850.
- [51] F. Zhang, H. Zhong, C. Chen, X. Wu, X. Hu, H. Huang, J. Han, B. Zou, Y. Dong, *ACS Nano* **2015**, *9*, 4533.
- [52] L. Protesescu, S. Yakunin, M. I. Bodnarchuk, F. Krieg, R. Caputo, C. H. Hendon, R. X. Yang, A. Walsh, M. V. Kovalenko, *Nano Lett.* **2015**, *15*, 3692.
- [53] D. Chen, X. Chen, *J. Mater. Chem. C* **2019**, *7*, 1413.
- [54] J. Shamsi, A. S. Urban, M. Imran, L. De Trizio, L. Manna, *Chem. Rev.* **2019**, *119*, 3296.
- [55] D. Han, M. Imran, M. Zhang, S. Chang, X. Wu, X. Zhang, J. Tang, M. Wang, S. Ali, X. Li, G. Yu, J. Han, L. Wang, B. Zou, H. Zhong, *ACS Nano* **2018**, *12*, 8808.
- [56] H. Huang, F. Zhao, L. Liu, F. Zhang, X. Wu, L. Shi, B. Zou, Q. Pei, H. Zhong, *ACS Appl. Mater. Interfaces* **2015**, *7*, 28128.
- [57] Y. Tong, E. Bladt, M. F. Aygüler, A. Manzi, K. Z. Milowska, V. A. Hintermayr, P. Docampo, S. Bals, A. S. Urban, L. Polavarapu, J. Feldmann, *Angew. Chem., Int. Ed.* **2016**, *55*, 13887.
- [58] M. Chen, Y. Zou, L. Wu, Q. Pan, D. Yang, H. Hu, Y. Tan, Q. Zhong, Y. Xu, H. Liu, B. Sun, Q. Zhang, *Adv. Funct. Mater.* **2017**, *27*, 1701121.
- [59] D. N. Dirin, L. Protesescu, D. Trummer, I. V. Kochetygov, S. Yakunin, F. Krumeich, N. P. Stadie, M. V. Kovalenko, *Nano Lett.* **2016**, *16*, 5866.
- [60] Y. Wei, K. Li, Z. Cheng, M. Liu, H. Xiao, P. Dang, S. Liang, Z. Wu, H. Lian, J. Lin, *Adv. Mater.* **2019**, *31*, 1807592.
- [61] H. Huang, Q. Xue, B. Chen, Y. Xiong, J. Schneider, C. Zhi, H. Zhong, A. L. Rogach, *Angew. Chem., Int. Ed.* **2017**, *56*, 9571.
- [62] J. Liu, K. Song, Y. Shin, X. Liu, J. Chen, K. X. Yao, J. Pan, C. Yang, J. Yin, L.-J. Xu, H. Yang, A. M. El-Zohry, B. Xin, S. Mitra, M. N. Hedhili, I. S. Roqan, O. F. Mohammed, Y. Han, O. M. Bakr, *Chem. Mater.* **2019**, *31*, 6642.
- [63] D. Zhang, S. W. Eaton, Y. Yu, L. Dou, P. Yang, *J. Am. Chem. Soc.* **2015**, *137*, 9230.
- [64] Z. Du, D. Fu, J. Teng, L. Wang, F. Gao, W. Yang, H. Zhang, X. Fang, *Small* **2019**, *15*, 1905253.
- [65] E. Horváth, M. Spina, Z. Szekeřnyes, K. Kamarás, R. Gaal, D. Gachet, L. Forró, *Nano Lett.* **2014**, *14*, 6761.
- [66] S. Z. Oener, P. Khoram, S. Brittman, S. A. Mann, Q. Zhang, Z. Fan, S. W. Boettcher, E. C. Garnett, *Nano Lett.* **2017**, *17*, 6557.
- [67] Q. Zhou, J. G. Park, R. Nie, A. K. Thokchom, D. Ha, J. Pan, S. Il Seok, T. Kim, *ACS Nano* **2018**, *12*, 8406.
- [68] P.-C. Tsai, J.-Y. Chen, E. Ercan, C.-C. Chueh, S.-H. Tung, W.-C. Chen, *Small* **2018**, *14*, 1704379.
- [69] M. Chen, J. Yang, Z. Wang, Z. Xu, H. Lee, H. Lee, Z. Zhou, S. Feng, S. Lee, J. Pyo, S. K. Seol, D. Ki, J. T. Kim, *Adv. Mater.* **2019**, *31*, 1904073.
- [70] H. Tsai, W. Nie, J.-C. Blancon, C. C. Stoumpos, R. Asadpour, B. Harutyunyan, A. J. Neukirch, R. Verduzco, J. J. Crochet, S. Tretiak, L. Pedesseau, J. Even, M. A. Alam, G. Gupta, J. Lou, P. M. Ajayan, M. J. Bedzyk, M. G. Kanatzidis, A. D. Mohite, *Nature* **2016**, *536*, 312.
- [71] L. Dou, A. B. Wong, Y. Yu, M. Lai, N. Kornienko, S. W. Eaton, A. Fu, C. G. Bischak, J. Ma, T. Ding, N. S. Ginsberg, L.-W. Wang, A. P. Alivisatos, P. Yang, *Science* **2015**, *349*, 1518.
- [72] W. Zheng, X. Xiong, R. Lin, Z. Zhang, C. Xu, F. Huang, *ACS Appl. Mater. Interfaces* **2018**, *10*, 1865.
- [73] Q. Zhang, L. Chu, F. Zhou, W. Ji, G. Eda, *Adv. Mater.* **2018**, *30*, 1704055.
- [74] S. Yang, W. Niu, A.-L. Wang, Z. Fan, B. Chen, C. Tan, Q. Lu, H. Zhang, *Angew. Chem., Int. Ed.* **2017**, *56*, 4252.
- [75] J. Chen, L. Gan, F. Zhuge, H. Li, J. Song, H. Zeng, T. Zhai, *Angew. Chem., Int. Ed.* **2017**, *56*, 2390.
- [76] H. Tian, L. Zhao, X. Wang, Y.-W. Yeh, N. Yao, B. P. Rand, T.-L. Ren, *ACS Nano* **2017**, *11*, 12247.
- [77] J. Li, J. Wang, Y. Zhang, H. Wang, G. Lin, X. Xiong, W. Zhou, H. Luo, D. Li, *2D Mater.* **2018**, *5*, 021001.
- [78] E. Shi, S. Deng, B. Yuan, Y. Gao, Akriti, L. Yuan, C. S. Davis, D. Zemlyanov, Y. Yu, L. Huang, L. Dou, *ACS Nano* **2019**, *13*, 1635.
- [79] V. A. Hintermayr, A. F. Richter, F. Ehrat, M. Döblinger, W. Vanderlinden, J. A. Sichert, Y. Tong, L. Polavarapu, J. Feldmann, A. S. Urban, *Adv. Mater.* **2016**, *28*, 9478.
- [80] M. Xie, H. Liu, F. Chun, W. Deng, C. Luo, Z. Zhu, M. Yang, Y. Li, W. Li, W. Yan, W. Yang, *Small* **2019**, *15*, 1901994.
- [81] M. C. Weidman, A. J. Goodman, W. A. Tisdale, *Chem. Mater.* **2017**, *29*, 5019.
- [82] M. B. Teunis, M. A. Johnson, B. B. Muhoberac, S. Seifert, R. Sardar, *Chem. Mater.* **2017**, *29*, 3526.
- [83] E. Klein, A. Black, Ö. Tokmak, C. Strelow, R. Lesyuk, C. Klinke, *ACS Nano* **2019**, *13*, 6955.
- [84] Z. Liang, S. Zhao, Z. Xu, B. Qiao, P. Song, D. Gao, X. Xu, *ACS Appl. Mater. Interfaces* **2016**, *8*, 28824.
- [85] P. Gui, H. Zhou, F. Yao, Z. Song, B. Li, G. Fang, *Small* **2019**, *15*, 1902618.
- [86] Y. Tong, F. Ehrat, W. Vanderlinden, C. Cardenas-Daw, J. K. Stolarczyk, L. Polavarapu, A. S. Urban, *ACS Nano* **2016**, *10*, 10936.
- [87] J. Chen, Y. Fu, L. Samad, L. Dang, Y. Zhao, S. Shen, L. Guo, S. Jin, *Nano Lett.* **2017**, *17*, 460.
- [88] K. Hong, Q. Van Le, S. Y. Kim, H. W. Jang, *J. Mater. Chem. C* **2018**, *6*, 2189.
- [89] Z. Liu, Q. Shang, C. Li, L. Zhao, Y. Gao, Q. Li, J. Chen, S. Zhang, X. Liu, Y. Fu, Q. Zhang, *Appl. Phys. Lett.* **2019**, *114*, 101902.
- [90] A. Waleed, M. M. Tavakoli, L. Gu, S. Hussain, D. Zhang, S. Poddar, Z. Wang, R. Zhang, Z. Fan, *Nano Lett.* **2017**, *17*, 4951.
- [91] Y. Wang, X. Sun, R. Shivanna, Y. Yang, Z. Chen, Y. Guo, G.-C. Wang, E. Wertz, F. Deschler, Z. Cai, H. Zhou, T.-M. Lu, J. Shi, *Nano Lett.* **2016**, *16*, 7974.
- [92] Z. Wu, J. Chen, Y. Mi, X. Sui, S. Zhang, W. Du, R. Wang, J. Shi, X. Wu, X. Qiu, Z. Qin, Q. Zhang, X. Liu, *Adv. Opt. Mater.* **2018**, *6*, 1800674.
- [93] M. Han, J. Sun, M. Peng, N. Han, Z. Chen, D. Liu, Y. Guo, S. Zhao, C. Shan, T. Xu, X. Hao, W. Hu, Z. Yang, *J. Phys. Chem. C* **2019**, *123*, 17566.
- [94] S. T. Ha, X. Liu, Q. Zhang, D. Giovanni, T. C. Sum, Q. Xiong, *Adv. Opt. Mater.* **2014**, *2*, 838.

- [95] J. Liu, Y. Xue, Z. Wang, Z.-Q. Xu, C. Zheng, B. Weber, J. Song, Y. Wang, Y. Lu, Y. Zhang, Q. Bao, *ACS Nano* **2016**, *10*, 3536.
- [96] G. Wang, D. Li, H.-C. Cheng, Y. Li, C.-Y. Chen, A. Yin, Z. Zhao, Z. Lin, H. Wu, Q. He, M. Ding, Y. Liu, Y. Huang, X. Duan, *Sci. Adv.* **2015**, *1*, e1500613.
- [97] X. Hu, H. Zhou, Z. Jiang, X. Wang, S. Yuan, J. Lan, Y. Fu, X. Zhang, W. Zheng, X. Wang, X. Zhu, L. Liao, G. Xu, S. Jin, A. Pan, *ACS Nano* **2017**, *11*, 9869.
- [98] C. Huo, X. Liu, X. Song, Z. Wang, H. Zeng, *J. Phys. Chem. Lett.* **2017**, *8*, 4785.
- [99] J. Chen, D. J. Morrow, Y. Fu, W. Zheng, Y. Zhao, L. Dang, M. J. Stolt, D. D. Kohler, X. Wang, K. J. Czech, M. P. Hautzinger, S. Shen, L. Guo, A. Pan, J. C. Wright, S. Jin, *J. Am. Chem. Soc.* **2017**, *139*, 13525.
- [100] C. Huo, X. Liu, Z. Wang, X. Song, H. Zeng, *Adv. Opt. Mater.* **2018**, *6*, 1800152.
- [101] Z. Tan, Y. Wu, H. Hong, J. Yin, J. Zhang, L. Lin, M. Wang, X. Sun, L. Sun, Y. Huang, K. Liu, Z. Liu, H. Peng, *J. Am. Chem. Soc.* **2016**, *138*, 16612.
- [102] W. Li, J. Zheng, B. Hu, H.-C. Fu, M. Hu, A. Veyssal, Y. Zhao, J.-H. He, T. L. Liu, A. Ho-Baillie, S. Jin, *Nat. Mater.* **2020**, <https://doi.org/10.1038/s41563-020-0720-x>.
- [103] S. K. Karuturi, H. Shen, A. Sharma, F. J. Beck, P. Varadhan, T. Duong, P. R. Narangari, D. Zhang, Y. Wan, J.-H. He, H. H. Tan, C. Jagadish, K. Catchpole, *Adv. Energy Mater.* **2020**, *10*, 2000772.
- [104] L. Dou, Y. (Micheal) Yang, J. You, Z. Hong, W.-H. Chang, G. Li, Y. Yang, *Nat. Commun.* **2014**, *5*, 5404.
- [105] M. Ahmadi, T. Wu, B. Hu, *Adv. Mater.* **2017**, *29*, 1605242.
- [106] X. Qi, Y. Zhang, Q. Ou, S. T. Ha, C.-W. Qiu, H. Zhang, Y.-B. Cheng, Q. Xiong, Q. Bao, *Small* **2018**, *14*, 1800682.
- [107] Z. Yang, Y. Deng, X. Zhang, S. Wang, H. Chen, S. Yang, J. Khurgin, N. X. Fang, X. Zhang, R. Ma, *Adv. Mater.* **2018**, *30*, 1704333.
- [108] H. C. Woo, J. W. Choi, J. Shin, S.-H. Chin, M. H. Ann, C.-L. Lee, *J. Phys. Chem. Lett.* **2018**, *9*, 4066.
- [109] Y. Jiang, X. Wang, A. Pan, *Adv. Mater.* **2019**, *31*, 1806671.
- [110] I. B. Koutselas, L. Ducasse, G. C. Papavassiliou, *J. Phys.: Condens. Matter* **1996**, *8*, 5953.
- [111] V. D'Innocenzo, G. Grancini, M. J. P. Alcocer, A. R. S. Kandada, S. D. Stranks, M. M. Lee, G. Lanzani, H. J. Snaith, A. Petrozza, *Nat. Commun.* **2014**, *5*, 3586.
- [112] N. Sestu, M. Cadelano, V. Sarritzu, F. Chen, D. Marongiu, R. Piras, M. Mainas, F. Quochi, M. Saba, A. Mura, G. Bongiovanni, *J. Phys. Chem. Lett.* **2015**, *6*, 4566.
- [113] Y. Yang, M. Yang, Z. Li, R. Crisp, K. Zhu, M. C. Beard, *J. Phys. Chem. Lett.* **2015**, *6*, 4688.
- [114] K. Galkowski, A. Mitioglu, A. Miyata, P. Plochocka, O. Portugall, G. E. Eperon, J. T.-W. Wang, T. Stergiopoulos, S. D. Stranks, H. J. Snaith, R. J. Nicholas, *Energy Environ. Sci.* **2016**, *9*, 962.
- [115] Y. Zhang, C.-K. Lim, Z. Dai, G. Yu, J. W. Haus, H. Zhang, P. N. Prasad, *Phys. Rep.* **2019**, *795*, 1.
- [116] A. Miyata, A. Mitioglu, P. Plochocka, O. Portugall, J. T.-W. Wang, S. D. Stranks, H. J. Snaith, R. J. Nicholas, *Nat. Phys.* **2015**, *11*, 582.
- [117] D. Marongiu, M. Saba, F. Quochi, A. Mura, G. Bongiovanni, *J. Mater. Chem. C* **2019**, *7*, 12006.
- [118] D. Zhang, Y. Yu, Y. Bekenstein, A. B. Wong, A. P. Alivisatos, P. Yang, *J. Am. Chem. Soc.* **2016**, *138*, 13155.
- [119] D. Zhang, L. Gu, Q. Zhang, Y. Lin, D.-H. Lien, M. Kam, S. Poddar, E. C. Garnett, A. Javey, Z. Fan, *Nano Lett.* **2019**, *19*, 2850.
- [120] N. Wang, L. Cheng, R. Ge, S. Zhang, Y. Miao, W. Zou, C. Yi, Y. Sun, Y. Cao, R. Yang, Y. Wei, Q. Guo, Y. Ke, M. Yu, Y. Jin, Y. Liu, Q. Ding, D. Di, L. Yang, G. Xing, H. Tian, C. Jin, F. Gao, R. H. Friend, J. Wang, W. Huang, *Nat. Photonics* **2016**, *10*, 699.
- [121] T. Ishihara, *J. Lumin.* **1994**, *60–61*, 269.
- [122] J. Hu, L. Yan, W. You, *Adv. Mater.* **2018**, *30*, 1802041.
- [123] W. Liu, J. Xing, J. Zhao, X. Wen, K. Wang, P. Lu, Q. Xiong, *Adv. Opt. Mater.* **2017**, *5*, 1601045.
- [124] J.-C. Blancon, H. Tsai, W. Nie, C. C. Stoumpos, L. Pedesseau, C. Katan, M. Kepenekian, C. M. M. Soe, K. Appavoo, M. Y. Sfeir, S. Tretiak, P. M. Ajayan, M. G. Kanatzidis, J. Even, J. J. Crochet, A. D. Mohite, *Science* **2017**, *355*, 1288.
- [125] M. C. Gélvez-Rueda, E. M. Hutter, D. H. Cao, N. Renaud, C. C. Stoumpos, J. T. Hupp, T. J. Savenije, M. G. Kanatzidis, F. C. Grozema, *J. Phys. Chem. C* **2017**, *121*, 26566.
- [126] J.-C. Blancon, A. V. Stier, H. Tsai, W. Nie, C. C. Stoumpos, B. Traoré, L. Pedesseau, M. Kepenekian, F. Katsutani, G. T. Noe, J. Kono, S. Tretiak, S. A. Crooker, C. Katan, M. G. Kanatzidis, J. J. Crochet, J. Even, A. D. Mohite, *Nat. Commun.* **2018**, *9*, 2254.
- [127] G. R. Yettapu, D. Talukdar, S. Sarkar, A. Swarnkar, A. Nag, P. Ghosh, P. Mandal, *Nano Lett.* **2016**, *16*, 4838.
- [128] Z. Yuan, C. Zhou, Y. Tian, Y. Shu, J. Messier, J. C. Wang, L. J. van de Burgt, K. Kountouriotis, Y. Xin, E. Holt, K. Schanze, R. Clark, T. Siegrist, B. Ma, *Nat. Commun.* **2017**, *8*, 14051.
- [129] H. Cho, S.-H. Jeong, M.-H. Park, Y.-H. Kim, C. Wolf, C.-L. Lee, J. H. Heo, A. Sadhanala, N. Myoung, S. Yoo, S. H. Im, R. H. Friend, T.-W. Lee, *Science* **2015**, *350*, 1222.
- [130] R. Yang, R. Li, Y. Cao, Y. Wei, Y. Miao, W. L. Tan, X. Jiao, H. Chen, L. Zhang, Q. Chen, H. Zhang, W. Zou, Y. Wang, M. Yang, C. Yi, N. Wang, F. Gao, C. R. McNeill, T. Qin, J. Wang, W. Huang, *Adv. Mater.* **2018**, *30*, 1804771.
- [131] W. Deng, X. Jin, Y. Lv, X. Zhang, X. Zhang, J. Jie, *Adv. Funct. Mater.* **2019**, *29*, 1903861.
- [132] Q. A. Akkerman, V. D'Innocenzo, S. Accornero, A. Scarpellini, A. Petrozza, M. Prato, L. Manna, *J. Am. Chem. Soc.* **2015**, *137*, 10276.
- [133] M. Yuan, L. N. Quan, R. Comin, G. Walters, R. Sabatini, O. Voznyy, S. Hoogland, Y. Zhao, E. M. Beaugregard, P. Kanjanaboos, Z. Lu, D. H. Kim, E. H. Sargent, *Nat. Nanotechnol.* **2016**, *11*, 872.
- [134] P. Li, Y. Chen, T. Yang, Z. Wang, H. Lin, Y. Xu, L. Li, H. Mu, B. N. Shivananju, Y. Zhang, Q. Zhang, A. Pan, S. Li, D. Tang, B. Jia, H. Zhang, Q. Bao, *ACS Appl. Mater. Interfaces* **2017**, *9*, 12759.
- [135] Y. Wang, X. Li, X. Zhao, L. Xiao, H. Zeng, H. Sun, *Nano Lett.* **2016**, *16*, 448.
- [136] W. Tian, H. Zhou, L. Li, *Small* **2017**, *13*, 1702107.
- [137] C. S. Ponceca, T. J. Savenije, M. Abdellah, K. Zheng, A. Yartsev, T. Pascher, T. Harlang, P. Chabera, T. Pullerits, A. Stepanov, J.-P. Wolf, V. Sundström, *J. Am. Chem. Soc.* **2014**, *136*, 5189.
- [138] Z. Yang, M. Wang, H. Qiu, X. Yao, X. Lao, S. Xu, Z. Lin, L. Sun, J. Shao, *Adv. Funct. Mater.* **2018**, *28*, 1705908.
- [139] G. Grancini, M. K. Nazeeruddin, *Nat. Rev. Mater.* **2019**, *4*, 4.
- [140] Y. Gao, M. Zhang, X. Zhang, G. Lu, *J. Phys. Chem. Lett.* **2019**, *10*, 3820.
- [141] H. Li, X. Wang, T. Zhang, X. Gong, Q. Sun, H. Pan, Y. Shen, S. Ahmad, M. Wang, *Adv. Funct. Mater.* **2019**, *29*, 1903293.
- [142] J. J. Choi, J. Luria, B.-R. Hyun, A. C. Bartnik, L. Sun, Y.-F. Lim, J. A. Marohn, F. W. Wise, T. Hanrath, *Nano Lett.* **2010**, *10*, 1805.
- [143] X. Song, X. Liu, D. Yu, C. Huo, J. Ji, X. Li, S. Zhang, Y. Zou, G. Zhu, Y. Wang, M. Wu, A. Xie, H. Zeng, *ACS Appl. Mater. Interfaces* **2018**, *10*, 2801.
- [144] K. Wang, C. Wu, Y. Jiang, D. Yang, K. Wang, S. Priya, *Sci. Adv.* **2019**, *5*, eaau3241.
- [145] J. Shi, Y. Li, Y. Li, D. Li, Y. Luo, H. Wu, Q. Meng, *Joule* **2018**, *2*, 879.
- [146] J. Bisquert, I. Mora-Seró, *J. Phys. Chem. Lett.* **2010**, *1*, 450.
- [147] H. Zhu, K. Miyata, Y. Fu, J. Wang, P. P. Joshi, D. Niesner, K. W. Williams, S. Jin, X. Y. Zhu, *Science* **2016**, *353*, 1409.
- [148] S. D. Stranks, G. E. Eperon, G. Grancini, C. Menelaou, M. J. P. Alcocer, T. Leijtens, L. M. Herz, A. Petrozza, H. J. Snaith, *Science* **2013**, *342*, 341.
- [149] C. Wehrenfennig, G. E. Eperon, M. B. Johnston, H. J. Snaith, L. M. Herz, *Adv. Mater.* **2014**, *26*, 1584.

- [150] R. L. Milot, G. E. Eperon, H. J. Snaith, M. B. Johnston, L. M. Herz, *Adv. Funct. Mater.* **2015**, *25*, 6218.
- [151] D. A. Valverde-Chávez, C. S. Ponseca, C. C. Stoumpos, A. Yartsev, M. G. Kanatzidis, V. Sundström, D. G. Cooke, *Energy Environ. Sci.* **2015**, *8*, 3700.
- [152] T. M. Brenner, D. A. Egger, A. M. Rappe, L. Kronik, G. Hodes, D. Cahen, *J. Phys. Chem. Lett.* **2015**, *6*, 4754.
- [153] L. M. Herz, *ACS Energy Lett.* **2017**, *2*, 1539.
- [154] B. Yang, K. Han, *Acc. Chem. Res.* **2019**, *52*, 3188.
- [155] W. Deng, L. Huang, X. Xu, X. Zhang, X. Jin, S.-T. Lee, J. Jie, *Nano Lett.* **2017**, *17*, 2482.
- [156] W. Tian, C. Zhao, J. Leng, R. Cui, S. Jin, *J. Am. Chem. Soc.* **2015**, *137*, 12458.
- [157] X. Hu, X. Wang, P. Fan, Y. Li, X. Zhang, Q. Liu, W. Zheng, G. Xu, X. Wang, X. Zhu, A. Pan, *Nano Lett.* **2018**, *18*, 3024.
- [158] F. Li, C. Ma, H. Wang, W. Hu, W. Yu, A. D. Sheikh, T. Wu, *Nat. Commun.* **2015**, *6*, 8238.
- [159] B. Yang, F. Zhang, J. Chen, S. Yang, X. Xia, T. Pullerits, W. Deng, K. Han, *Adv. Mater.* **2017**, *29*, 1703758.
- [160] D.-H. Kang, S. R. Pae, J. Shim, G. Yoo, J. Jeon, J. W. Leem, J. S. Yu, S. Lee, B. Shin, J.-H. Park, *Adv. Mater.* **2016**, *28*, 7799.
- [161] V. K. S. Hsiao, S.-F. Leung, Y.-C. Hsiao, P.-K. Kung, Y.-C. Lai, Z.-H. Lin, K. N. Salama, H. N. Alshareef, Z. L. Wang, J.-H. He, *Nano Energy* **2019**, *65*, 103958.
- [162] C. Bi, S. V. Kershaw, A. L. Rogach, J. Tian, *Adv. Funct. Mater.* **2019**, *29*, 1902446.
- [163] J. Dai, J. Xi, L. Li, J. Zhao, Y. Shi, W. Zhang, C. Ran, B. Jiao, X. Hou, X. Duan, Z. Wu, *Angew. Chem., Int. Ed.* **2018**, *57*, 5754.
- [164] R. Dong, C. Lan, X. Xu, X. Liang, X. Hu, D. Li, Z. Zhou, L. Shu, S. Yip, C. Li, S.-W. Tsang, J. C. Ho, *ACS Appl. Mater. Interfaces* **2018**, *10*, 19019.
- [165] B.-B. Zhang, S. Yuan, J.-P. Ma, Y. Zhou, J. Hou, X. Chen, W. Zheng, H. Shen, X.-C. Wang, B. Sun, O. M. Bakr, L.-S. Liao, H.-T. Sun, *J. Am. Chem. Soc.* **2019**, *141*, 15423.
- [166] A. Z. Chen, M. Shiu, J. H. Ma, M. R. Alpert, D. Zhang, B. J. Foley, D.-M. Smilgies, S.-H. Lee, J. J. Choi, *Nat. Commun.* **2018**, *9*, 1336.
- [167] J. Xue, Z. Zhu, X. Xu, Y. Gu, S. Wang, L. Xu, Y. Zou, J. Song, H. Zeng, Q. Chen, *Nano Lett.* **2018**, *18*, 7628.
- [168] S. Chatterjee, A. J. Pal, *ACS Appl. Mater. Interfaces* **2018**, *10*, 35194.
- [169] S. Zhu, M. Jiang, J. Ye, H. Xie, Y. Qiu, *Comput. Theor. Chem.* **2018**, *1144*, 1.
- [170] S. Lu, Q. Zhou, Y. Ouyang, Y. Guo, Q. Li, J. Wang, *Nat. Commun.* **2018**, *9*, 3405.
- [171] Z. Ma, Z. Shi, D. Yang, F. Zhang, S. Li, L. Wang, D. Wu, Y. Zhang, G. Na, L. Zhang, X. Li, Y. Zhang, C. Shan, *ACS Energy Lett.* **2020**, *5*, 385.
- [172] H. Gao, J. Feng, Y. Pi, Z. Zhou, B. Zhang, Y. Wu, X. Wang, X. Jiang, L. Jiang, *Adv. Funct. Mater.* **2018**, *28*, 1804349.
- [173] P. Cheng, T. Wu, J. Liu, W.-Q. Deng, K. Han, *J. Phys. Chem. Lett.* **2018**, *9*, 2518.
- [174] L. Ji, X. Zhang, T. Zhang, Y. Wang, F. Wang, Z. Zhong, Z. D. Chen, Z. Xiao, L. Chen, S. Li, *J. Mater. Chem. A* **2019**, *7*, 9154.
- [175] T. Lei, M. Lai, Q. Kong, D. Lu, W. Lee, L. Dou, V. Wu, Y. Yu, P. Yang, *Nano Lett.* **2018**, *18*, 3538.
- [176] D. Amgar, T. Binyamin, V. Uvarov, L. Etgar, *Nanoscale* **2018**, *10*, 6060.
- [177] S. Baek, S. Kim, J. Y. Noh, J. H. Heo, S. H. Im, K.-H. Hong, S.-W. Kim, *Adv. Opt. Mater.* **2018**, *6*, 1800295.
- [178] D. Dong, H. Deng, C. Hu, H. Song, K. Qiao, X. Yang, J. Zhang, F. Cai, J. Tang, H. Song, *Nanoscale* **2017**, *9*, 1567.
- [179] S. Prathapani, P. Bhargava, S. Mallick, *Appl. Phys. Lett.* **2018**, *112*, 092104.
- [180] S.-H. Turren-Cruz, A. Hagfeldt, M. Saliba, *Science* **2018**, *362*, 449.
- [181] C. C. Stoumpos, D. H. Cao, D. J. Clark, J. Young, J. M. Rondinelli, J. I. Jang, J. T. Hupp, M. G. Kanatzidis, *Chem. Mater.* **2016**, *28*, 2852.
- [182] L. N. Quan, F. P. García de Arquer, R. P. Sabatini, E. H. Sargent, *Adv. Mater.* **2018**, *30*, 1801996.
- [183] D. H. Cao, C. C. Stoumpos, T. Yokoyama, J. L. Logsdon, T.-B. Song, O. K. Farha, M. R. Wasielewski, J. T. Hupp, M. G. Kanatzidis, *ACS Energy Lett.* **2017**, *2*, 982.
- [184] L. Mao, W. Ke, L. Pedesseau, Y. Wu, C. Katan, J. Even, M. R. Wasielewski, C. C. Stoumpos, M. G. Kanatzidis, *J. Am. Chem. Soc.* **2018**, *140*, 3775.
- [185] M. E. Kamminga, H.-H. Fang, M. R. Filip, F. Giustino, J. Baas, G. R. Blake, M. A. Loi, T. T. M. Palstra, *Chem. Mater.* **2016**, *28*, 4554.
- [186] J. Butkus, P. Vashishtha, K. Chen, J. K. Gallaher, S. K. K. Prasad, D. Z. Metin, G. Laufersky, N. Gaston, J. E. Halpert, J. M. Hodgkiss, *Chem. Mater.* **2017**, *29*, 3644.
- [187] Y. Liu, M. Guo, S. Dong, X. Jiao, T. Wang, D. Chen, *J. Mater. Chem. C* **2018**, *6*, 7797.
- [188] Z. Zheng, X. Wang, Y. Shen, Z. Luo, L. Li, L. Gan, Y. Ma, H. Li, A. Pan, T. Zhai, *Adv. Opt. Mater.* **2018**, *6*, 1800879.
- [189] L. Zhang, K. Wang, Y. Lin, B. Zou, *J. Phys. Chem. Lett.* **2020**, *11*, 4693.
- [190] N. N. Som, P. M. W. P. Sampath, S. D. Dabhi, V. Mankad, S. Shinde, M. L. C. Attygalle, P. K. Jha, *Sol. Energy* **2018**, *173*, 1315.
- [191] G. Feng, Y. Qin, C. Ran, L. Ji, L. Dong, W. Li, *APL Mater.* **2018**, *6*, 114201.
- [192] Q. Tu, I. Spanopoulos, S. Hao, C. Wolverton, M. G. Kanatzidis, G. S. Shekawat, V. P. Dravid, *ACS Energy Lett.* **2019**, *4*, 796.
- [193] X. Hu, X. Zhang, L. Liang, J. Bao, S. Li, W. Yang, Y. Xie, *Adv. Funct. Mater.* **2014**, *24*, 7373.
- [194] Y. Shao, Y. Fang, T. Li, Q. Wang, Q. Dong, Y. Deng, Y. Yuan, H. Wei, M. Wang, A. Gruverman, J. Shield, J. Huang, *Energy Environ. Sci.* **2016**, *9*, 1752.
- [195] Z. Lian, Q. Yan, Q. Lv, Y. Wang, L. Liu, L. Zhang, S. Pan, Q. Li, L. Wang, J.-L. Sun, *Sci. Rep.* **2015**, *5*, 16563.
- [196] K. Lin, J. Xing, L. N. Quan, F. P. G. de Arquer, X. Gong, J. Lu, L. Xie, W. Zhao, D. Zhang, C. Yan, W. Li, X. Liu, Y. Lu, J. Kirman, E. H. Sargent, Q. Xiong, Z. Wei, *Nature* **2018**, *562*, 245.
- [197] Z. Liu, C.-H. Lin, B.-R. Hyun, C.-W. Sher, Z. Lv, B. Luo, F. Jiang, T. Wu, C.-H. Ho, H.-C. Kuo, J.-H. He, *Light: Sci. Appl.* **2020**, *9*, 83.
- [198] P. Ramasamy, D.-H. Lim, B. Kim, S.-H. Lee, M.-S. Lee, J.-S. Lee, *Chem. Commun.* **2016**, *52*, 2067.
- [199] Y. Wang, Y. Zhang, Y. Lu, W. Xu, H. Mu, C. Chen, H. Qiao, J. Song, S. Li, B. Sun, Y.-B. Cheng, Q. Bao, *Adv. Opt. Mater.* **2015**, *3*, 1389.
- [200] J. Li, Y. Shen, Y. Liu, F. Shi, X. Ren, T. Niu, K. Zhao, S. F. Liu, *ACS Appl. Mater. Interfaces* **2017**, *9*, 19176.
- [201] M. I. Saidaminov, M. A. Haque, M. Savoie, A. L. Abdelhady, N. Cho, I. Dursun, U. Buttner, E. Alarousu, T. Wu, O. M. Bakr, *Adv. Mater.* **2016**, *28*, 8144.
- [202] A. A. Bessonov, M. Allen, Y. Liu, S. Malik, J. Bottomley, A. Rushton, I. Medina-Salazar, M. Voutilainen, S. Kallioinen, A. Colli, C. Bower, P. Andrew, T. Ryhänen, *ACS Nano* **2017**, *11*, 5547.
- [203] J. Chen, W. Ouyang, W. Yang, J. He, X. Fang, *Adv. Funct. Mater.* **2020**, *30*, 1909909.
- [204] B. A. Koscher, J. K. Swabeck, N. D. Bronstein, A. P. Alivisatos, *J. Am. Chem. Soc.* **2017**, *139*, 6566.
- [205] H. Wu, Z. Kang, Z. Zhang, H. Si, S. Zhang, Z. Zhang, Q. Liao, Y. Zhang, *Small Methods* **2019**, *3*, 1900117.
- [206] J. Pan, L. N. Quan, Y. Zhao, W. Peng, B. Murali, S. P. Sarmah, M. Yuan, L. Sinatra, N. M. Alyami, J. Liu, E. Yassitepe, Z. Yang, O. Voznyy, R. Comin, M. N. Hedhili, O. F. Mohammed, Z. H. Lu, D. H. Kim, E. H. Sargent, O. M. Bakr, *Adv. Mater.* **2016**, *28*, 8718.
- [207] J. Pan, Y. Shang, J. Yin, M. De Bastiani, W. Peng, I. Dursun, L. Sinatra, A. M. El-Zohry, M. N. Hedhili, A.-H. Emwas, O. F. Mohammed, Z. Ning, O. M. Bakr, *J. Am. Chem. Soc.* **2018**, *140*, 562.
- [208] M. Gong, R. Sakidja, R. Goul, D. Ewing, M. Casper, A. Stramel, A. Elliot, J. Z. Wu, *ACS Nano* **2019**, *13*, 1772.

- [209] L. Zhou, K. Yu, F. Yang, H. Cong, N. Wang, J. Zheng, Y. Zuo, C. Li, B. Cheng, Q. Wang, *J. Mater. Chem. C* **2017**, *5*, 6224.
- [210] F. Zhang, B. Yang, K. Zheng, S. Yang, Y. Li, W. Deng, R. He, *Nano-Micro Lett.* **2018**, *10*, 43.
- [211] Y. Li, Z. Shi, L. Lei, F. Zhang, Z. Ma, D. Wu, T. Xu, Y. Tian, Y. Zhang, G. Du, C. Shan, X. Li, *Chem. Mater.* **2018**, *30*, 6744.
- [212] X. Liu, D. Yu, F. Cao, X. Li, J. Ji, J. Chen, X. Song, H. Zeng, *Small* **2017**, *13*, 1700364.
- [213] J. P. Clifford, G. Konstantatos, K. W. Johnston, S. Hoogland, L. Levina, E. H. Sargent, *Nat. Nanotechnol.* **2009**, *4*, 40.
- [214] L. Ji, H.-Y. Hsu, J. C. Lee, A. J. Bard, E. T. Yu, *Nano Lett.* **2018**, *18*, 994.
- [215] T. M. Brenner, D. A. Egger, L. Kronik, G. Hodes, D. Cahen, *Nat. Rev. Mater.* **2016**, *1*, 15007.
- [216] X. Li, D. Yu, F. Cao, Y. Gu, Y. Wei, Y. Wu, J. Song, H. Zeng, *Adv. Funct. Mater.* **2016**, *26*, 5903.
- [217] Y. Dong, Y. Gu, Y. Zou, J. Song, L. Xu, J. Li, J. Xue, X. Li, H. Zeng, *Small* **2016**, *12*, 5622.
- [218] J. Xue, Y. Gu, Q. Shan, Y. Zou, J. Song, L. Xu, Y. Dong, J. Li, H. Zeng, *Angew. Chem., Int. Ed.* **2017**, *56*, 5232.
- [219] Z. Dai, Q. Ou, C. Wang, G. Si, B. Shabbir, C. Zheng, Z. Wang, Y. Zhang, Y. Huang, Y. Dong, J. J. Jasieniak, B. Su, Q. Bao, *J. Mater. Chem. C* **2019**, *7*, 5954.
- [220] H. Zhou, Z. Song, C. R. Grice, C. Chen, X. Yang, H. Wang, Y. Yan, *J. Phys. Chem. Lett.* **2018**, *9*, 4714.
- [221] J. Xing, X. F. Liu, Q. Zhang, S. T. Ha, Y. W. Yuan, C. Shen, T. C. Sum, Q. Xiong, *Nano Lett.* **2015**, *15*, 4571.
- [222] H. Zhu, Y. Fu, F. Meng, X. Wu, Z. Gong, Q. Ding, M. V. Gustafsson, M. T. Trinh, S. Jin, X.-Y. Zhu, *Nat. Mater.* **2015**, *14*, 636.
- [223] S. Zhuo, J. Zhang, Y. Shi, Y. Huang, B. Zhang, *Angew. Chem., Int. Ed.* **2015**, *54*, 5693.
- [224] B.-S. Zhu, Z. He, J.-S. Yao, C. Chen, K.-H. Wang, H.-B. Yao, J.-W. Liu, S.-H. Yu, *Adv. Opt. Mater.* **2018**, *6*, 1701029.
- [225] H. Zhou, Z. Song, C. R. Grice, C. Chen, J. Zhang, Y. Zhu, R. Liu, H. Wang, Y. Yan, *Nano Energy* **2018**, *53*, 880.
- [226] W. Zhai, J. Lin, C. Li, S. Hu, Y. Huang, C. Yu, Z. Wen, Z. Liu, Y. Fang, C. Tang, *Nanoscale* **2018**, *10*, 21451.
- [227] I. M. Asuo, P. Fourmont, I. Ka, D. Gedamu, S. Bouzidi, A. Pignolet, R. Nechache, S. G. Cloutier, *Small* **2019**, *15*, 1804150.
- [228] P. Zhu, S. Gu, X. Shen, N. Xu, Y. Tan, S. Zhuang, Y. Deng, Z. Lu, Z. Wang, J. Zhu, *Nano Lett.* **2016**, *16*, 871.
- [229] C.-H. Lin, T.-Y. Li, J. Zhang, Z.-Y. Chiao, P.-C. Wei, H.-C. Fu, L. Hu, M.-J. Yu, G. H. Ahmed, X. Guan, C.-H. Ho, T. Wu, B. S. Ooi, O. F. Mohammed, Y.-J. Lu, X. Fang, J.-H. He, *Nano Energy* **2020**, *73*, 104801.
- [230] A. Waleed, M. M. Tavakoli, L. Gu, Z. Wang, D. Zhang, A. Manikandan, Q. Zhang, R. Zhang, Y.-L. Chueh, Z. Fan, *Nano Lett.* **2017**, *17*, 523.
- [231] L. Gu, S. Poddar, Y. Lin, Z. Long, D. Zhang, Q. Zhang, L. Shu, X. Qiu, M. Kam, A. Javey, Z. Fan, *Nature* **2020**, *581*, 278.
- [232] J. Wang, M. S. Gudiksen, X. Duan, Y. Cui, C. M. Lieber, *Science* **2001**, *293*, 1455.
- [233] C. Lin, C. Kang, T. Wu, C. Tsai, C. Sher, X. Guan, P. Lee, T. Wu, C. Ho, H. Kuo, J. He, *Adv. Funct. Mater.* **2020**, *30*, 1909275.
- [234] J. Feng, X. Yan, Y. Liu, H. Gao, Y. Wu, B. Su, L. Jiang, *Adv. Mater.* **2017**, *29*, 1605993.
- [235] M. Shoaib, X. Zhang, X. Wang, H. Zhou, T. Xu, X. Wang, X. Hu, H. Liu, X. Fan, W. Zheng, T. Yang, S. Yang, Q. Zhang, X. Zhu, L. Sun, A. Pan, *J. Am. Chem. Soc.* **2017**, *139*, 15592.
- [236] P. Gui, Z. Chen, B. Li, F. Yao, X. Zheng, Q. Lin, G. Fang, *ACS Photonics* **2018**, *5*, 2113.
- [237] T. Yang, Y. Zheng, Z. Du, W. Liu, Z. Yang, F. Gao, L. Wang, K.-C. Chou, X. Hou, W. Yang, *ACS Nano* **2018**, *12*, 1611.
- [238] Z. Li, Z. Li, Z. Shi, X. Fang, *Adv. Funct. Mater.* **2020**, *30*, 2002634.
- [239] Y. Chen, J. Zhang, J. Zhou, Y. Chu, B. Zhou, X. Wu, J. Huang, *Adv. Opt. Mater.* **2018**, *6*, 1800469.
- [240] L. Lv, Y. Xu, H. Fang, W. Luo, F. Xu, L. Liu, B. Wang, X. Zhang, D. Yang, W. Hu, A. Dong, *Nanoscale* **2016**, *8*, 13589.
- [241] J. Song, L. Xu, J. Li, J. Xue, Y. Dong, X. Li, H. Zeng, *Adv. Mater.* **2016**, *28*, 4861.
- [242] J. Zhou, Y. Chu, J. Huang, *ACS Appl. Mater. Interfaces* **2016**, *8*, 25660.
- [243] K. Wang, C. Wu, D. Yang, Y. Jiang, S. Priya, *ACS Nano* **2018**, *12*, 4919.
- [244] R. Dong, C. Lan, F. Li, S. Yip, J. C. Ho, *Nanoscale Horiz.* **2019**, *4*, 1342.
- [245] J. R. Ayres, *J. Appl. Phys.* **1993**, *74*, 1787.
- [246] L. L. Kerr, S. S. Li, S. W. Johnston, T. J. Anderson, O. D. Crisalle, W. K. Kim, J. Abushama, R. N. Noufi, *Solid-State Electron.* **2004**, *48*, 1579.
- [247] A. Balcioglu, R. K. Ahrenkiel, F. Hasoon, *J. Appl. Phys.* **2000**, *88*, 7175.
- [248] D. Shi, V. Adinolfi, R. Comin, M. Yuan, E. Alarousu, A. Buin, Y. Chen, S. Hoogland, A. Rothenberger, K. Katsiev, Y. Losovyj, X. Zhang, P. A. Dowben, O. F. Mohammed, E. H. Sargent, O. M. Bakr, *Science* **2015**, *347*, 519.
- [249] M. Saliba, J.-P. Correa-Baena, M. Grätzel, A. Hagfeldt, A. Abate, *Angew. Chem., Int. Ed.* **2018**, *57*, 2554.
- [250] D. P. McMeekin, G. Sadoughi, W. Rehman, G. E. Eperon, M. Saliba, M. T. Horantner, A. Haghighirad, N. Sakai, L. Korte, B. Rech, M. B. Johnston, L. M. Herz, H. J. Snaith, *Science* **2016**, *351*, 151.
- [251] D. Bi, W. Tress, M. I. Dar, P. Gao, J. Luo, C. Renevier, K. Schenk, A. Abate, F. Giordano, J.-P. Correa Baena, J.-D. Decoppet, S. M. Zakeeruddin, M. K. Nazeeruddin, M. Grätzel, A. Hagfeldt, *Sci. Adv.* **2016**, *2*, e1501170.
- [252] N. Zhou, Y. Shen, L. Li, S. Tan, N. Liu, G. Zheng, Q. Chen, H. Zhou, *J. Am. Chem. Soc.* **2018**, *140*, 459.
- [253] X. Zhang, X. Ren, B. Liu, R. Munir, X. Zhu, D. Yang, J. Li, Y. Liu, D.-M. Smilgies, R. Li, Z. Yang, T. Niu, X. Wang, A. Amassian, K. Zhao, S. (Frank) Liu, *Energy Environ. Sci.* **2017**, *10*, 2095.
- [254] L. Iagher, L. Etgar, *ACS Energy Lett.* **2018**, *3*, 366.
- [255] Y. Liu, H. Ye, Y. Zhang, K. Zhao, Z. Yang, Y. Yuan, H. Wu, G. Zhao, Z. Yang, J. Tang, Z. Xu, S. (Frank) Liu, *Matter* **2019**, *1*, 465.
- [256] X. Guo, Q. Liu, H. Zhou, X. Luan, C. Li, Z. Hu, A. Hu, X. He, *IEEE Electron Device Lett.* **2018**, *39*, 228.
- [257] D. Yu, F. Cao, Y. Shen, X. Liu, Y. Zhu, H. Zeng, *J. Phys. Chem. Lett.* **2017**, *8*, 2565.
- [258] J. Wang, J. Li, S. Lan, C. Fang, H. Shen, Q. Xiong, D. Li, *ACS Nano* **2019**, *13*, 5473.
- [259] C. D. Stanciu, F. Hansteen, A. V. Kimel, A. Kirilyuk, A. Tsukamoto, A. Itoh, T. Rasing, *Phys. Rev. Lett.* **2007**, *99*, 047601.
- [260] G. A. Hembury, V. V. Borovkov, Y. Inoue, *Chem. Rev.* **2008**, *108*, 1.
- [261] Y. Yang, R. C. da Costa, M. J. Fuchter, A. J. Campbell, *Nat. Photonics* **2013**, *7*, 634.
- [262] J. Petersen, J. Volz, A. Rauschenbeutel, *Science* **2014**, *346*, 67.
- [263] D. G. Billing, A. Lemmerer, *CrystEngComm* **2006**, *8*, 686.
- [264] C. Chen, L. Gao, W. Gao, C. Ge, X. Du, Z. Li, Y. Yang, G. Niu, J. Tang, *Nat. Commun.* **2019**, *10*, 1927.
- [265] J. Ma, C. Fang, C. Chen, L. Jin, J. Wang, S. Wang, J. Tang, D. Li, *ACS Nano* **2019**, *13*, 3659.
- [266] S. Heo, G. Seo, K. T. Cho, Y. Lee, S. Paek, S. Kim, M. Seol, S. H. Kim, D.-J. Yun, K. Kim, J. Park, J. Lee, L. Lechner, T. Rodgers, J. W. Chung, J.-S. Kim, D. Lee, S.-H. Choi, M. K. Nazeeruddin, *Adv. Energy Mater.* **2019**, *9*, 1902470.
- [267] D.-H. Lien, Z. Dong, J. R. D. Retamal, H.-P. Wang, T.-C. Wei, D. Wang, J.-H. He, Y. Cui, *Adv. Mater.* **2018**, *30*, 1801972.
- [268] S. Das, M. J. Hossain, S.-F. Leung, A. Lenox, Y. Jung, K. Davis, J.-H. He, T. Roy, *Nano Energy* **2019**, *58*, 47.
- [269] H.-P. Wang, D. Periyangounder, A.-C. Li, J.-H. He, *IEEE Access* **2019**, *7*, 19395.
- [270] G. Grancini, C. Roldán-Carmona, I. Zimmermann, E. Mosconi, X. Lee, D. Martineau, S. Narbey, F. Oswald, F. De Angelis, M. Graetzel, M. K. Nazeeruddin, *Nat. Commun.* **2017**, *8*, 15684.

- [271] Z. Wang, Q. Lin, F. P. Chmiel, N. Sakai, L. M. Herz, H. J. Snaith, *Nat. Energy* **2017**, *2*, 17135.
- [272] Y. Shen, D. Yu, X. Wang, C. Huo, Y. Wu, Z. Zhu, H. Zeng, *Nanotechnology* **2018**, *29*, 85201.
- [273] Y. Lee, J. Kwon, E. Hwang, C.-H. Ra, W. J. Yoo, J.-H. Ahn, J. H. Park, J. H. Cho, *Adv. Mater.* **2015**, *27*, 41.
- [274] N. Cho, F. Li, B. Turedi, L. Sinatra, S. P. Sarmah, M. R. Parida, M. I. Saidaminov, B. Murali, V. M. Burlakov, A. Goriely, O. F. Mohammed, T. Wu, O. M. Bakr, *Nat. Commun.* **2016**, *7*, 13407.
- [275] T. Mueller, F. Xia, P. Avouris, *Nat. Photonics* **2010**, *4*, 297.
- [276] D.-H. Kwak, D.-H. Lim, H.-S. Ra, P. Ramasamy, J.-S. Lee, *RSC Adv.* **2016**, *6*, 65252.
- [277] M. Spina, M. Lehmann, B. Náfrádi, L. Bernard, E. Bonvin, R. Gaál, A. Magrez, L. Forró, E. Horváth, *Small* **2015**, *11*, 4824.
- [278] Y. Chen, Y. Sun, J. Peng, J. Tang, K. Zheng, Z. Liang, *Adv. Mater.* **2018**, *30*, 1703487.
- [279] C. Fang, H. Wang, Z. Shen, H. Shen, S. Wang, J. Ma, J. Wang, H. Luo, D. Li, *ACS Appl. Mater. Interfaces* **2019**, *11*, 8419.
- [280] H. Algadi, C. Mahata, J. Woo, M. Lee, M. Kim, T. Lee, *Electronics* **2019**, *8*, 678.
- [281] S. Chen, G. Shi, *Adv. Mater.* **2017**, *29*, 1605448.
- [282] H. Wu, H. Si, Z. Zhang, Z. Kang, P. Wu, L. Zhou, S. Zhang, Z. Zhang, Q. Liao, Y. Zhang, *Adv. Sci.* **2018**, *5*, 1801219.
- [283] P. A. Shaikh, D. Shi, J. R. D. Retamal, A. D. Sheikh, M. A. Haque, C.-F. Kang, J.-H. He, O. M. Bakr, T. Wu, *J. Mater. Chem. C* **2016**, *4*, 8304.
- [284] Q. Fu, X. Wang, F. Liu, Y. Dong, Z. Liu, S. Zheng, A. Chaturvedi, J. Zhou, P. Hu, Z. Zhu, F. Bo, Y. Long, Z. Liu, *Small* **2019**, *15*, 1902890.
- [285] X. Zhang, Q. Wang, Z. Jin, J. Zhang, S. (Frank) Liu, *Nanoscale* **2017**, *9*, 6278.
- [286] J. Lu, X. Sheng, G. Tong, Z. Yu, X. Sun, L. Yu, X. Xu, J. Wang, J. Xu, Y. Shi, K. Chen, *Adv. Mater.* **2017**, *29*, 1700400.
- [287] M. Zhang, L. Wang, L. Meng, X.-G. Wu, Q. Tan, Y. Chen, W. Liang, F. Jiang, Y. Cai, H. Zhong, *Adv. Mater.* **2018**, *6*, 1800077.
- [288] H. Fang, C. Battaglia, C. Carraro, S. Nemsak, B. Ozdol, J. S. Kang, H. A. Bechtel, S. B. Desai, F. Kronast, A. A. Unal, G. Conti, C. Conlon, G. K. Palsson, M. C. Martin, A. M. Minor, C. S. Fadley, E. Yablonovitch, R. Maboudian, A. Javey, *Proc. Natl. Acad. Sci. USA* **2014**, *111*, 6198.
- [289] B. Conings, J. Drijkoningen, N. Gauquelin, A. Babayigit, J. D'Haen, L. D'Olieslaeger, A. Ethirajan, J. Verbeeck, J. Manca, E. Mosconi, F. De Angelis, H.-G. Boyen, *Adv. Energy Mater.* **2015**, *5*, 1500477.
- [290] E. J. Juarez-Perez, Z. Hawash, S. R. Raga, L. K. Ono, Y. Qi, *Energy Environ. Sci.* **2016**, *9*, 3406.
- [291] Q. Han, S.-H. Bae, P. Sun, Y.-T. Hsieh, Y. M. Yang, Y. S. Rim, H. Zhao, Q. Chen, W. Shi, G. Li, Y. Yang, *Adv. Mater.* **2016**, *28*, 2253.
- [292] C. C. Stoumpos, C. D. Malliakas, M. G. Kanatzidis, *Inorg. Chem.* **2013**, *52*, 9019.
- [293] A. Swarnkar, A. R. Marshall, E. M. Sanehira, B. D. Chernomordik, D. T. Moore, J. A. Christians, T. Chakrabarti, J. M. Luther, *Science* **2016**, *354*, 92.
- [294] G. Chen, J. Feng, H. Gao, Y. Zhao, Y. Pi, X. Jiang, Y. Wu, L. Jiang, *Adv. Funct. Mater.* **2019**, *29*, 1808741.
- [295] B. Jeong, H. Han, Y. J. Choi, S. H. Cho, E. H. Kim, S. W. Lee, J. S. Kim, C. Park, D. Kim, C. Park, *Adv. Funct. Mater.* **2018**, *28*, 1706401.
- [296] B. Li, Y. Zhang, L. Fu, T. Yu, S. Zhou, L. Zhang, L. Yin, *Nat. Commun.* **2018**, *9*, 1076.
- [297] U. Bansode, A. Rahman, S. Ogale, *J. Mater. Chem. C* **2019**, *7*, 6986.
- [298] Y. Lin, Y. Bai, Y. Fang, Q. Wang, Y. Deng, J. Huang, *ACS Energy Lett.* **2017**, *2*, 1571.
- [299] J.-W. Lee, S.-G. Kim, J.-M. Yang, Y. Yang, N.-G. Park, *APL Mater.* **2019**, *7*, 41111.
- [300] Y. Zhang, S. Li, W. Yang, M. K. Joshi, X. Fang, *J. Phys. Chem. Lett.* **2019**, *10*, 2400.
- [301] Y. Li, Z. Shi, W. Liang, L. Wang, S. Li, F. Zhang, Z. Ma, Y. Wang, Y. Tian, D. Wu, X. Li, Y. Zhang, C. Shan, X. Fang, *Mater. Horiz.* **2020**, *7*, 530.
- [302] Y. Zhang, W. Xu, X. Xu, J. Cai, W. Yang, X. Fang, *J. Phys. Chem. Lett.* **2019**, *10*, 836.
- [303] J. W. Lim, H. Wang, C. H. Choi, H. Kwon, L. N. Quan, W.-T. Park, Y.-Y. Noh, D. H. Kim, *Nano Energy* **2019**, *57*, 761.
- [304] J. Ding, H. Fang, Z. Lian, J. Li, Q. Lv, L. Wang, J.-L. Sun, Q. Yan, *CrystEngComm* **2016**, *18*, 4405.
- [305] L. Zeng, Q. Chen, Z. Zhang, D. Wu, H. Yuan, Y. Li, W. Qarony, S. P. Lau, L. Luo, Y. H. Tsang, *Adv. Sci.* **2019**, *6*, 1901134.
- [306] X. Liu, S. Wang, P. Long, L. Li, Y. Peng, Z. Xu, S. Han, Z. Sun, M. Hong, J. Luo, *Angew. Chem., Int. Ed.* **2019**, *58*, 14504.
- [307] S. Wang, L. Li, W. Weng, C. Ji, X. Liu, Z. Sun, W. Lin, M. Hong, J. Luo, *J. Am. Chem. Soc.* **2020**, *142*, 55.
- [308] P. Newman, The Internet of Things 2020—Business Insider, <https://www.businessinsider.com/internet-of-things-report> (accessed: March 2020).
- [309] F. Bao, J. Yang, S. Bai, W. Xu, Z. Yan, Q. Xu, J. Liu, W. Zhang, F. Gao, *Adv. Mater.* **2018**, *30*, 1803422.
- [310] C. Li, J. Lu, Y. Zhao, L. Sun, G. Wang, Y. Ma, S. Zhang, J. Zhou, L. Shen, W. Huang, *Small* **2019**, *15*, 1903599.
- [311] R. Liu, J. Zhang, H. Zhou, Z. Song, Z. Song, C. R. Grice, D. Wu, L. Shen, H. Wang, *Adv. Opt. Mater.* **2020**, *8*, 1901735.
- [312] C. H. Kang, I. Dursun, G. Liu, L. Sinatra, X. Sun, M. Kong, J. Pan, P. Maity, E.-N. Ooi, T. K. Ng, O. F. Mohammed, O. M. Bakr, B. S. Ooi, *Light: Sci. Appl.* **2019**, *8*, 94.
- [313] J. Kirman, A. Johnston, D. A. Kuntz, M. Askerka, Y. Gao, P. Todorović, D. Ma, G. G. Privé, E. H. Sargent, *Matter* **2020**, *2*, 938.
- [314] C.-H. Lin, T.-Y. Li, B. Cheng, C. Liu, C.-W. Yang, J.-J. Ke, T.-C. Wei, L.-J. Li, A. Fratallocchi, J.-H. He, *Nano Energy* **2018**, *53*, 817.
- [315] N. Zhang, W. Sun, S. P. Rodrigues, K. Wang, Z. Gu, S. Wang, W. Cai, S. Xiao, Q. Song, *Adv. Mater.* **2017**, *29*, 1606205.
- [316] C.-H. Lin, B. Cheng, T.-Y. Li, J. R. D. Retamal, T.-C. Wei, H.-C. Fu, X. Fang, J.-H. He, *ACS Nano* **2019**, *13*, 1168.
- [317] H. Zhou, J. Zeng, Z. Song, C. R. Grice, C. Chen, Z. Song, D. Zhao, H. Wang, Y. Yan, *J. Phys. Chem. Lett.* **2018**, *9*, 2043.
- [318] J. Chen, Q. Jing, F. Xu, Z. Lu, Y. Lu, *Optica* **2017**, *4*, 835.
- [319] C. Tian, F. Wang, Y. Wang, X. Chen, J. Mei, H. Liu, D. Zhao, *ACS Appl. Mater. Interfaces* **2019**, *11*, 15804.
- [320] Y. Zhang, J. Du, X. Wu, G. Zhang, Y. Chu, D. Liu, Y. Zhao, Z. Liang, J. Huang, *ACS Appl. Mater. Interfaces* **2015**, *7*, 21634.
- [321] Z. Sun, L. Aigouy, Z. Chen, *Nanoscale* **2016**, *8*, 7377.
- [322] B. Pradhan, G. S. Kumar, S. Sain, A. Dalui, U. K. Ghorai, S. K. Pradhan, S. Acharya, *Chem. Mater.* **2018**, *30*, 2135.
- [323] X. Tang, Z. Zu, H. Shao, W. Hu, M. Zhou, M. Deng, W. Chen, Z. Zang, T. Zhu, J. Xue, *Nanoscale* **2016**, *8*, 15158.
- [324] D. Zhang, Y. Yang, Y. Bekenstein, Y. Yu, N. A. Gibson, A. B. Wong, S. W. Eaton, N. Kornienko, Q. Kong, M. Lai, A. P. Alivisatos, S. R. Leone, P. Yang, *J. Am. Chem. Soc.* **2016**, *138*, 7236.
- [325] Y. Li, Z. Shi, L. Lei, Z. Ma, F. Zhang, S. Li, D. Wu, T. Xu, X. Li, C. Shan, G. Du, *ACS Photonics* **2018**, *5*, 2524.
- [326] M. Lai, Q. Kong, C. G. Bischak, Y. Yu, L. Dou, S. W. Eaton, N. S. Ginsberg, P. Yang, *Nano Res.* **2017**, *10*, 1107.
- [327] Y. Meng, C. Lan, F. Li, S. Yip, R. Wei, X. Kang, X. Bu, R. Dong, H. Zhang, J. C. Ho, *ACS Nano* **2019**, *13*, 6060.
- [328] Y. Zhou, J. Luo, Y. Zhao, C. Ge, C. Wang, L. Gao, C. Zhang, M. Hu, G. Niu, J. Tang, *Adv. Opt. Mater.* **2018**, *6*, 1800679.
- [329] M. Wang, W. Tian, F. Cao, M. Wang, L. Li, *Adv. Funct. Mater.* **2020**, *30*, 1909771.
- [330] M. Spina, E. Bonvin, A. Sienkiewicz, B. Náfrádi, L. Forró, E. Horváth, *Sci. Rep.* **2016**, *6*, 19834.



- [331] H. Deng, D. Dong, K. Qiao, L. Bu, B. Li, D. Yang, H.-E. Wang, Y. Cheng, Z. Zhao, J. Tang, H. Song, *Nanoscale* **2015**, *7*, 4163.
- [332] I. M. Asuo, D. Gedamu, I. Ka, L. F. Gerlein, F.-X. Fortier, A. Pignolet, S. G. Cloutier, R. Nechache, *Nano Energy* **2018**, *51*, 324.
- [333] W. Wang, Y. Ma, L. Qi, *Adv. Funct. Mater.* **2017**, *27*, 1603653.
- [334] H.-C. Cheng, G. Wang, D. Li, Q. He, A. Yin, Y. Liu, H. Wu, M. Ding, Y. Huang, X. Duan, *Nano Lett.* **2016**, *16*, 367.
- [335] P. Li, B. N. Shivananju, Y. Zhang, S. Li, Q. Bao, *J. Phys. D: Appl. Phys.* **2017**, *50*, 94002.
- [336] W. Zheng, R. Lin, Z. Zhang, Q. Liao, J. Liu, F. Huang, *Nanoscale* **2017**, *9*, 12718.
- [337] L. Li, Z. Sun, P. Wang, W. Hu, S. Wang, C. Ji, M. Hong, J. Luo, *Angew. Chem., Int. Ed.* **2017**, *56*, 12150.
- [338] Z. Qi, X. Fu, T. Yang, D. Li, P. Fan, H. Li, F. Jiang, L. Li, Z. Luo, X. Zhuang, A. Pan, *Nano Res.* **2019**, *12*, 1894.
- [339] X. Fu, S. Jiao, Y. Jiang, L. Li, X. Wang, C. Zhu, C. Ma, H. Zhao, Z. Xu, Y. Liu, W. Huang, W. Zheng, P. Fan, F. Jiang, D. Zhang, X. Zhu, X. Wang, A. Pan, *ACS Appl. Mater. Interfaces* **2020**, *12*, 2884.



**Hsin-Ping Wang** received her B.S. and Ph.D. degrees from National Taiwan University, Taipei, Taiwan, in 2011 and 2017, respectively. Then, she was a postdoc researcher at Stanford University. Her research interests include theoretical and experimental research on optical properties analysis of nanostructure, varied types of solar cells, and solar water splitting cells.



**Siyuan Li** is currently a postgraduate student in Prof. Xiaosheng Fang's research group at the Department of Materials Science, Fudan University, China. He received his B.S. degree from Tianjin University in 2017. His current research focuses on ultraviolet photodetectors based on low-dimensional perovskites.



**Xinya Liu** is currently pursuing her Ph.D. under the supervision of Prof. Xiaosheng Fang in the Department of Materials Science, Fudan University, China. She received her B.S. from Soochow University, China. Her current research focuses on material synthesis, device fabrication, and application in perovskite photodetectors.



**Zhifeng Shi** is currently an associate professor of School of Physics and Microelectronics, Zhengzhou University. He received his Ph.D. degree in microelectronics and solid-state electronics under the supervision of Prof. Guotong Du at Jilin University. His research interests relate to the controllable synthesis and photophysics of semiconductor optoelectronic materials and their applications in functional devices.



**Xiaosheng Fang** is a professor in the Department of Materials Science at Fudan University, China. He received his Ph.D. degree from the Institute of Solid State Physics (ISSP), Chinese Academy of Sciences in 2006. After that, he was a JSPS postdoctoral fellow at the National Institute for Materials Science, Japan, as well as a research scientist at the International Center for Young Scientists (ICYS). He was a visiting scholar at MIT and Harvard University in 2009 and 2016, respectively. His current research topic mainly focuses on inorganic semiconductors and high-performance photodetectors.



**Jr-Hau He** is a professor in the Department of Materials Science and Engineering at City University of Hong Kong. He got his B.S. and Ph.D. degrees from National Tsing Hua University in 1999 and 2005, respectively. Dr. He was a professor in Electrical Engineering at National Taiwan University and King Abdullah University of Science and Technology (2007–2019). He has dedicated his efforts to the next generation of optoelectronic devices and AI chips. He is a fellow of OSA, RSC, and SPIE, and a senior member of IEEE.